Climate and chemistry modeling of forest-atmosphere feedbacks in the Great Lakes region

by

Alexander Bryan

A dissertation submitted in partial fulfillment
of the requirements for the degree of
Doctor of Philosophy
(Atmospheric, Oceanic, and Space Sciences)
in The University of Michigan
2014

Doctoral Committee:

Associate Professor Allison L. Steiner, Chair
Professor Mary Anne Carroll
Alex B. Guenther, Pacific Northwest National Laboratory
Associate Professor Valeriy Y. Ivanov
Associate Professor Derek J. Posselt

ACKNOWLEDGEMENTS

I am indebted to my many colleagues, friends, and family for their generous time and support. The success of this dissertation would not have been possible without the following individuals.

First and foremost, I am grateful to my Ph.D. adviser, Allison Steiner, for providing me the opportunity to research a fascinating subject with a friendly and energetic research group at a quality institution. Working with Allison felt more like a partnership than an apprenticeship. Our meetings were about figuring things out together, and I always felt my suggestions were valued. This gave me confidence in my abilities as a researcher and encouraged me to be independent, yet cooperative. Not only was she open to my ideas—even if they were only excuses to get up to the biostation—she welcomed my ideas with eager excitement. Her enthusiasm is inspiring and contagious. Outside of advising Ph.D. students, Allison generously offers research opportunities to undergraduates. I would not be where I am today if it were not for the research experience I gained as an undergraduate at my alma mater, Valparaiso University, and so I am incredibly appreciative of the opportunities Allison creates for Michigan undergraduates. Another way in which Allison supports undergraduate research is through the course she created (AOSS 422: Boundary Layer Meteorology). As part of the class, students get to setup from scratch an instrument tower at the University's botanical gardens and propose original projects to analyze the data. There is no other class like in the department where students gain hands-on field research experience. I have had the pleasure of participating in the project for

three semesters: first as her student and for two semesters assisting with the setup as a grader. Allison is truly a gift to AOSS and the University of Michigan, and I am grateful to have reaped the benefits of being her student.

This dissertation would not have been possible without the generous assistance of my committee. I want to especially recognize and thank Mary Anne Carroll. She invited me to serve on the CABINEX 2009 field campaign at the University of Michigan Biological Station. I was merely looking for a summer job to fill the gap between college and grad school. Little did I know (1) how extraordinary life at the "biostation" was and (2) how beneficial it would be to see first-hand the data I would be working for the next 5 years being collected. During the project, she kindly invited to mentor some of her REU students, and to her "tree house" for socializing and libations. Where I benefited the most from Mary Anne was as her student in AOSS 479 (Atmospheric Chemistry). Mary Anne is an extraordinary advocate for students with learning disabilities (LDs) like myself, offering extra time and a separate room on exams for *anyone*—no documentation required. When my performance reflected a lack of understanding, and knowing how crucial the subject matter of the course was for my Ph.D. research, Mary Anne took me under her wing, working with me one-on-one for an additional *eight months* until I demonstrated an adequate knowledge of the course material. No professor of mine has ever invested and devoted themselves personally to my success as a pupil, and I hope to pay forward the level of commitment she blessed me with.

My work would no less be possible without the advice and support of my other committee members. Derek Posselt not only contributed a great deal scientifically to my research, in particular my Great Lakes regional climate modeling work (Chapter IV, but also invested himself in my career as a researcher through several heart-to-heart discussions on academic life and managing the work-life balance. He was also an enjoyable climbing partner, and I'm relieved I did not have to strand him at

the top of a route to guarantee my success. Alex Guenther provided crucial insights that helped inform my 1-D modeling work in Chapters II and III. In addition, Alex was an incredibly supportive mentor during my summer in Boulder, CO, as part of the Graduate Visitor Program at the National Center for Atmospheric Research (NCAR). He dedicates himself to students by ensuring we have all the resources we need. Lastly, Valeriy Ivanov contributed much of his expertise in the UMBS forest site and water fluxes toward my thesis work. His particular interests allowed him to suggest substantial improvements to all chapters in this dissertation, which he did in a very thorough way. As cognate committee members go, Valeriy was amongst the most invested I have seen.

My success as a graduate student would not have been possible without the generosity of the Steiner Lab, both in terms of hours the let me rehearse my various talks and for the social outlet they provided. Kirsti and Susan both contributed generously to Chapter III. Kirsti, in particular, and I share a special bond for our time working with the CACHE code. Stacey kindly let me pass the torch on both of my departmental service activities: GUStO and MGU. Everyone, especially, Stacey, Susan, Kirsti, and Yang, have always been there for me, particularly in these stressful final years. (Thanks for the brownies, Stacey!). Last but not least, I want to give a special shout-out to Steiner Lab alum, Ahmed Tawfik. Ahmed was a superb role model of not only a quality grad student, but a quality human being. I have always admired his kindness to everyone, especially his ability to make people feel valued. He'll laugh at your jokes even when they're not funny. In group settings, he makes a point of engaging with everybody and ensuring everyone feels welcomed and comfortable. He specifically reaches out to the quietest, shyest person in the group and says just the right thing to build that person up and make them feel confident in themselves. He did just that for me during my formative years as a grad student, and I will forever remember his kindness, sense of humor, confidence, and so many other aspects of his

great personality.

I am incredibly blessed that my life journey took me to Michigan, in particular AOSS, whose outstanding faculty, staff, and students provided me a rich experience and in many ways contributed to my success as a student. I want to recognize Frank Marsik for his friendship and advice over the years. I will never forget the day Frank saw a new face in the Steiner Lab across the hall and reached out to shake my hand. He and I shared many a-conversation on guitar playing, particularly church music, and I can't wait for his next visit out in Northampton for the next folk festival! He was gracious enough to let me borrow his bike for a summer. I will miss seeing him 1–3 days a week (depending on our motivation and willingness to get out of bed in the morning) at the gym. I also want to recognize Mark Moldwin for assisting Julie and I will getting the AOSS Graduate and Undergraduate Student Organization (GUStO) underway. (He even came up with our brilliant name!). He's been a very engaging member of the community. No faculty member has made as considerable an effort to engage with students (both graduate and undergraduate) as a whole as Mark. AOSS is very lucky to have him.

My time here at Michigan would not have been as smooth as it was without the enormous efforts of AOSS staff. Sandee Hicks has helped immensely on the forefront with GUStO efforts, but also in the background with taking care of financial and other organizational matters. She's also been a very friendly face to see and talk to on a regular basis. Sandra Pytlinski also works hard to ensure things run smoothly in so many ways. She was a pivotal contributor to MGU (now under the quality care of Eidilia Thomas), and also with academic matters, filling the large shoes of Margaret Reid, which she has done so well. Lastly, the IT staff, especially Faye, Darren, and Melissa, have been an essential part of my career here at Michigan. AOSS is blessed to have such a quality staff.

One thing I have always said and believed, and still do to this day, is that I

would not be where I am today if it weren't for the research experience I gained as an undergraduate. Therefore, I cannot thank enough Professor Gary Morris (Valparaiso University and Rice University) for seeing my potential, not only on the ballroom dance floor, but in academic research. Through him, I gained experience in experimental field work as part of a NASA campaign in Panamá, and contacts that lead to more research the following year. Specifically, I had the pleasure of working with Anne Thompson (NASA GSFC, formerly PSU, formerly Goddard (again) before that) for another NASA campaign in Yellowknife, NWT, Canada. I am thankful all the relationships I gained during these experiences, especially, David Lutz, Bonne Ford, Elizabeth Thompson, David Doughty, John Yorks, Thomas Walker, and Alaina Luzik.

My Michigan experience would not have been complete (and nearly as enjoyable) without my personal friends. A special thanks to Aron for all our runs and outings to the Renn Fair, Julie for giving her all as my esteemed GUStO co-leader, Gina for co-heading MGU with me, and, of course, for all these people (and Jim) for sharing in many lunches and good conversations. Through my wife, I was fortunate to gain several great friendships in Astronomy: Ilse, Jeb, Ashley, Colin, Dan, Sandor. I am grateful for my friends outside these departments, including my friends from Grace Ann Arbor (Matt, Elizabeth, Thomas, Andrea, Bryan), Trinity Lutheran (Lori, Sara, Brian, Marian, Natalie, Trevor, Liz and the choirs), and many others from various places and times (Chad, Aaron, Huanan, Elizabeth G., Mary, Bobby, and Debra). I want say a special thank-you to CAPS, especially my therapists Junichi, Canzi, and Kipp, for all their unending support and guidance that helped me to be a better person and student. Lastly, I want to thank my best man and dear friend, Jared Lee, for always supporting me through the years, both academically and personally.

I reserve the final paragraph of this section for my dear family: my mom, Tina; my dad, Tim; my step-dad, Ron; my brothers and sisters, Patrick, Nicholas, and

Olivia. I am grateful for the experiences I have shared with them and the love they give me daily. They know me through and through and are always there for me when I need them. Last, but certainly not least, I owe so much of not only my success but my happiness in life to my wife, Anne. She knows when I've had a good or bad day the moment I walk in the door, and knows just what to say and do in either instance. She took on the largest burden of my stress the few years, and has stuck with me through it all, still smiling in the end. Michigan has blessed me with many things—including this Ph.D.—but no greater gift came from Michigan than my wife. I thank God every day for providing me with such great fortune in this life, and I look forward to what he has in store for me next.

TABLE OF CONTENTS

LIST OF FIGURES

Figure

LIST OF TABLES

ABSTRACT

Climate and chemistry modeling of forest-atmosphere feedbacks in the Great Lakes region

by

Alexander Bryan

Chair: Allison Steiner

Vegetation impacts air quality and climate by emitting ozone precursors, known as volatile organic compounds (VOC), and water vapor. The influence of these natural emissions depends on how efficiently they escape the forest layer. This dissertation examines our understanding of this escape using multi-scale models. First, sonic anemometer data and an updated chemical mechanism are incorporated into a 1-D canopy model to improve the representation of near-canopy turbulence and VOC chemistry. The revised turbulence improves the vertical gradients in VOC, suggesting better escape, while the new chemistry scheme exacerbates VOC overestimates. The influence of canopy heterogeneity is evaluated by comparing vertically uniform and variable VOC emission potential distributions. The variable case constrains light-induced VOC emissions to the upper canopy where more light is available, leading to higher emissions. As a practical implication of this result, accounting for heterogeneity enhances changes in VOC escape following succession. Lastly, land- and lake-atmosphere feedbacks in the Great Lakes region are simulated with a 3-D regional climate model (RCM) coupled with a state-of-the-art land surface model

(LSM). A moisture budget analysis reveals that evapotranspiration accounts for up to one-quarter of the local precipitation. However, the RCM does not fully capture the spatial variability in evapotranspiration, estimated by eddy covariance measurements at three field stations, potentially due to missing complexity in its response to surface conditions in LSM parameterizations. In conclusion, the forest-atmosphere exchange of biogenic VOC and water vapor, and thus the impact of vegetation on air quality and climate, is highly sensitive to complexities in surface layer processes, which are not adequately represented in current atmospheric models at both local and regional scales. Additional eddy covariance measurements at multiple canopy depths are needed to better characterize and improve model parameterizations of canopy turbulence and evapotranspiration. Land surface descriptions require more detailed vegetation data (e.g., stand height, age, and density) to account for vertical heterogeneity in VOC emissions.

CHAPTER I

Introduction

1.1 The role of vegetation in the Earth system

Terrestrial vegetation plays a critical role in the water cycle, sustainable air quality and climate. Over land, terrestrial vegetation represents the lower boundary condition for the atmosphere, and plays a key role in cycling molecules between the surface reservoir and the atmosphere. From the climate perspective, this includes the release of water vapor into the atmosphere through transpiration and the extraction of carbon dioxide (CO_2) from the atmosphere. CO_2 and water vapor are greenhouse gases and thus CO_2 extraction reduces atmospheric warming and water vapor emission (known as transpiration) contributes to warming. Transpiration also provides moisture for cloud formation and subsequent precipitation.

From the chemical perspective, terrestrial vegetation is known to affect air quality and human health in the presence of anthropogenic pollution. Scientific research over the past three decades has identified the role of vegetation in public health through the release of ozone (O_3) and particulate matter precursors known as volatile organic compounds (VOC) (*Logan*, 1985; *Carlton et al.*, 2009). At the ground level, ozone is toxic and damaging to human and plant tissue. With respect to climate, particulate matter reflects sunlight back to space and can alter cloud formation, resulting in a cooler climate. Fine particulate matter (PM2.5) has adverse health and

respiratory effects on humans. VOC also consume oxidants that are necessary for the chemical removal of atmospheric pollution, thus limiting the ability of the atmosphere to cleanse itself (*Poisson et al.*, 2000; *Tan et al.*, 2001).

From the physical perspective, terrestrial vegetation provides a source and sink of many of these molecules. Concentrations of certain chemicals (e.g., VOC, H_2O, O_2) within leaf membranes are higher than in the surrounding atmosphere, inducing emission of such compounds. Foliage also acts as depositing surfaces for molecules with higher concentrations external to the leaves, such as CO_2 and ozone. In addition, vegetation modifies the surface energy balance by absorbing sunlight and attenuating it through the canopy. Absorbed sunlight is converted to heat energy, which raises the near-surface air temperature. The reduced sunlight in the lower canopy and soil surface results in a cooler environment in this layer. In addition, canopy elements (branches and foliage) induce aerodynamic drag (i.e., friction), which can dampen and make erratic the exchange of molecules out of the forest into the atmosphere.

1.1.1 Air quality impacts

To protect against a variety of stresses, plants release gases known as volatile organic compounds (VOCs), which impact air quality and climate indirectly as precursors of ozone (O_3) (*Logan*, 1985) and particulate matter (*Carlton et al.*, 2009; *Hallquist et al.*, 2009). While beneficial in the upper atmosphere for protecting life on Earth from solar ultraviolet radiation, ozone is toxic to humans and plants and thus undesirable in large amounts near the Earth's surface. VOC oxidation yields lower volatility products that nucleate into new particles or condense onto existing particles. These particles are known as secondary organic aerosols (SOA). Biogenic VOCs (BVOCs) emitted naturally from vegetation account for more than 80% of the global VOC budget (*Guenther et al.*, 2006) and thus have the potential to affect air quality on a global scale. However, ozone formation requires an additional

precursor of primarily anthropogenic origin (*Logan*, 1985); thus, unsustainable air quality problems are most frequent in heavily populated and industrialized urban centers (*Carslaw and Carslaw*, 2001). BVOCs can aggravate regional air quality problems, as observed in vegetated urban areas like Atlanta (*Chameides et al.*, 1988) and in forests downwind of urban areas (*Carroll et al.*, 2001; *Sillman et al.*, 2002; *Day et al.*, 2009; *Bryan et al.*, 2012). As urbanization continues, ozone problems are expected to rise unless regulations on anthropogenic emissions are implemented (*Bloomer et al.*, 2009). In addition, climate and land- use change are expected to exacerbate global ozone- and aerosol-induced air quality problems by enhancing VOC emissions (*Steiner et al.*, 2006; *Heald et al.*, 2008). Deforestation and land-use change associated with urban and agricultural expansion, however, will reduce BVOC emissions globally (*Heald et al.*, 2008). Despite these changes in BVOC levels from human activity, ozone concentrations may increase or decrease depending on anthropogenic precursors (*Steiner et al.*, 2006). Understanding the complex interplay between biogenic and anthropogenic ozone precursors is critical for implementing effective policy legislation aimed at mitigating ozone problems.

1.1.2 Climate impacts

Vegetation impacts climate in several ways, including (1) its impact on the surface energy budget and the resulting temperatures, (2) its role in the water cycle by recycling water from the surface back to the atmosphere through transpiration, (3) by fixing atmospheric CO_2 into biomass, and (4) through the release of BVOC which can form particulate matter. The dark green color of vegetation foliage gives the leaves a low albedo (i.e., reflectivity), which makes the leaves efficient absorbers of sunlight, which enhances surface heating. When plants open the pores, or stomates, on their leaves to receive CO_2, water vapor escapes, or transpires, into the atmosphere. Water vapor is another greenhouse gas with a warming feedback. However, water vapor

is also a critical component of the water cycle by supplying atmospheric moisture for cloud development and precipitation. Clouds have strong cooling feedback on climate due to their high albedo. Another cooling feedback mentioned above is the uptake of CO_2 for photosynthesis. As highlighted above, BVOCs emitted from trees are a precursor for particulate matter, specifically secondary organic aerosols (SOA, *Carlton et al.*, 2009), which also contribute to cloud formation (*Kerminen et al.*, 2005) and thus also have a cooling radiative feedback by reflecting incoming shortwave solar radiation.

1.2 Forest-atmosphere exchange

The exchange of molecules between terrestrial vegetation and the atmosphere depends on a process known as forest-atmosphere exchange. Several physical and chemical processes occurring within and above forest canopies control the exchange of molecules released from terrestrial vegetation into the atmosphere. In this dissertation, I focus on the exchange of two classes of molecules: (1) water vapor, and (2) BVOC emissions.

1.2.1 Water vapor

Vegetation emits water vapor into the atmosphere through the process of evapotranspiration, which includes the evaporation of intercepted water on the surface of leaves and the emission of water vapor molecules in the air space from leaf cavities. These two processes for water vapor flux to the atmosphere have distinct rates with unique controls. Water on the leaf surface evaporates at a rate controlled by the energy and amount of retained water, while transpiration through leaf stomata is controlled by the size of the opening in the leaf, known as the stomatal conductance, and the vapor concentration gradient across the leaf boundary. Frictional forces induced by dynamic motions along the leaf boundary layer also suppresses transpiration. The

water vapor added to the atmosphere via evapotranspiration may fuel cloud formation, which in turn may lead to precipitation, returning water back to the surface, thus describing the pivotal role of vegetation on hydroclimate. Evaporated water usually travels long distances before a cloud is formed and precipitated, but a portion of evaporated water can precipitate back into the same watershed it originated in a process known as precipitation recycling (*Schär et al.*, 1999). The recycling of moisture in the Great Lakes region is explored in Chapter IV of this dissertation.

1.2.2 BVOCs

Exchange of BVOCs across the forest-atmosphere boundary is controlled by the interactions between the vegetation and the surrounding air, but is more complex than water vapor (Section 1.2.1) because of the chemical reactivity of these compounds. Leaves in the canopy emit and take up gases directly, and the fate of these compounds in the atmosphere is affected by photochemical destruction and transport within and out of the canopy airspace. The processes of emission, deposition, chemistry, and turbulent transport are the primary controls on forest-atmosphere exchange, where the local rate of change of a trace gas concentration c at a point in the canopy is given by:

$$\frac{\partial c}{\partial t} = \frac{\partial c}{\partial t}_{\text{emission}} + \frac{\partial c}{\partial t}_{\text{deposition}} + \frac{\partial c}{\partial t}_{\text{chemistry}} + \frac{\partial c}{\partial t}_{\text{transport}} - V \cdot \nabla c. \tag{1.1}$$

where $-V \cdot \nabla c$ represents advective transport. Emission and deposition denote fluxes into and out of the atmosphere, respectively. After emission, chemistry in the atmosphere drives the transformation of BVOCs to ozone. Once BVOCs are emitted from the canopy foliage, atmospheric turbulence transports and mixes them within the atmospheric boundary layer.

1.2.2.1 BVOC emission from canopies

Plants generate terpenes—a class of BVOC of the form $C_{5x}H_{8x}$ (e.g., C_5H_8, $C_{10}H_{16}$, etc.)—for a variety of physiological purposes (*Fuentes et al.*, 2000; *Sharkey et al.*, 2008). Isoprene (C_5H_8, 2-methyl-1,3-butadiene), a hemiterpene, is generated predominantly by broadleaf vegetation such as oak and aspen (*Guenther et al.*, 1994; *Kesselmeier and Staudt*, 1999), and is thought to protect leaves from heat stress resulting from direct and prolonged exposure to intense sunlight (*Sharkey and Singsaas*, 1995), though the exact means by which isoprene offers thermoprotection is still under debate (*Sharkey and Yeh*, 2001). In addition, isoprene consumes ozone and other reactive oxygen, protecting vegetation against oxidation of foliage tissue (*Loreto and Velikova*, 2001). Needle-leaf vegetation (e.g., pine, spruce, and fir) produces monoterpenes ($C_{10}H_{16}$) to defend against insects and other herbivores (*Phillips and Croteau*, 1999) and inhibit growth of competing vegetation within the same nutrient pool (*Muller*, 1966). Larger terpenes (e.g., sesquiterpenes, $C_{15}H_{24}$) formed by plants undergo rapid chemical destruction after being emitted into the atmosphere; thus their degree of influence in gas-phase atmospheric chemistry is not well known. Isoprene and monoterpenes (collectively referred to as isoprenoids) are the focus of most studies, as they are emitted in large quantities and account for 44% and 11% of total global VOCs, respectively (*Guenther et al.*, 1995; *Steiner and Goldstein*, 2007). Regionally, however, isoprenoid emission abundances vary by plant species and geographical location due to several variables that control their formation and emission into the atmosphere.

Plants synthesize BVOCs from the carbon gained during photosynthesis at a rate proportional to light and temperature (*Fall and Wildermuth*, 1998; *Loreto et al.*, 1996). Following synthesis, BVOCs vaporize at a temperature-dependent rate and subsequently diffuse across cell membranes and through the leaf stomata, into the atmosphere (*Lerdau et al.*, 1997). Isoprene emits promptly after synthesis in the

chloroplasts of broadleaves and thus its emission follows its light- and temperature-dependent synthesis rate (*Tingey et al.*, 1979; *Monson et al.*, 1992; *Sharkey et al.*, 1996). As a result, near-canopy concentrations tend to follow the sunlight diel cycle. Monoterpenes were once believed to only emit from stored pools in needles following its temperature-dependent vaporization rate (*Guenther et al.*, 1991; *Lerdau et al.*, 1997). In recent decades, high-intensity light-dependent monoterpene emissions have been observed, particularly from tropical vegetation, and even suggest that such emissions dominate the total global monoterpene budget (*Guenther*, 2013). Such emissions have been observed in northern Michigan (*Ortega et al.*, 2007); however, the composition of these emissions indicate the plants were under stress and thus the light-dependent monoterpene emissions may not be representative of typical conditions. Other factors such as plant physiology (e.g., stomatal conductance), leaf age, recent meteorological conditions, and soil moisture are also known to affect or control the emission of isoprene and monoterpenes (*Fall and Monson*, 1992; *Guenther et al.*, 2006; *Tawfik et al.*, 2012). Herbivore attack (*Phillips and Croteau*, 1999) or extreme leaf temperature changes may also trigger short bursts in BVOC emission (*Sharkey et al.*, 2008).

1.2.2.2 Oxidation of BVOCs in the Atmosphere

Once emitted into the atmosphere, primary BVOCs are subjected to oxidation via reaction with one of three main tropospheric oxidants: the hydroxyl radical (OH), ozone (O_3), or the nitrate radical (NO_3). OH is produced in the presence of sunlight, whereas nitrate is easily destroyed by incoming solar radiation. Therefore, the OH and nitrate radicals are the main drivers of daytime and nighttime VOC oxidation, respectively, in the free atmosphere (i.e., above the forest canopy). In the canopy, however, shading by vegetation foliage and branches reduces photochemical OH production and NO_3 destruction, thus increasing the influence of nitrate as a VOC sink

even during the day (*Fuentes et al.*, 2007). Observations and models indicate that NO_2 photolysis (i.e., the destruction of NO_2 by sunlight) is also reduced within the canopy, lowering the potential for ozone formation while increasing daytime NO_3 production. As direct sunlight attenuates through the canopy, diffuse radiation from the reflection of light off leaves and aerosols becomes a major driver of in-canopy photochemistry, accounting for up to 85% of in-canopy radiation (*Knohl and Baldocchi*, 2008).

Oxidation in the atmosphere occurs on the order of seconds to days depending on several factors (*Steiner and Goldstein*, 2007). The chemical lifetime depends on the oxidation pathway, which is variable, depending on the chemical structure of the BVOC species and the availability of oxidants. Because isoprene is the most abundantly emitted BVOC and OH is the most reactive oxidant, the isoprene-OH oxidation pathway is the most influential mechanism driving BVOC chemistry and the formation of ozone precursors. Ozone has a particular affinity for compounds with double bonds and is therefore a dominant oxidant for the larger terpenes (e.g., monoterpenes and sesquiterpenes) (*Steiner and Goldstein*, 2007).

The oxidation of primary BVOC emissions (e.g., isoprene and monoterpenes) forms a suite of secondary products known as oxygenated VOCs, including formaldehyde (CH_2O), methacrolein (C_4H_6O), methyl vinyl ketone (C_4H_6O), and various additional peroxy radicals. Further oxidation of these secondary products forms the hydroperoxyl radical (HO_2), a primary atmospheric oxidant and dominant ingredient for tropospheric ozone. In addition to the formation of HO_2, oxygenated VOCs can also react with radicals to produce less volatile species that plants often take up, as discussed below.

1.2.2.3 BVOC Uptake by Plants and Deposition onto Surfaces

Many BVOCs and other airborne gases interact with the Earth's surface in a variety of ways. Gases may settle on the ground or other surfaces by gravity. Raindrops often collect and carry gases to the surface. In addition, plants take up gases through their stomata in a process known as stomatal uptake. These mechanisms are all forms of deposition, a process that removes gases from the atmosphere. Deposition rates vary by gas, as well as vegetation architecture and the ambient meteorology. Due to their low mass and low solubility, BVOCs rarely deposit via gravitational settling or capture by rain. Higher concentrations of primary BVOCs (isoprene and monoterpenes) exist within leaves than in the surrounding atmosphere, which is more conducive to emission than to stomatal uptake. Oxidized BVOCs (e.g., formaldehyde and methacrolein), on the other hand, are more highly concentrated in the atmosphere than within leaves and are thus susceptible to stomatal uptake.

Stomatal uptake occurs when atmospheric concentrations immediately adjacent to a leaf exceed those within the leaf, which allows the diffusion of molecules into the leaf structure. For example, plants take up carbon dioxide (CO_2) via stomatal uptake for photosynthesis. Ozone and sulfur dioxide (SO_2) are widely recognized as having among the highest deposition efficiencies via plant uptake (*Wesely*, 1989; *Finkelstein et al.*, 2000; *Hogg et al.*, 2007). Once taken up by the plant, ozone damages the leaf by oxidizing the tissue. Some studies postulate that plants protect themselves from ozone exposure by emitting BVOCs that react with the ozone in the air immediately surrounding the leaf (*Sharkey et al.*, 2008). Recent studies also show that products of isoprene oxidation (e.g., formaldehyde, methacrolein, and methyl vinyl ketone) that oxidize into ozone-forming peroxy radicals deposit at rates comparable to or up to 2–3 times greater than that of ozone (*Karl et al.*, 2010; *Sumner et al.*, 2001).

1.2.2.4 Turbulence-Driven Transport of BVOCs in the Atmosphere

Wind shear and free convection result in the formation of turbulent eddies in the lower atmosphere (*Stull*, 1988). These turbulent eddies mix BVOCs and their oxidation products throughout the atmospheric boundary layer, providing the dominant physical mechanism driving forest-atmosphere exchange. While molecular diffusion also transfers BVOCs from the canopy to the atmosphere, turbulence is substantially more efficient and thus diffusion is typically neglected in atmospheric models. The effect of turbulent mixing on atmospheric concentrations of gases depends on the chemical lifetime of a gas (*Molemaker and Vilà-Guerau de Arellano*, 1998; *Krol et al.*, 2000). Long-lived gases (e.g., oxygen, carbon dioxide, and methane) tend to be distributed uniformly in the planetary boundary layer (i.e., are "well-mixed") and thus turbulence has little effect on their concentrations. In contrast, short-lived gases such as oxidants (e.g., OH and nitrate) react before turbulence can transport them very far. BVOCs have a chemical lifetime that is approximately the same order as their turbulent timescale (generally, minutes to hours). Consequently, the efficiency of forest-atmosphere BVOC exchange is highly sensitive to turbulent strength, especially during the daytime (*Bryan et al.*, 2012). Therefore, while most atmospheric chemistry models may adequately capture gas exchange across the land-atmosphere boundary, models simulating BVOC exchange may require more detailed turbulence parameterizations.

Turbulent strength, typically represented in atmospheric models by the turbulent exchange coefficient (K), varies with altitude and time of day. The turbulent exchange coefficient for heat (K_H) serves as a reliable proxy for the strength of turbulence that is responsible for the exchange of atmospheric gases. Turbulence peaks in the mid-afternoon around the middle of the planetary boundary layer ($\sim$500 m above ground level). In the lower portion of the boundary layer, turbulence strength weakens with decreasing altitude as a result of frictional drag induced by the Earth's

surface. Near the forest canopy layer (∼20 m), daytime turbulence as estimated by K_H is weaker than in the mid-boundary layer by approximately two orders of magnitude. This reduction in turbulence strength near the surface layer partially accounts for the similarity in timescales between turbulence-induced exchange and chemical degradation of BVOCs within forest canopies noted above.

The nature of turbulence within forest canopies is complex due to the presence of vegetation. Foliage, branches, and other sources of roughness induce aerodynamic drag, perturbing and weakening dynamic motions and movement of gases in the canopy airspace (*Baldocchi*, 1988). The strength of frictional drag varies widely with canopy structure, in particular with respect to foliar density as well as the heterogeneous nature of the canopy. Dense canopies exhibit particularly slow fluxes of BVOCs across the forest-atmosphere boundary in large part due to the physical obstruction of canopy elements.

As a consequence of the relatively weak background turbulence within and below forest canopies, in-canopy motions are particularly sensitive to other dynamical perturbations. Intense bursts of turbulent activity known as coherent structures (*Collineau and Brunet*, 1993a; *Finnigan*, 2000; *Steiner et al.*, 2011) occur in two common forms: (1) rapid streams of downward motion that pass through the canopy layer known as "sweeps" and (2) subsequent upward motions known as "ejections" (*Raupach et al.*, 1996). These erratic motions may be critical for the efficient exchange of BVOCs out of the canopy layer given the weak nature of in-canopy turbulence. Unfortunately, due to the brief (lasting on average 5–7 seconds), intermittent (occurring at uneven intervals ranging from 15–75 seconds), and unpredictable nature of these events (*Collineau and Brunet*, 1993b), these events are typically filtered from observational datasets via time averaging as part of data analysis and neglected in atmospheric models. Consequently, correlating BVOC fluxes with coherent structure events is still an area of active research, and the effects of these phenomena on

forest-atmosphere BVOC exchange are not yet well understood.

1.2.3 Current Understanding of Forest-Atmosphere Exchange

Forest-atmosphere water vapor exchange in climate models has a long history of development (*Bonan*, 2008). The earliest models (late 1960s) neglected vegetation and evaporation (expressed in terms of the surface energy balance as latent heat flux) was entirely a function of soil moisture. Vegetation was explicitly introduced into models in the mid-1980s, which treated soil evaporation and canopy evaporation and transpiration (collectively referred to as evapotranspiration) in terms of both the surface energy balance and the hydrological cycle. By this point, controls on evapotranspiration went beyond simply soil moisture availability to include dependencies on vegetation physiology, which experienced improvements in the following decade with advances in our knowledge of the relationships between evaporative fluxes and photosynthesis, in particular CO_2 uptake (*Sellers et al.*, 1996).

Considerable research has focused on forest-atmosphere BVOC exchange through a number of observational field campaigns at flux towers in the United States (e.g., CABINEX, *Bryan et al.*, 2012; BEARPEX, *Wolfe and Thornton*, 2011; CELTIC, *Stroud et al.*, 2005; and BEACHON, *DiGangi et al.*, 2011). The diverse array of vegetation types covered by these studies allows for the examination of both isoprene- and monoterpene-dominated sites. Often coupled with modeling studies, these campaigns may reveal discrepancies between simulated and observed conditions that illuminate gaps in our knowledge of canopy processes.

Discrepancies between model simulations and field observations of oxidants and BVOC oxidation products highlight the need to better understand BVOC oxidation in forest canopies. Current models have difficulty simulating the OH radical in remote forest environments where vegetation plays an important role in OH regulation (*Tan et al.*, 2001; *Di Carlo et al.*, 2004; *Pugh et al.*, 2010). For example, if BVOC

emissions from the forest canopy are very high, then they can deplete OH concentrations in the troposphere. In fact, most models predict this drawdown of OH that cannot be confirmed with observations. Models generally underestimate OH concentrations (*Tan et al.*, 2001; *Lelieveld et al.*, 2008), suggesting either over-depletion in atmospheric chemistry models or a missing in-canopy source. *Lelieveld et al.* (2008) propose an OH recycling pathway that avoids OH depletion, which several laboratory experiments confirmed (*Hasson et al.*, 2004; *Jenkin et al.*, 2007; *Dillon and Crowley*, 2008), suggesting a viable source of the missing VOC oxidation in forest environments. Models also do not capture long-range horizontal transport from isoprene-poor regions (*Sillman et al.*, 2002) or downward mixing of VOC-clean air from the free atmosphere (*Hurst et al.*, 2001) that may reduce OH loss. Additional OH sources from terpene dissociation via ozone reaction (*Faloona et al.*, 2001) may also account for the underestimation of OH. While underestimated concentrations suggest a missing OH source in models, models also underestimate OH reactivity within the canopy (*Di Carlo et al.*, 2004), which suggests a missing modeled sink of OH as well. *Di Carlo et al.* (2004) hypothesize that forest emissions contain VOCs that have yet to be identified and accounted for in atmospheric chemistry models; however, more recent studies suggest that the OH reactivity can be accounted for by including the oxidation of secondary VOCs discussed above (*Kim et al.*, 2011).

While many past studies have attributed these differences to chemistry, it is also possible that atmospheric models do not accurately capture the vertical mixing of BVOCs. Observational and modeling studies alike point to a need for an improved turbulence characterization and representation in model parameterizations (*Hurst et al.*, 2001; *Horiguchi et al.*, 2010; *Bryan et al.*, 2012). In particular, models neglect the erratic canopy-scale eddies frequently observed in tall plant stands (*Finnigan*, 2000), yet these phenomena may contribute 50 percent or more to the total heat fluxes out of the canopy (*Steiner et al.*, 2011).

Vertically heterogeneous canopies, such as the successional forest of the University of Michigan Biological Station located at the northern tip of Michigan's lower peninsula, exhibit a diverse array of biogenic emissions along with vertically varying emissions as a function of canopy light extinction, as examined in Chapter III. Though many studies report extensive inventories of BVOC emissions for a wide range of tree species (*Guenther et al.*, 1994; *Kesselmeier and Staudt*, 1999; *Steiner and Goldstein*, 2007; *Warneke et al.*, 2010), such studies report single values for each BVOC and tree species for the forest site of interest despite large variability in the reported BVOC emissions, even for the same tree species. Therefore, many modeling studies utilize the generalized approximations reported by *Guenther et al.* (1994) for the sake of consistency.

1.3 Multi-scale modeling of forest-atmosphere exchange

The previous section highlights the unique chemical and dynamic environment that exists within forest canopies. All of these chemical and physical processes occur over a range of spatial scales, from the leaf level (cm) to the canopy level (m) to the atmospheric boundary layer (km). In order to address these scale issues, models introduce parameterizations. Most three-dimensional (3-D) models have regional-scale domains, with horizontal resolutions ranging on the order of 1 to 100 km. In such models, the small-scale in-canopy processes are highly parameterized and thus such models do not capture the complexities in structure, chemistry, and dynamics occurring within forests.

One-dimensional (1-D) column models with highly resolved layers in the canopy have been used to capture and analyze the complex canopy environment (*Forkel et al.*, 2006; *Boy et al.*, 2011; *Wolfe and Thornton*, 2011). Such models are typically split into three distinct layers with multiple grid points within each layer (from top to bottom): (1) the planetary boundary layer, (2) the crown space, and (3) the trunk space. Some

models include one or more soil layers for storing surface heat and moisture and simulating the interactions with the overlying atmosphere. For atmospheric chemistry applications, the canopy layer includes parameterizations for simulating leaf energy balance, BVOC emissions, deposition, in-canopy turbulence, among other processes. The multiple grid points allow users to resolve the architecture of the forest canopy and its effect on light attenuation on the surface energy balance, which affects surface heating and BVOC emissions. In-canopy dynamics are treated differently than the overlying planetary boundary layer to account for added drag of canopy foliage. 1-D models typically have distinct treatments of in-canopy and above-canopy (i.e., planetary boundary layer) processes. Chapters II and III apply a 1-D model (Canopy Atmospheric CHemistry Emission model (CACHE, *Forkel et al.*, 2006)), to examine forest-atmosphere exchange at a research station in northern Michigan.

While 1-D models are useful to examine processes within the forest, an understanding of the role of vegetation on the climate system requires a broader scale achieved by regional scale climate models. To improve simulations of surface-atmosphere interactions, climate models are often coupled with land surface models to capture the dependence of these interactions on surface processes (*Bonan*, 1995). A variety of land surface models have been developed of varying complexity, resolution, and representation of biophysics (*Dickinson et al.*, 1986; *Oleson et al.*, 2004). The first of these models was the Biosphere-atmosphere Transfer Scheme (BATS, *Dickinson et al.*, 1986, 1993), representing the basic biophysical and hydrological processes within vegetated ecosystems such as the surface energy balance, and canopy- and soil-atmosphere moisture fluxes. Current land surface models, such as the NCAR Community Land Model (CLM, *Oleson et al.*, 2004, 2008), now include components representing ocean and lake processes, carbon cycling, and organic aerosol formation. In addition, recent models now have more complex land cover descriptions than their predecessors, including multiple soil textures and a wider array of vegetation classes

that change dynamically according to their phenological cycles (*Oleson et al.*, 2004). In Chapter IV, I examine land- and lake-atmosphere feedbacks in the Great Lakes region using the 3-D Abdus Salam International Centre for Theoretical Physics (ICTP) Regional Climate Model version 4.3.4 (RegCM, *Giorgi et al.*, 2012) coupled with the National Center for Atmospheric Research (NCAR) Community Land Model version 3.5 (CLM, *Oleson et al.*, 2004).

1.4 Thesis overview

This dissertation examines the treatment of surface-atmosphere exchange using two different scales of models: (1) a 1-D model to examine the role of the canopy model at a local scale, and (2) a 3-D regional climate model to address a broader scale. The primary goal is to determine the controls on the forest-atmosphere exchange of BVOC and water vapor, and examine how 1-D and 3-D models represent and capture those controls. To accomplish this, we use a suite of measurement datasets to establish relationships between trace gas exchange and observable surface conditions (e.g., surface temperature, surface energy fluxes), and evaluate the ability of local and regional models to capture these relationships. This assessment aims to identify the greatest model development needs to improve the simulation of surface impacts on atmospheric chemistry and climate. Chapters II and III utilize the 1-D canopy model, CACHE, and compare output against multiple measurement parameters at multiple heights during the CABINEX campaign. Chapter II examines the relative roles of in-canopy turbulence or chemistry on the exchange of BVOC in a forest canopy. Chapter III uses a novel approach to simulate vertically heterogeneous BVOC emissions and assesses the importance of accounting for heterogeneity for forest-atmosphere BVOC exchange. Using the 3-D RegCM-CLM, Chapter IV assesses the importance and uncertainties associated with surface moisture fluxes. Finally, Chapter V summarizes the dissertation work, provides broader implications for air quality and climate

practitioners, and offers suggestions for future investigations and model development to improve our understanding and the simulation of forest-atmosphere exchange.

CHAPTER II

In-canopy gas-phase chemistry during CABINEX 2009: sensitivity of a 1-D canopy model to vertical mixing and isoprene chemistry

2.1 Abstract

Vegetation emits large quantities of biogenic volatile organic compounds (BVOC). At remote sites, these compounds are the dominant precursors to ozone and secondary organic aerosol (SOA) production, yet current field studies show that atmospheric models have difficulty in capturing the observed HO_x cycle and concentrations of BVOC oxidation products. In this chapter, we simulate BVOC chemistry within a forest canopy using a one-dimensional canopy-chemistry model (Canopy Atmospheric CHemistry Emission model; CACHE) for a mixed deciduous forest in northern Michigan during the CABINEX 2009 campaign. We find that the base-case model, using fully-parameterized mixing and the simplified biogenic chemistry of the Regional Atmospheric Chemistry Model (RACM), underestimates daytime in-canopy vertical mixing by 50–70 % and by an order of magnitude at night, leading to discrepancies in the diurnal evolution of HO_x, BVOC, and BVOC oxidation products. Implementing observed micrometeorological data from above and within the canopy substantially improves the diurnal cycle of modeled BVOC, particularly at the end of the day, and

also improves the observation-model agreement for some BVOC oxidation products and OH reactivity. We compare the RACM mechanism to a version that includes the Mainz isoprene mechanism (RACM-MIM) to test the model sensitivity to enhanced isoprene degradation. RACM-MIM simulates higher concentrations of both primary BVOC (isoprene and monoterpenes) and oxidation products (HCHO, MACR+MVK) compared with RACM simulations. Additionally, the revised mechanism alters the OH concentrations and increases HO_2. These changes generally improve agreement with HO_x observations, yet overestimate BVOC oxidation products, indicating that this isoprene mechanism does not improve the representation of local chemistry at the site. Overall, the revised mechanism yields smaller changes in BVOC and BVOC oxidation product concentrations and gradients than improving the parameterization of vertical mixing with observations, suggesting that uncertainties in vertical mixing parameterizations are an important component in understanding observed BVOC chemistry.

2.2 Introduction

There is increasing evidence of the important role of forest canopies and biogenic volatile organic compound (VOC) emissions on tropospheric composition and atmospheric chemistry (*Goldstein and Galbally*, 2007; *Lelieveld et al.*, 2008). VOC oxidation, in the presence of reactive nitrogen oxides ($NO_x = NO + NO_2$) and sunlight, is critical for ozone formation (*Logan*, 1985) and condensation of their oxidation products can yield secondary organic aerosols (SOA) (*Claeys et al.*, 2004; *Carlton et al.*, 2009; *Hallquist et al.*, 2009). Additionally, VOC can control the oxidation capacity of the troposphere through the regulation of hydrogen radicals ($HO_x = OH + HO_2$) (*Poisson et al.*, 2000; *Tan et al.*, 2001). Forest canopies are an important VOC source both globally and regionally, contributing to nearly half the global VOC budget (*Guenther et al.*, 1995). To affect the troposphere, biogenic VOC (BVOC) emissions

and their oxidation products must be mixed effectively out of the forest canopy. This forest-atmosphere exchange is highly sensitive to turbulent mixing and chemistry because BVOC oxidation and transport occur on similar timescales (*Molemaker and Vilà-Guerau de Arellano*, 1998; *Krol et al.*, 2000; *Pugh et al.*, 2010).

To investigate the role of BVOC on tropospheric chemistry, several recent field campaigns have involved chemical measurements at multiple heights throughout the forest canopy (e.g., *Carroll et al.*, 2001; *Hewitt et al.*, 2010; *Martin et al.*, 2010). Results from these field campaigns highlight gaps in our understanding of BVOC oxidation. For example, the hydroxyl radical (OH) is underestimated in most forest ecosystem types (*Carslaw and Carslaw*, 2001; *Tan et al.*, 2001; *Butler et al.*, 2008; *Karl et al.*, 2009). Modeling studies of remote forest sites that add a HO_x recycling mechanism through BVOC oxidation reactions (*Lelieveld et al.*, 2008; *Hofzumahaus et al.*, 2009) or OH regeneration from epoxides (*Paulot et al.*, 2009) display some improvement in measured-modeled agreement in some locations, yet these do not show consistent improvement in all studies (*Karl et al.*, 2009; *Barkley et al.*, 2011). Additionally, BVOC oxidation products are poorly simulated in a number of forest regimes. *Pugh et al.* (2010) show that first-generation oxidation products of isoprene (C_5H_8, 2-methyl-1,3-butadiene)—the dominant BVOC emission in many broadleaf ecosystems—are overestimated by box-model simulations of a Malaysian tropical rainforest. *Karl et al.* (2009) compare several mechanisms with enhanced isoprene oxidation and find that some isoprene oxidation products such as hydroxyacetone are underpredicted compared to observations. While revised chemical mechanisms can explicitly account for more detailed isoprene chemistry (*Pöschl et al.*, 2000; *Paulot et al.*, 2009; *Peeters et al.*, 2009; *Stavrakou et al.*, 2010), difficulties remain in simulating isoprene degradation and oxidation products under low-NO_x conditions (*Karl et al.*, 2009).

In addition to uncertainties in the pathways of BVOC oxidation, vertical trans-

port within and above the canopy sub-layer is an additional source of uncertainty in forest-atmosphere exchange (*Finnigan*, 2000; *Hurst et al.*, 2001). Here, we define the canopy sub-layer as the thin atmospheric layer nearest the surface containing forest roughness elements. Turbulence occurs over a range of scales in the planetary boundary layer (PBL) from the mesoscale to the sub-grid scale, and thus, must be either represented with higher-order turbulence schemes or parameterizations. Among the most common parameterizations is the first-order flux-gradient relationship, known as K-theory, in which turbulent exchange is a function of the eddy diffusivity parameter, K (*Blackadar*, 1979). Because mixing strength in the mid-PBL peaks at two orders of magnitude higher than in the canopy roughness layer (*Gao et al.*, 1993), turbulent transport tends to be much smaller within plant canopies than above the roughness elements. In fact, K-theory has been found to break down completely within forest canopies due to the existence of intermittent coherent structures that encompass the entire depth of the canopy (*Raupach et al.*, 1996), yet the parameterization continues to be used for its computational efficiency in many models (*Forkel et al.*, 2006). Though high-resolution canopy models may have the vertical resolution to capture fine-scale turbulence within the canopy, many models do not have the detailed description of higher-order turbulence to simulate the effects of coherent structures and other canopy-scale turbulence. Therefore, most models may have large uncertainties in the role of vertical mixing on BVOC gradients and forest-atmosphere exchange (e.g., *Ganzeveld et al.*, 2006). Near-field effects, often represented by a scaling factor (*Makar et al.*, 1999; *Stroud et al.*, 2005; *Wolfe and Thornton*, 2011), have been shown to improve modeled in-canopy and above-canopy turbulence (*Raupach*, 1989). Large-eddy simulation models (e.g., *Heus et al.*, 2010; *Patton et al.*, 2001) can capture these dynamical changes, though development with sufficient detail in chemical mechanisms is still underway (e.g., *Kim et al.*, 2012). The use of a 1-D model in this study represents a computationally efficient preference towards a detailed chemical

mechanism over that of a detailed turbulence parameterization.

Despite the uncertainties in vertical mixing, one-dimensional (1-D) models are still useful tools for studying the vertical transport in the context of atmospheric composition because they focus on the implications of in-canopy chemistry on vertical concentrations and gradients (e.g., *Wolfe et al.*, 2011; *Boy et al.*, 2011). *Wolfe et al.* (2011) examine daytime biogenic chemistry at a ponderosa pine plantation, concluding that chemistry may outweigh the effect of turbulent mixing on forest-atmosphere exchange, even for compounds with long chemical lifetimes relative to their transport timescales. *Boy et al.* (2011) apply a more detailed turbulence scheme to understand BVOC oxidation and tracer transport and their effect on particle formation in a Scots Pine forest in Finland and find that this improved mixing parameterization can reproduce observed vertical profiles of BVOC.

Here, we focus on chemistry and turbulence within and above a deciduous hardwood forest in Northern Michigan. A number of field campaigns as part of the Program for Research on Oxidants: PHotochemistry, Emissions, and Transport (PROPHET, *Carroll et al.*, 2001) have been conducted since 1997 at the University of Michigan Biological Station (UMBS). Results from the summer 1998 PROPHET intensive show that models underestimate OH (*Faloona et al.*, 2001; *Sillman et al.*, 2002), while measured HO_2 concentrations compare well with model results (*Tan et al.*, 2001). Measurements of OH reactivity suggest an unknown BVOC source, which may contribute to these OH discrepancies (*Di Carlo et al.*, 2004). In 2009, the Community Atmosphere-Biosphere INteractions Experiment (CABINEX) was conducted to provide new insights into the role of BVOC chemistry and its relationship to HO_x chemistry observed at the PROPHET site. Branch enclosure measurements from CABINEX 2009 show that identified primary emissions reasonably reflect current emission estimates (*Ortega et al.*, 2007), suggesting that the missing ambient OH reactivity could be explained by secondary BVOC oxidation products (*Kim et al.*,

2011).

In this manuscript, we compare measurements from the CABINEX 2009 campaign with a 1-D Eulerian Canopy Atmospheric CHemistry Emission model (CACHE, *Forkel et al.*, 2006) to investigate the role of in-canopy chemistry and turbulence on HO_x and BVOC concentrations and vertical gradients. To examine the relative sensitivities of the model to mixing and chemistry, we compare a base-case model scenario with the original turbulence and chemistry description within CACHE against a revised mixing scheme and isoprene-focused chemical mechanism. We explore the relative impacts of HO_x pathways in an atmospheric chemical mechanism versus the effects of vertical mixing on ambient concentrations to isolate and highlight the key processes of biosphere-atmosphere interactions at this deciduous forest ecosystem.

2.3 Methods

2.3.1 CABINEX 2009 campaign

CABINEX 2009 was conducted at the PROPHET site at UMBS near Pellston, MI (45° 33′31.66″ N, 84° 43′52.40″ W) at the transition between mixed hardwood to boreal forest (*Schmid et al.*, 2003). Depending on the wind direction, the site can be controlled by local emissions and chemistry or regional transport from urban areas (Milwaukee, WI ($\sim$ 378 km SW); Detroit, MI ($\sim$ 385 km SSE); and Chicago, IL ($\sim$ 475 km SW), as shown in Fig. 2.1). The local vegetation is diverse (*Pressley et al.*, 2005), containing varieties of aspen, oak, beech, birch, maple, and pine with an average canopy height (h) of approximately 22.5 m. Climate conditions at the PROPHET site are generally cold but with warm summers (FLUXNET database, *Baldocchi et al.*, 2001). The average daily maximum temperatures for Pellston, MI, in July and August are 26 °C and 25 °C with average precipitation of 63.2 mm and 81.8 mm, respectively. The summer of 2009 was unseasonably cool and cloudy with

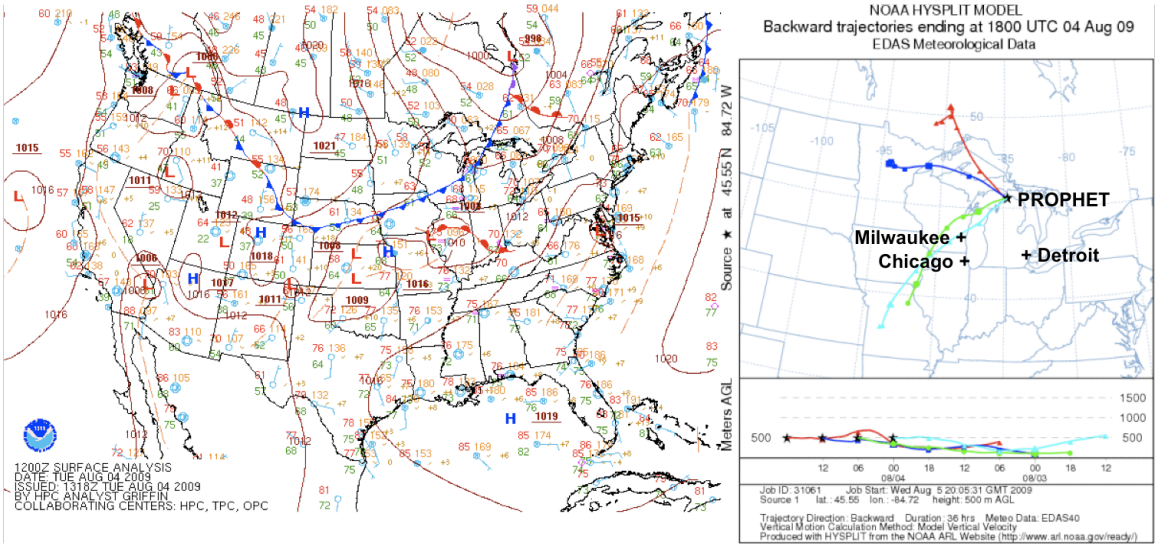

Figure 2.1: Surface reanalysis **(left)** for 07 EST 4 August 2009 and 36-hour backward trajectories **(right)** ending at 19 EST on 3 August 2009 (cyan), and 01 EST (green), 07 EST (blue), and 13 EST (red) on 4 August 2009. Surface reanalysis data is provided by the National Center for Environmental Prediction (NCEP), a division of the NOAA Climate Diagnostics Center. Back-trajectory data is provided by the NOAA (R. R. Draxler and G. D. Rolph, HYSPLIT (Hybrid Single-Particle Lagrangian Integrated Trajectory) model, accessed via NOAA ARL READY Website, Air Resour. Lab., NOAA, Silver Spring, Md., 2003, available at http://www.arl.noaa.gov/ready/hysplit4.html)

an average high temperature of 22 °C and with rain or fog occurring on 62 % of the days within the 1 July–8 August 2009 observational period, which may reduce BVOC emissions and photochemical activity.

O_3, NO_2, NO, isoprene, monoterpenes, formaldehyde (HCHO), methacrolein and methyl vinyl ketone (MACR+MVK), OH, HO_2, and glyoxal (GLY) were measured at multiple heights within and above the canopy. Due to limited instrumentation during the campaign, simultaneous measurements at multiple heights could not be obtained for all compounds. Therefore, data availability at a given height widely varies over the campaign. Primary BVOC species and BVOC oxidation products were measured, alternating at 10-min intervals between 6 m, 20.4 m, and 34 m, using a proton transfer reaction mass spectrometer (PTR-MS) with dehumidified sampling to allow more sensitive measurement of HCHO (*de Gouw and Warneke*, 2007; *Jobson and McCoskey*, 2010). Simultaneous measurements at all three inlet heights could not be obtained to do the availability of only one instrument. NO and NO_2 were measured, alternating between the same three heights, using a 2-channel chemiluminescence instrument with a blue light photolytic converter for NO_2 (Air Quality Design). HO_x species were measured only at 32 m during the two-day simulation presented here, with OH measured using laser-induced fluorescence with the Fluorescence Assay by Gas Expansion (FAGE) technique and HO_2 measured by chemical conversion to OH with added NO (*Stevens et al.*, 1994; *Dusanter et al.*, 2009). Total OH reactivity was measured at 30.9 m using a turbulent flow tube technique similar to that described in *Kovacs and Brune* (2001). Glyoxal (GLY) was measured at 35.4 m using laser-induced phosphorescence (*Huisman et al.*, 2011). Wind speed and direction were measured via propeller anemometer at 36.4 m. Additionally, two sonic anemometers measuring the three-component wind field (u, v, and w) and temperature were mounted at 20.6 m and 34 m (*Steiner et al.*, 2011). Temperature was also measured at 6 m, 20.4 m, and 31.2 m using R. M. Young relative humidity and tem-

perature probes. Photosynthetically active radiation (PAR) was measured at 32.6 m using a BF-3 Sunshine Sensor.

2.3.2 Model description and simulations

CACHE is a 1-D multilayer model that simulates the vertical distribution of concentrations and vertical fluxes of heat, moisture, and gas-phase chemical species over time using the prognostic equations for potential temperature (θ) and volume mixing ratio for compound i (c_i):

$$\frac{\partial \theta}{\partial t} = \frac{\partial}{\partial z}\left(K_{\mathrm{H}}\frac{\partial \theta}{\partial z}\right) + S_{\mathrm{H}} \tag{2.1}$$

$$\frac{\partial c_i}{\partial t} = \frac{\partial}{\partial z}\left(K_{\mathrm{H}}\frac{\partial c_i}{\partial z}\right) + S_{\mathrm{c}} + C \tag{2.2}$$

Equations (2.1) and (2.2) are solved for each model layer, where K_{H} denotes the turbulent exchange coefficient for heat, S_{H} and S_c denote sources and sinks for heat and mass, respectively, and C denotes chemical transformation. Turbulent exchange, chemistry, emissions, deposition, and advection are described in subsequent sections.

For our simulations of the PROPHET site, we use a model domain consisting of 40 vertical layers spanning 4.4 km in the vertical (z) direction with eight layers in the 6-m trunk space and ten layers in the 16.5-m crown space. To accommodate our focus on near-canopy processes and exchange, the grid resolution decreases exponentially with height with a spacing of 0.81 m at ground level and 1061.1 m at the top. Simulations are run for 48 h at a time step of 60 s. Initial conditions are provided to the model for vertical profiles of chemical concentrations based on observed near-canopy concentrations at the start of the simulation; the initial vertical temperature profile is interpolated using radiosonde data from Gaylord, MI ($\sim$59.5 km S). Model input includes (Fig. 2.2): (1) observed PAR to drive the prognostic temperature profile and photochemistry and account for cloud cover, and (2) observed wind speed and

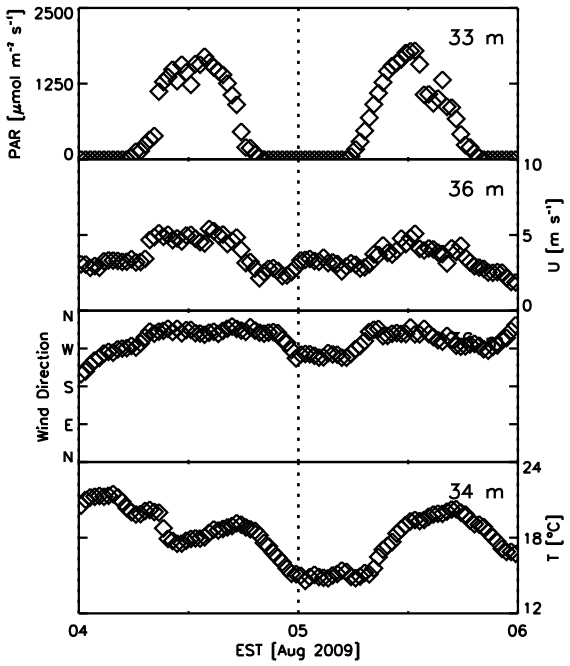

Figure 2.2: Observed photosynthetically-active radiation (PAR), wind speed (U), wind direction, and temperature (T) measured at the PROPHET tower.

direction at 36.4 m to drive the vertical wind profile and NO_x and VOC advection. Additional input required for the revised turbulence scheme (see Sect. 2.3.2.1) include u_* and σ_w at 20.6 and 34 m. In addition, we prescribe a total leaf area index (LAI) of $3.8\,m^2\,m^{-2}$ (as observed at PROPHET, *Ortega et al.*, 2007) and typical values for leaf reflectance and transmittance observed in deciduous broadleaf ecosystems (see Table 2.1, *Asner*, 1998). Model output is interpolated at the instrument heights and data collection times for precise comparison with measurements.

Table 2.1: Leaf and soil reflectance and transmittance by waveband (visible/near infrared/thermal) used in CACHE. Absorptivities can be calculated as the remaining fraction that is neither reflected nor absorbed. Values are derived from *Asner* (1998).

	Soil	Leaf
Reflectance	0.15/0.20/0.10	0.20/0.45/0.10
Transmittance	0.00/0.00/0.00	0.10/0.30/0.10

2.3.2.1 Turbulent exchange

Vertical transport is parameterized in CACHE using a first-order flux-gradient relationship, or K-theory, in which heat and mass are transported by eddy diffusion at a rate proportional to the turbulent exchange coefficient for heat, K_{H}. Vertical fluxes of heat and mass are computed at each model time step as follows:

$$\overline{w'\theta'} = -K_{\mathrm{H}} \frac{\partial \bar{\theta}}{\partial z} \tag{2.3}$$

$$\overline{w'c_i'} = -K_{\mathrm{H}} \frac{\partial \bar{c_i}}{\partial z}. \tag{2.4}$$

Modeled K_{H} (hereinafter denoted $K_{\mathrm{H,mod}}$) is derived empirically according to *Forkel et al.* (1990) given a length scale l, the vertical wind shear $|\partial v/\partial z|$, and a stability parameter f:

$$K_{\mathrm{H,mod}} = l^2 \left| \frac{\partial v}{\partial z} \right| \cdot f. \tag{2.5}$$

l varies within and above the canopy according to the following parameterization:

$$l = \frac{\kappa(z-d)}{1 + (\kappa(z-d)/\lambda)} \tag{2.6}$$

where κ is the von Kármán constant (0.4), d is the zero-plane displacement height (0.85 h for $z \geq h$ and zero for $z < h$), and λ is the maximum mixing length (given by *Forkel et al.* (1990, Eq. (10)) for $z \geq h$ and set constant at 2 m for $z < h$). The vertical

wind profile for computing $|\partial v/\partial z|$ derives from the common logarithmic expression for the PBL (*Stull*, 1988); within the canopy, winds dissipate as a function of u_* and canopy structure according to a modified logarithmic-wind equation following *Baldocchi* (1988, Eq. 6). f is a function of the Richardson number Ri:

$$f(\mathrm{Ri}) = \begin{cases} 1.35\sqrt{1-11\mathrm{Ri}}\frac{1-5.5\mathrm{Ri}}{1-3\mathrm{Ri}} & : \mathrm{Ri} < 0 \\ 1.35[(1+6\mathrm{Ri})\sqrt{1+6\mathrm{Ri}}]^{-1} & : \mathrm{Ri} \geq 0 \end{cases} . \tag{2.7}$$

In the original model configuration—hereafter referred to as the "BASE" model scenario – the vertical turbulence profile is driven solely by Eqs. (2.5–2.7).

To evaluate the sensitivity of BVOC gradients to in-canopy vertical mixing, we apply an alternate K-theory parameterization in a modeling scheme hereafter referred to as the "MIX" simulation. We first define "observed" K_H (hereafter denoted by $K_{\mathrm{H,obs}}$) following *Makar et al.* (1999):

$$K_{\mathrm{H,obs}} = \sigma_w^2 T_\mathrm{L} \tag{2.8}$$

where T_L is the Lagrangian timescale ($T_\mathrm{L} = 0.3h/u_*$), u_* is the friction velocity, and σ_w is the vertical velocity standard deviation. u_* and σ_w are computed using half-hour Reynolds averages of raw (10 Hz) sonic anemometer measurements of u, v, and w above the canopy (34 m; 1.5 h) and in the top of the canopy (20.6 m; 0.9 h):

$$u_* = \left(\overline{u'w'}^2 + \overline{v'w'}^2\right)^{1/4} \tag{2.9}$$

$$\sigma_w = \sqrt{\frac{1}{n-1}\sum_{i=1}^{n}(w_i - \bar{w})^2} \tag{2.10}$$

In the MIX simulations, we adjust the modeled turbulence profile (i.e. the BASE case) to match the near-surface observations estimated in Eq. (2.8) as follows. At each

time step, we first compute a full vertical profile of $K_{\mathrm{H,mod}}$ using Eq. (2.5). Then, we linearly interpolate between $K_{\mathrm{H,mod}}$ at the canopy base (6 m) and $K_{\mathrm{H,obs}}$ at the first measurement level (20.6 m). At the model grid points between the two measurement heights (20.6–34 m), we linearly interpolate u_* and σ_w and compute $K_{\mathrm{H,obs}}$ using Eq. (2.8). Above 34 m, modeled values are adjusted to remove any discontinuity between the measured and modeled values. Near-canopy K_{H} ($z \leq 1.64\ h$) is scaled by an R factor to account for near-field effects of the canopy, where R is:

$$R = \frac{\left[1 - \exp\left(-\tau/T_{\mathrm{L}}\right)\right]\left(\tau - T_{\mathrm{L}}\right)^{3/2}}{\left[\tau - T_{\mathrm{L}} + T_{\mathrm{L}}\exp\left(-\tau/T_{\mathrm{L}}\right)\right]^{3/2}} \tag{2.11}$$

and the transport timescale τ is derived using a τ/T_{L} ratio of 4 (*Stroud et al.*, 2005; *Wolfe and Thornton*, 2011). We evaluate the revised mixing scheme in Sect. 2.4.1.

2.3.2.2 Chemistry

Gas-phase chemical transformation in the original CACHE model implements the Regional Atmospheric Chemistry Mechanism (RACM, *Stockwell et al.*, 1997), which includes a suite of 77 chemical species and 237 reactions. The mechanism includes explicit treatment of three BVOC categories: isoprene (denoted by the RACM surrogate, ISO), monoterpenes with one double bond (i.e. α-pinene; denoted API), and monoterpenes with two double bonds (i.e. *d*-limonene; denoted LIM). The remaining VOC are lumped into four alkane categories, four alkene categories, and three aromatic categories based on reactivity with OH. In the RACM mechanism, MACR+MVK are contained in the surrogate for all unsaturated C4 carbonyls (denoted MACR in *Stockwell et al.* (1997)), which derive from both anthropogenic and biogenic diene oxidation; however, we note that measurements from the campaign only account for MACR+MVK alone.

In this study, we perform a sensitivity test (hereafter referred to as the "MIM"

simulation) comparing RACM against the Mainz isoprene mechanism (MIM) adaptation of RACM (RACM-MIM, *Geiger et al.*, 2003). RACM-MIM treats an additional seven species explicitly that are split from surrogate species in RACM. By using this greater speciation, RACM-MIM includes an additional twelve reactions. Ultimately, this mechanism provides more specific pathways of isoprene oxidation, the production of second-generation isoprene oxidation products, and further detail on the MACR chemistry under low-NO_x conditions.

2.3.2.3 Emissions

BVOC emissions are controlled by site-specific emission rates that depend on ecosystem-specific emission factors, temperature, and PAR (*Steinbrecher et al.*, 1999). Isoprene emission fluxes were not routinely measured during the campaign; therefore, we use the mean isoprene surface emission flux observed at PROPHET during 2003 and 2005 (*Ortega et al.*, 2007). Emission fluxes are held constant throughout the simulation. Bigtooth aspen (*Populus grandidentata*) and northern red oak (*Quercus rubra*) account for 99 % of the isoprene budget, emitting at mean basal emission rates of 46.3 and 53.5 $\mu g\,C\,g^{-1}\,h^{-1}$ at standard conditions (PAR = 1000 $\mu mol\,m^{-2}\,s^{-1}$; temperature = 30 °C). Since 2009 was colder than average summers, we subtract one standard deviation from the mean isoprene emission fluxes, corresponding to 24.8 $\mu g\,C\,g^{-1}\,h^{-1}$ for aspen and 23.8 $\mu g\,C\,g^{-1}\,h^{-1}$ for oak, which yields the best fit for BVOCs. The net emission of isoprene per model level is determined by scaling the given emission factors by PAR and temperature, according to the parameterization described in *Forkel et al.* (2006) following *Guenther et al.* (1995), and a prescribed vertical LAI distribution. Monoterpene emission rates derive from tree branch enclosure measurements in 2003, 2005 and 2009 (*Ortega et al.*, 2007; *Ortega and Helmig*, 2008). Normalized (20 °C) foliage emission rates for the sum of monoterpenes for northern red oak (*Quercus rubra*), eastern white pine (*Pinus strobus*), red pine (*Pinus resinosa*),

and American beech (*Fagus grandifolia*) measured during CABINEX 2009 are 0.16, 0.38, 0.56, and 7.46 μg C g^{-1} h^{-1}, respectively. For beech, the predominant emission is *d*-limonene (27 %), followed by sabinene (17 %), α-pinene (12 %), and cymene (12 %). *Ortega et al.* (2007) measure a mean basal emission rate for paper birch (*Betula papyrifera*) of 0.5 μg C g^{-1} h^{-1}. For white and red pine, we scale the emission factors by 2.56 (*Perterer and Körner*, 1990) to account for the conversion from projected to total leaf area. We sum these species contributions and split this total monoterpene emission factor into the RACM VOC species API (56.5 %, or 0.086 nmol m^{-2} leaf area s^{-1}) and LIM (43.5 %, or 0.066 nmol m^{-2} leaf area s^{-1}) according to the measured fractional contribution of similar species.

We note that these emission estimates are based on available data from the site collected by several investigators over several seasons. Due to the high variability seen in these data, it is difficult to define representative values particularly given the cool conditions during the summer of 2009. Previous studies have noted that emission factors can vary based on prior temperatures on the span of weeks (*Pétron et al.*, 2001) and can vary based on the plants acclimation, particularly for isoprene (*Hanson and Sharkey*, 2001). Consequently, these estimates may have uncertainties of a minimum of a factor of two. Measurements indicate a dependence on temperature for monoterpene emissions; therefore, we presume monoterpene emissions to be from pools within the foliage, and are, thus, scaled according to the temperature-dependent parameterization described in *Forkel et al.* (2006). Soil NO emissions are parameterized according to *Forkel et al.* (2006), following *Simpson et al.* (1995), based on an emission rate of 180 nmol m^{-2} h^{-1} observed previously at PROPHET (*Alaghmand et al.*, 2011). Foliage NO_2 emission from nitrate photolysis at the leaf surface (*Hari et al.*, 2003) is not considered in this study due to uncertainties in emission factors.

2.3.2.4 Deposition

Dry deposition of chemical species to canopy foliage ($S_{c,\mathrm{dep},i}; \mathrm{nmol\,m^{-2}\,s^{-1}}$) is parameterized following *Meyers and Baldocchi* (1988):

$$S_{\mathrm{c,dep},i}(z) \;=\; -\mathrm{LAI}(z)c_i(z)v_{\mathrm{d},i}(z) \tag{2.12}$$

where LAI and c_i are the leaf area index per unit height and concentration for gas i, respectively. Deposition velocity ($v_{\mathrm{d},i}; \mathrm{m\,s^{-1}}$) is represented by four resistances: the quasi-laminar boundary layer ($R_{\mathrm{b},i}$), stomatal (R_{s}), mesophyll ($R_{\mathrm{m},i}$), and cuticular ($R_{\mathrm{c},i}$):

$$v_{\mathrm{d},i}(z) \;=\; \frac{1}{R_{\mathrm{b},i}(z) + R_{\mathrm{s}}(z)D_{\mathrm{H_2O}}/D_i + R_{\mathrm{m},i}} + \frac{2}{R_{\mathrm{b},i}(z) + R_{\mathrm{c},i}}. \tag{2.13}$$

where $D_{\mathrm{H_2O}}/D_i$ is the ratio of the molecular diffusivities of water to gas i (*Gao et al.*, 1993). $R_{\mathrm{b},i}$ is a function of $D_{\mathrm{H_2O}}/D_i$ and the layer-mean horizontal wind $\bar{u}$ (*Meyers*, 1987):

$$R_{\mathrm{b,i}}(z) \;=\; \frac{r_{\mathrm{b}}(z)}{D_{\mathrm{H_2O}}/D_i}. \tag{2.14}$$

where

$$r_{\mathrm{b}}(z) \;=\; \begin{cases} 500 & : \bar{u}(z) \le 0.01\ \mathrm{m\,s^{-1}} \\ 180\sqrt{l/\bar{u}(z)} & : \bar{u}(z) > 0.01\ \mathrm{m\,s^{-1}} \end{cases} \tag{2.15}$$

given an estimated typical leaf length l of 8 cm. During the day, R_{s} is dependent on light, leaf temperature, and water potentials following *Jarvis* (1976):

$$R_{\mathrm{s}} = R_{\mathrm{s,min}}(1 + \beta/I) * \frac{g}{h} \tag{2.16}$$

where $R_{\mathrm{s,min}}$ is the minimum stomatal resistance ($90\,\mathrm{m\,s^{-1}}$), β is the visible irradiance at 2 $R_{\mathrm{s,min}}$ ($200\,\mathrm{W\,m^{-2}}$), I is the visible irradiance (i.e., PAR), g is a correction for temperature, and h is a correction for leaf water potential. At night, R_{s} is equivalent to the cuticular resistance for O_3 ($R_{\mathrm{c,O_3}} \approx 3000\,\mathrm{m\,s^{-1}}$, *Wesely*, 1989) at night. $R_{\mathrm{m},i}$

and $R_{c,i}$ are parameterized according to *Wesely* (1989) as a function of the Henry's law constant H_i^* and a reactivity factor $f_{0,i}$ describing the extent that gas i decomposes in the plant mesophyll relative to O_3, ranging from non-reactive ($f_{0,i} = 0$) to full decomposition ($f_{0,i} = 1$, i.e. O_3):

$$R_{m,i} = (H_i^*/3000 + 100 f_{0,i})^{-1} \tag{2.17}$$

$$R_{c,i} = R_{c,O_3}(10^{-5} H_i^* + f_{0,i})^{-1}. \tag{2.18}$$

$f_{0,i}$ follows *Wesely* (1989) with the exception of MACR and HCHO, which are set to that of O_3 ($f_{0,i} = 1$) in response to recent suggestions that oxidized VOC can decompose in the leaf more rapidly than previously believed (*Karl et al.*, 2004, 2010). Following this change, CACHE simulates canopy-integrated deposition velocities for MACR within the expectations of *Karl et al.* (2010, $v_{d,\mathrm{MACR}} < 2.4\ \mathrm{cm\,s^{-1}}$) and comparable to that of O_3 (Fig. 2.3). H_2O_2 deposition rates are consistent with previous modeling studies, yet may be underestimated according to recent observational studies (*Ganzeveld et al.*, 2006). Deposition to the ground follows *Gao et al.* (1993).

2.3.2.5 Advection

Horizontal advection of anthropogenic NO_x and long-lived VOC is represented in CACHE as a function of wind direction. *Cooper et al.* (2001) attribute elevated concentrations of O_3, CO, NO_x, and other oxidized nitrogen species (NO_z) observed at PROPHET to southerly flow from Chicago or Detroit and lower mixing ratios to flow from clean Canadian air masses over the Great Lakes. We estimate the direction-dependent advection rate of eight RACM species (NO_2, HCHO, MACR, KET, HC3, HC5, OLT, and OLI; see *Stockwell et al.* (1997) for full definitions) according to the geographical location of PROPHET relative to nearby major urban centers. Chicago (pop. $\sim$ 2.9 million) and Detroit (pop. $\sim$ 950 000) are the major contributors of an-

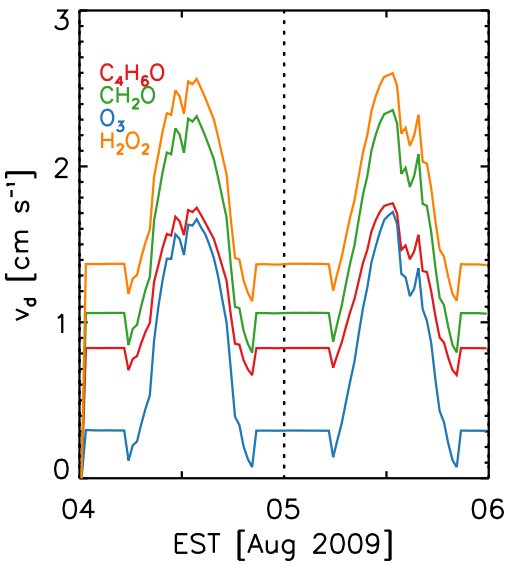

Figure 2.3: Simulated canopy-integrated deposition velocity (v_d) for methacrolein (C_4H_6O), formaldehyde (CH_2O), ozone (O_3), and hydrogen peroxide (H_2O_2).

thropogenic emissions affecting northern Michigan, with emission inventories for NO_x and VOC totaling over 20 000 kg day^{-1}, whereas peak NO_x and VOC emissions from Milwaukee (pop. $\sim$ 950 000) total in the range of 12 500–15 000 kg day^{-1} (*LADCO*, 2010). Therefore, we presume signatures of anthropogenic advection observed at PROPHET to be more pronounced with air originating in Chicago or Detroit over Milwaukee by assuming the strongest advection rates when winds are directly from the south. Westerly advection from Lake Michigan has been associated with lower isoprene concentrations than advection from forests to the south (*Sillman et al.*, 2002); therefore, we add advection of biogenic HCHO and MACR from isoprene oxidation under southerly winds. We incorporate advection of the above species between the heights 45–106 m (22–26 model levels) at the hourly, wind-direction-dependent rates shown in Table 2.2. Measured NO_2, HCHO, and MACR concentrations are used to tune advection rates for the model scenario that incorporates both the revised turbulence scheme and RACM-MIM chemistry (hereafter, the MIX+MIM case). Due to

Table 2.2: Advection rates for NO_x, VOC, and other hydrocarbons as a function of wind direction. Rates (in ppbv h^{-1}) are scaled by the geostrophic wind speed.

RACM species name	90–135°, 225–270°	135–225°
NO_2	0.05	0.25
MACR	0.00	1.00
HCHO (anthropogenic)	0.00	0.03
HCHO (biogenic)	0.00	1.00
KET	0.00	0.25
HC3	0.00	2.50×10^{-4}
HC5	0.00	0.25
OLT	0.00	0.13
OLI	0.00	0.01

the lack of ambient observations, anthropogenic hydrocarbon RACM categories, OLI, OLT, KET, HC3, and HC5, are added to reflect average concentrations of regional pollution events.

2.3.2.6 Case study: 4–5 August

The case study simulation period includes 48 h starting at 00:00 Eastern Standard Time (EST) on 4 August 2009 and ending at 23:59 EST on 5 August 2009. This two-day period offers the clearest daytime skies within the period when the most chemistry observations are available. We select these clear-sky days because they represent the time period most conducive to BVOC emissions and photochemistry, as well as providing the best measured-modeled agreement for the turbulence parameterization. NCEP surface reanalysis indicates a weak frontal passage occurring at ∼07:00 EST on 4 August (Fig. 2.1), visible in the observed wind direction (Fig. 2.2) through a shift from southerly to northwesterly winds. Back-trajectory data (Fig. 2.1) show that air originated in northern Illinois (southwest of the PROPHET site) prior to the frontal passage. Following the frontal passage, the source region ranges from northern Minnesota and southwestern Ontario, Canada (west and northwest of the

site, respectively). This meteorological scenario allows us to evaluate our advection scheme presented in Sect. 2.3.2.5 and the ability of the model to capture the shift from polluted- to clean-air advection, while also providing a good comparison between chemistry at PROPHET under the influence of regional transport versus predominantly local chemistry.

2.4 Results and discussion

We compare micrometeorological and chemistry observations from CABINEX 2009 against CACHE simulations during the 4–5 August 2009 case period using four model scenarios:

1. BASE: a control run in which turbulence follows $K_{\mathrm{H,mod}}$ (Eq. 2.5) alone and chemistry is according to RACM;

2. MIX: sensitivity of the model to turbulence is tested by modifying $K_{\mathrm{H,mod}}$ with $K_{\mathrm{H,obs}}$ (Eq. 2.8) and R (Eq. 2.11) to account for near-field effects (Sect. 2.3.2.1), while using BASE chemistry;

3. MIM: sensitivity of the model to varying treatments of isoprene degradation is tested by replacing RACM with RACM-MIM while using BASE turbulence; and

4. MIX+MIM: the combined effects of enhanced turbulence and biogenic representation are examined by applying MIX turbulence and MIM chemistry.

We first evaluate the modifications made to the turbulent exchange parameterization implemented in the MIX model scenario (Sect. 2.4.1), followed by an analysis of model-measurement comparisons throughout the canopy and the surface layer (to approximately 3 h) for O_3 and NO_x (Sect. 2.4.2), BVOC and their oxidation products (Sect. 2.4.3), and HO_x concentrations and OH reactivity (Sect. 2.4.4).

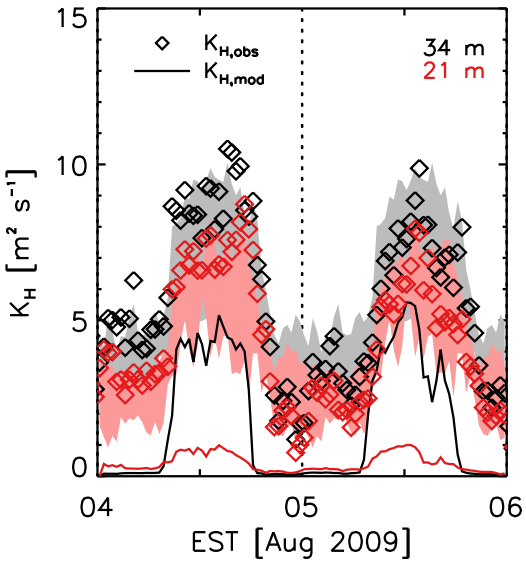

Figure 2.4: Observed ($K_{\mathrm{H,obs}}$, given by Eq. (2.8, diamonds)) and modeled ($K_{\mathrm{H,mod}}$, given by Eq. (2.5), solid lines) time series of the turbulent exchange coefficient in the upper-canopy (20.6 m, 0.9 h, red) and above the canopy (34 m, 1.5 h, black) for 4–5 August 2009. Standard deviations of the mean diurnal cycle of $K_{\mathrm{H,obs}}$ for the sunny and partly sunny days (21, 29 July, 2, 4, 5, and 7 August) are shaded. $K_{\mathrm{H,obs}}$ is calculated using sonic anemometer estimations of u_* and σ_w (see Sect. 2.3.2.1).

2.4.1 Evaluation of turbulent exchange

We estimate observed eddy diffusivity ($K_{\mathrm{H,obs}}$, Fig. 2.4) from sonic anemometer measurements (Eq. 2.8) at two heights on the PROPHET tower (0.9 h and 1.5 h) for the 4–5 August case study. At 34 m, $K_{\mathrm{H,obs}}$ has a strong diurnal cycle ranging from 3 $\mathrm{m^2\,s^{-1}}$ at night to 10 $\mathrm{m^2\,s^{-1}}$ at midday with nighttime and daytime standard deviations of around 1 and 2 $\mathrm{m^2\,s^{-1}}$, respectively. $K_{\mathrm{H,obs}}$ in the upper canopy is only 1–3 $\mathrm{m^2\,s^{-1}}$ lower than above the canopy, with a similar magnitude of standard deviations. The majority of the canopy foliage resides below the 0.9 h measurement, and the absence of lower canopy micrometeorological measurements is a limiting factor in our estimates of in-canopy mixing.

The original CACHE parameterization of $K_{\mathrm{H,mod}}$ (Eq. 2.5) is below one standard

deviation of $K_{\mathrm{H,obs}}$ at both measurement heights 95 % of the simulation time (Fig. 2.4). At 1.5 h, daytime $K_{\mathrm{H,mod}}$ is underestimated by a factor of two, whereas nighttime values are two orders of magnitude below $K_{\mathrm{H,obs}}$. $K_{\mathrm{H,obs}}$ at 0.9 h are an order of magnitude greater than model estimates over the full simulation period. In addition, the modeled onset of the stable nocturnal boundary layer, represented by the shift from higher, buoyancy-driven mixing to lower, mechanically-driven mixing at the end of the day, occurs two hours earlier and more abruptly than observed. This suggests that the empirical piecewise stability function (Eq. 2.7) may inadequately capture the formation of the stable layer and/or its effect on turbulence.

We evaluate the MIX turbulence scheme by comparing the BASE and MIX model simulations against observed time series of near-canopy temperatures (Fig. 2.5) and midday vertical profiles of K_{H}, temperature, primary BVOC (isoprene and monoterpenes), and BVOC oxidation products (formaldehyde, MACR+MVK, and acetaldehyde) (Fig. 2.6). Following the frontal passage, which CACHE cannot simulate, near-canopy temperatures are reproduced by the model, especially in the MIX simulation (Fig. 2.5). This indicates that the radiation-driven heating source and vertical exchange of heat at the surface are captured fairly well by the model. $K_{\mathrm{H,obs}}$, which drives in- and near-canopy turbulence for the MIX case, is twice as large as the BASE-case turbulence (i.e. $K_{\mathrm{H,mod}}$) at 1.5 h and an order of magnitude larger at 0.9 h (Fig. 2.6a), indicating missing turbulence such as coherent structures (as observed during CABINEX 2009, *Steiner et al.*, 2011), counter-gradient terms, or other processes that cannot be captured by the original K-theory parameterization. The standard deviations of the $K_{\mathrm{H,obs}}$ (denoted by the error bars) are based on daily averages for the sunny and partly sunny days during the period of available u_* and σ_w measurements (21, 29 July, 2, 4, 5, and 7 August). Of these "clear-sky" days, observed turbulence was stronger than average on 5 August, leading to nearly uniform temperatures with height that is well captured by the MIX model case (Fig. 2.6b).

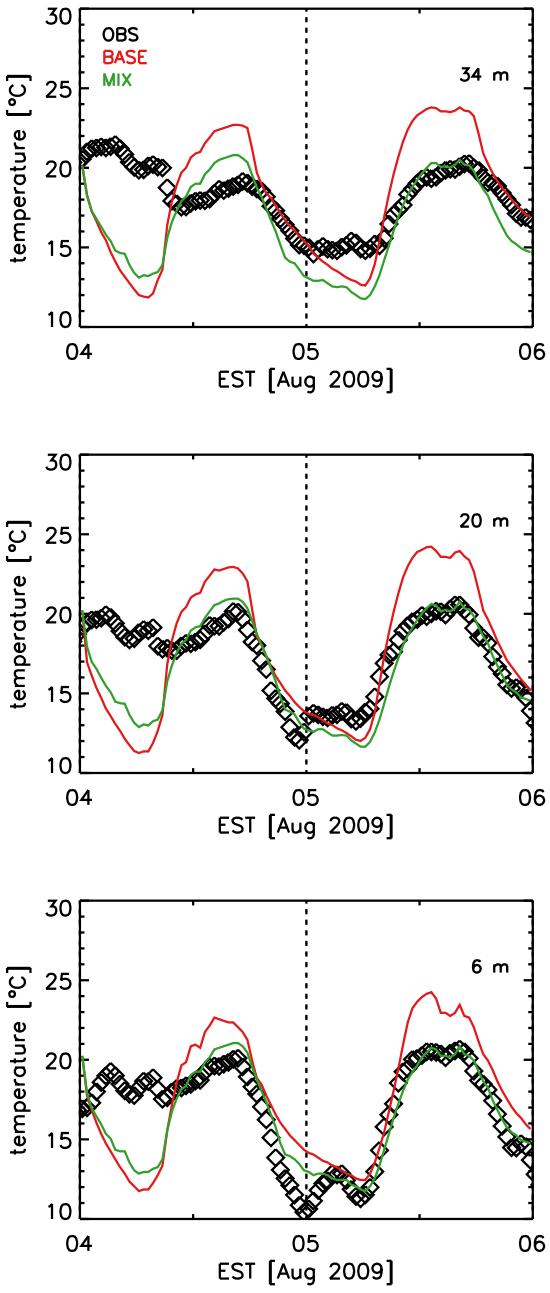

Figure 2.5: Measured and modeled temperatures at 34, 20.4, and 6 m.

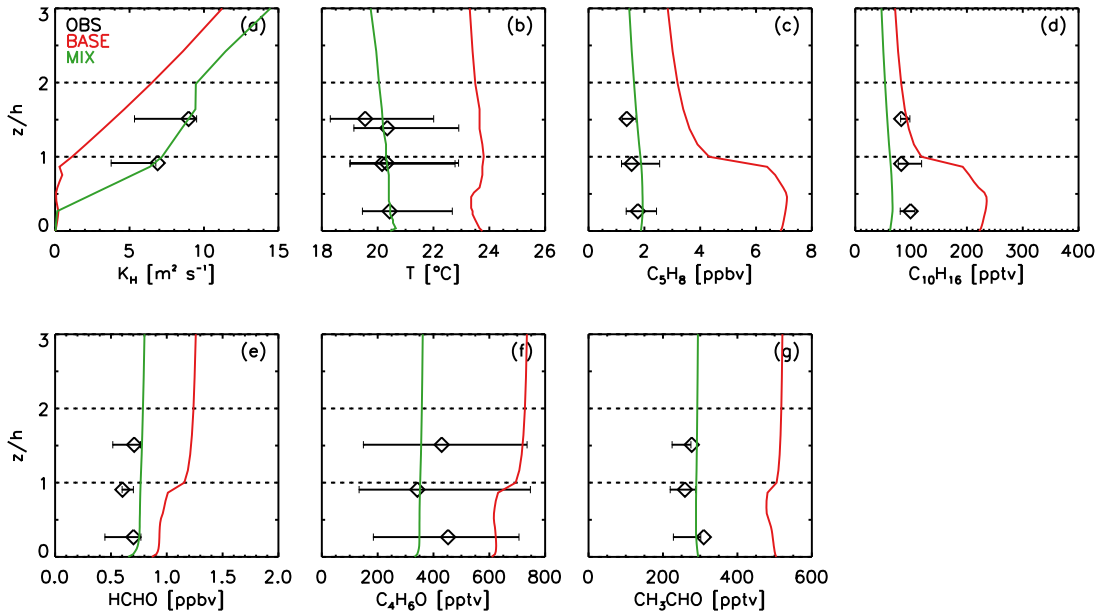

Figure 2.6: Measured and modeled vertical profiles of **(a)** eddy diffusivity, **(b)** temperature, **(c)** isoprene, **(d)** monoterpenes, **(e)** formaldehyde, **(f)** MACR+MVK, and **(g)** acetaldehyde at 14 EST 5 August 2009. Whiskers denote the standard deviations for the sunny and partly sunny days (21, 29 July, 2, 4, 5, and 7 August).

In the BASE scenario, $K_{\mathrm{H,mod}}$ decreases to $0.1\,\mathrm{m^2\,s^{-1}}$ at the displacement height, creating an unrealistic artificial boundary. This is an artifact of the use of two different equations to construct the in- and above-canopy wind profiles and turbulence schemes, which creates a discontinuity at the forest-atmosphere interface and prevents BVOC transport out of the canopy sub-layer in the model. Temperature (Fig. 2.6b) decreases with height within and above the canopy according to the observations, yet the BASE model case imposes a stabilizing inversion induced by heating of the upper canopy. Consequently, in-canopy mixing is weak in the BASE simulation. With regard to the observations, we note that the vertical gradients may vary by instrument placement in the canopy.

Observed midday vertical gradients of BVOC and oxidation products are also compared against the BASE and MIX simulations in Fig. 2.6c–g. Enhanced turbu-

lence effectively improves the agreement of modeled and measured concentrations for the more reactive species (isoprene and monoterpenes) by reducing in-canopy concentrations and weakening the vertical gradient. For the longer-lived species (formaldehyde, MACR+MVK, and acetaldehyde), concentrations are decreased and gradients are weakened by the enhanced mixing, leading to a nearly uniform modeled vertical profile in the lowest 60 m (3 h). Oxidized VOC (e.g., MACR+MVK) can deposit as efficiently as O_3 (*Karl et al.*, 2010), yet simulated gradients of these species in the MIX case are weak. This suggests that either a compensation point has been reached or there are some primary sources of oxidized VOC from the forest canopy.

Above the canopy (not shown), CACHE accurately captures the characteristic features of the PBL, as indicated by the diurnal cycles of stability and turbulence. During the day, surface heating from canopy absorption of solar radiation induces instability and buoyancy-driven mixing, generating the convective mixed layer. The maximum height of the mixed layer varies with surface heating, but generally peaks mid-day around 1 km above the surface with a maximum strength occurring at approximately 500 m as modeled in *Gao et al.* (1993). At the end of the day, buoyant turbulence ceases in the absence of surface heating, and the stable nocturnal boundary forms beneath a well-mixed residual layer. CACHE does not explicitly model conditions in the free atmosphere nor the existence of an entrainment zone along a capping inversion. Therefore, our study focusses on exchange across the forest-atmosphere interface where we expect little influence from these upper PBL features.

2.4.2 O_3 and NO_x

We assess the performance of the model in simulating near-canopy O_3, NO_2, and NO during the 4–5 August case period (Fig. 2.7). At all three heights (6, 20.4, and 34 m), observed O_3 mixing ratios peak at 40–50 ppbv shortly after the start of the simulation period and subsequently drop by 20 ppbv in 5 h. At that time, backward

trajectories produced by the Hybrid Single Particle Lagrangian Integrated (HYSPLIT) model (Fig. 2.1) indicate that air parcels observed at PROPHET prior to 08:00 EST on 4 August originated near Milwaukee and Chicago, and parcels arriving after 08:00 EST originated in northern Minnesota and Canada. Additionally, the local wind direction observed at PROPHET (Fig. 2.2) shifted from southerly to northwesterly over a 3- to 5-h period just after midnight. This transport, concurrent with a peak in observed NO_2 concentrations (Fig. 2.7), highlights the influence of large-scale advection on local O_3 and NO_x concentrations. Despite the inclusion of the same advection scheme in the BASE and MIX cases, the BASE-simulated O_3 is reduced after initialization, while the concentrations in the MIX case increase to near-observed values. This indicates the influence of turbulent mixing on advection from aloft. While CACHE captures the enhanced polluted advection from Chicago and Milwaukee, we note that the wind-direction-dependent advection scheme does not consider the removal of polluted air from clean-air advection, thus CACHE does not fully capture the observed decreased in O_3 following the shift in wind direction and reduced influence from Chicago. Another possibility is that the initial conditions are not fully relaxed by this point in the simulation.

Under clean-air advection (i.e. following the frontal passage discussed in Sect. 2.3.2.6), above- (Fig. 2.7a) and upper-canopy (Fig. 2.7d) O_3 measurements show only small variability (e.g., approximately 10 ppbv) over the remainder of the simulation. BASE simulates a strong diurnal cycle, whereas MIX shows no clear diurnal cycle, indicating that locally produced ozone is also highly sensitive to mixing. In the lower canopy (Fig. 2.7g), O_3 measured after the frontal passage is more variable, which is not captured by any of the model simulations. Wind directions are weakly variable from the west to northwest, showing no relationship with changes in O_3 concentration, suggesting that advection does not explain the observed variability. At the minima of the variability, lower-canopy concentrations are lower than the upper two measurements,

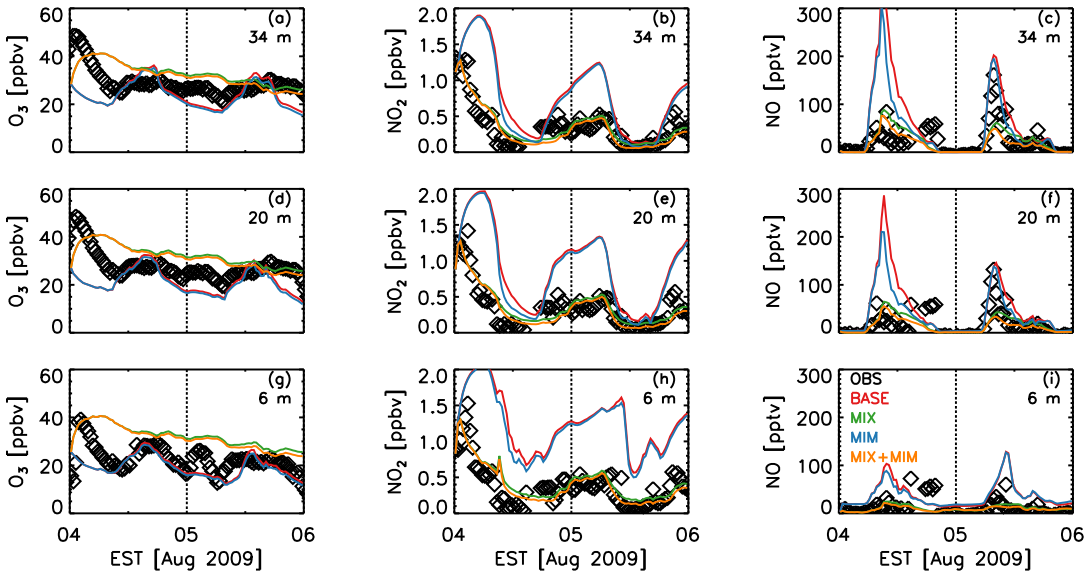

Figure 2.7: Measured versus modeled time series for **(a, d, g)** O_3, **(b, e, h)** NO_2, and **(c, f, i)** NO at 34 m, 20.4 m, and 6 m for the 4–5 August 2009 simulation period, showing observed concentrations (OBS, black) and modeled concentrations as follows: the original model configuration with modeled turbulence and RACM chemistry (BASE; red); the corrected mixing simulation with RACM chemistry (MIX; green); the original mixing scheme with RACM-MIM chemistry (blue; MIM); and the revised mixing scheme with RACM-MIM chemistry (MIX+MIM; orange).

indicating the potential relevance of an important O_3 canopy sink. In the canopy layer, deposition is the primary sink of O_3, exceeding modeled chemical loss by a factor of 10. Modeled O_3 deposition velocity peaks mid-day at $1.6\,\mathrm{cm\,s^{-1}}$ (Fig. 2.3), which is higher than other modeling studies ($0.4\,\mathrm{cm\,s^{-1}}$, *Finkelstein et al.*, 2000; *Stroud et al.*, 2005), yet yields deposition fluxes that compare quite well with previous observations at PROPHET (15–$20\,\mathrm{nmol\,m^{-2}\,s^{-1}}$, *Hogg et al.*, 2007). This suggests O_3 deposition is fairly well represented in the model. However, midday ozone deposition velocity increases by less than 0.02 % with enhanced mixing, indicating that deposition is not the main driver in the large concentration differences in the BASE and MIX ozone simulations. Lastly, we note that micrometeorological observations were not available in the lower canopy and may be underestimated by the MIX simulation, leading to an uncertainty in lower-canopy turbulence. Consequently, we are unable to evaluate whether these uncertainties in mixing can explain the lower canopy variability. In contrast with turbulent mixing, the enhancement in isoprene degradation between BASE and MIM show little impact on O_3 concentrations, indicating that O_3 is more sensitive to mixing than chemistry.

Like O_3, observed NO_2 displays a signature of anthropogenic advection on the early morning of 4 August. In the model, we have tuned the NO_2 advection rate (Sect. 2.3.2.5) to capture the higher concentrations observed at the beginning of the simulation and subsequent lower concentrations as the winds shift following the frontal passage. Observed NO_2 ranges from 1.2 ppbv at the beginning of the simulation to approximately 0.5 ppbv on the second night, with midday concentrations of less than 0.1 ppbv after photolysis. MIX+MIM underpredicts NO_2 slightly in the early part of the second night, likely due to an oversimplification in our NO_2 advection scheme, missing downward transport from the residual layer, or an additional NO_2 source (e.g., emission from foliage). NO mixing ratios show a distinct diurnal pattern in the observations, peaking at nearly 180 pptv around mid-morning 5 August at 34 m,

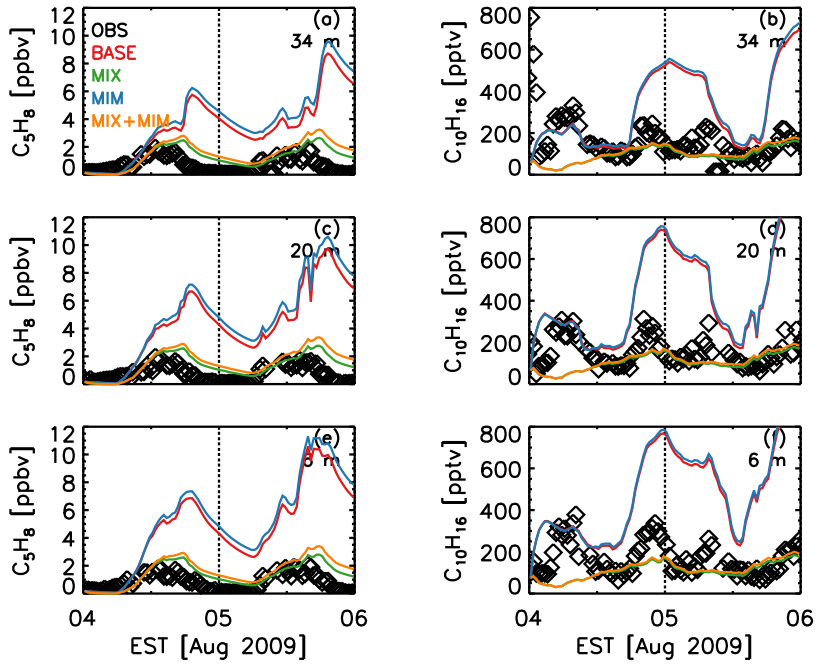

Figure 2.8: Same as Fig. 2.7, but for **(a, c, e)** isoprene and **(b, d, f)** monoterpenes.

consistent with measurements taken over multiple years at PROPHET (*Alaghmand et al.*, 2011). At night, mixing ratios reach as low as 1–5 pptv. The model reproduces the NO diurnal cycle well at the top of the canopy in all model scenarios, with concentrations overestimated on the first day in the BASE and MIM cases and good agreement for the MIX cases, and underestimated on the second day in the MIX and MIX+MIM cases. NO concentrations decrease with increasing canopy depth as a result of light attenuation lowering the NO yields from NO_2 photolysis. All four model scenarios are able to capture this effect of attenuation reasonably well.

2.4.3 Biogenic VOC and oxidation products

Figure 2.8 evaluates the four model scenarios against observations for primary BVOC, isoprene and monoterpenes. Observations of isoprene show a strong diurnal cycle ranging from 0.2 ppbv at night to up to 2–3 ppbv at midday at all height levels.

MIM simulations show slightly increased concentrations of isoprene over the BASE simulation, owing to lower OH availability as enhanced MACR+MVK concentrations increase the competition for OH. However, the BASE and MIM model scenarios have difficulty reproducing this diurnal pattern in two respects: (1) modeled concentrations increase later in the morning than observed, and (2) a rapid increase in concentrations occurs at sunset, causing a large discrepancy between the model and observations. Near the ground, this modeled pattern is dampened with a less pronounced evening peak and better drawdown of concentrations at night. Such a pattern has been frequently observed (cf. *Martin et al.*, 1991), and is prevalent in many modeling studies (e.g., *Sillman et al.*, 2002; *Forkel et al.*, 2006; *Barkley et al.*, 2011), which attribute the end-of-the-day increase to decreased mixing associated with the development of the stable nocturnal boundary layer. As noted in Sect. 2.4.1, CACHE captures the formation of the stable layer through the development of positive potential temperature gradients and highly reduced turbulent mixing below a well-mixed residual layer. In the BASE simulation, however, rapidly reduced mixing associated with an early and abrupt onset of the stable layer (Sect. 2.4.1, Fig. 2.4) leads to accumulation of isoprene (and other BVOC) near the canopy at the end of the day, further indicating the inability of the stability parameter (Eq. 2.7) to realistically capture the stable layer formation and its effect on turbulent exchange. As demonstrated in the MIX simulation, amplified turbulence and the gradual dissipation of daytime buoyancy-forced turbulence dampens these accumulations. We note, however, that underestimations of modeled in-canopy turbulence due to a lack of micrometeorological measurements in the lower canopy may result in insufficient exchange across the forest-atmosphere boundary. Our evaluation of the BASE and MIX turbulence schemes presented in Sect. 2.4.1 discusses several observed model-measurement discrepancies in the BASE K_{H} that are corrected in the MIX scenario, including the end-of-day decrease in mixing at sundown. This indicates the sensitivity of the top-of-canopy BVOC flux to

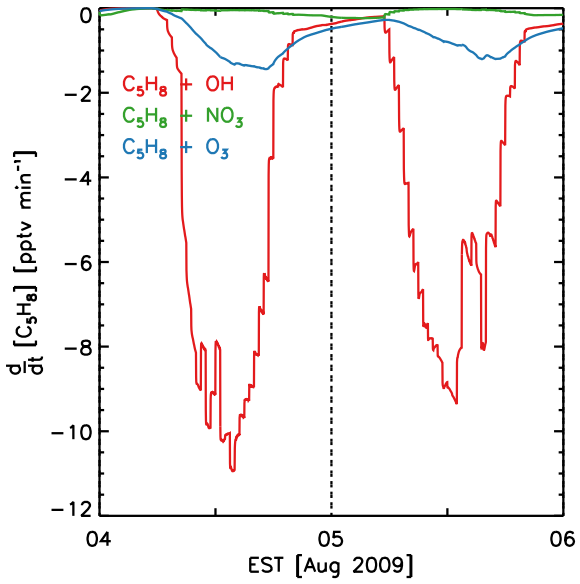

Figure 2.9: Modeled isoprene loss rates with respect to reaction with OH, NO_3, and O_3 at 34 m from the MIX case.

turbulence and emphasizes the importance of an accurate representation of in-canopy mixing in models. Overall, these results highlight the importance of an accurate representation of in-canopy mixing in models and the need for improved simulation the transition from the convective to the nocturnal PBL.

While enhanced mixing improves the diurnal evolution of isoprene, modeled mixing ratios exceed observations on the second day by 1–3 ppbv, likely due to an underestimate of isoprene oxidation. Oxidation of isoprene in the model is primarily controlled by reaction with OH, with loss rates in the model peaking at midday around 11 pptv min^{-1} (Fig. 2.9). Oxidation by ozone follows at much smaller rates (up to 2 pptv min^{-1} around sunset) and small contributions by loss with the nitrate radical at night (approximately 0.5 pptv min^{-1}). Simulated NO_3 mixing ratios at 34 m (not shown) peak at 4 pptv the first night under elevated NO_2 concentrations from regional transport and decrease to 0.3 pptv on the second night when chemistry is dominated by local emissions. Past estimates of NO_3 at PROPHET range from

0.4 pptv (*Pratt et al.*, 2012) to 2–3 pptv (*Faloona et al.*, 2001), although we note that NO_3 has not been measured at the site before, making it difficult to evaluate the model. The primary model NO_3 source is the nighttime oxidation of NO_2 by O_3, yet observed NO_2 concentrations at the site remain relatively low; therefore, we should expect relatively low concentrations of NO_3 and low isoprene-NO_3 oxidation rates. A potential explanation for the lack of nighttime oxidation may be OH concentrations, as discussed in Sect. 2.4.4. In addition to the effect of nighttime chemistry, *Ganzeveld et al.* (2008) suggest that downward transport of oxygenated VOC from the residual layer may lower OH availability, further reducing isoprene oxidation, particularly in the morning. This downward transport is captured in our model for oxygenated VOC during the second morning of the simulation, yet model overestimations of isoprene begin as early as sundown on the prior day, suggesting that the effect of entrained oxygenated VOC from the residual layer on OH concentrations is likely small relative to the observed discrepancies in nighttime chemistry.

Monoterpenes ($C_{10}H_{16}$) are grouped together as a total monoterpene concentration by the PTR-MS. As noted at other forest sites (*Bouvier-Brown et al.*, 2009), observations show a different diurnal cycle than isoprene. The early morning and late evening peak (Fig. 2.8) and higher concentrations at night than during the day have been attributed to high photooxidation during the daytime and an accumulation at night as these temperature-dependent emissions continue in the absence of sunlight. Above the canopy, higher concentrations of monoterpenes are observed at the beginning of the simulation, suggesting a potential advective source of terpenes to the site in the first six hours of the simulation, which is consistent with air traveling over the forested state. RACM-MIM simulates terpene concentrations to be very similar to the RACM case due to no changes in the MIM terpene oxidation scheme. As with isoprene, however, enhanced mixing greatly improves the model-measurement agreement in terms of magnitude of concentrations, though the diurnal cycle is only

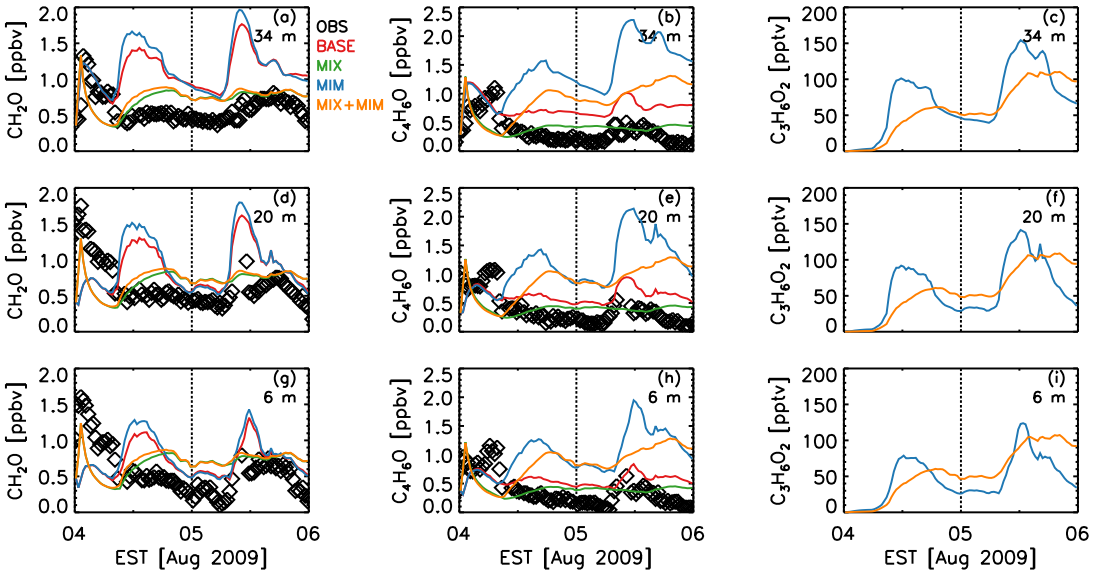

Figure 2.10: Same as Fig. 2.7, but for **(a, d, g)** formaldehyde, **(b, e, h)** MACR+MVK, and **(c, f, i)** hydroxyacetone. Observations of hydroxyacetone are not available.

weakly captured.

Formaldehyde (HCHO) is an important VOC oxidation product and is typically produced in relatively large quantities from the oxidation of isoprene. While anthropogenic VOC can also provide a substantial source of HCHO (*Pang et al.*, 2009), their effect on local HCHO concentrations observed at the PROPHET site is minor (*Sumner et al.*, 2001), unless under advective conditions from the south. Observed mixing ratios at the site are 0.5–1 ppbv (Fig. 2.10), reflecting values that are lower than the 1999 field campaign observations (0.5–12 ppbv, *Sumner et al.*, 2001), consistent with the expected reduced photochemistry in the summer of 2009. An advection source is apparent from the higher HCHO concentrations both above and below the canopy (Fig. 2.10a, d, g) at the beginning of the simulations, as formaldehyde generally peaks midday from local chemistry. When an advective HCHO source is added at 45–106 m, measured-modeled comparisons improve above the canopy but not below the canopy,

suggesting either that there is in-canopy production that the model does not capture, in-canopy deposition is overestimated, or mixing within the canopy is stronger than simulated. HCHO midday deposition velocity is higher than other studies ($2.3\,\mathrm{cm\,s^{-1}}$ in our model as compared to $1.5\,\mathrm{cm\,s^{-1}}$ in *Sumner et al.* (2001)), yet the model still overestimates HCHO in all simulations at all heights, even after enhancing the in-leaf reactivity to that of O_3, as suggested for other oxidized VOC (*Karl et al.*, 2010). This indicates the possible existence of a compensation point, similar to that observed of other compounds (e.g., NO_2, acetone, and methanol, *Ganzeveld et al.*, 2002, 2008), at which the concentration in the plant mesophyll matches or exceeds that of the ambient air, restricting further deposition and potentially inducing emissions.HCHO deposition velocity decreases by less than $0.1\,\mathrm{cm\,s^{-1}}$ with enhanced mixing, as with that of O_3. When advection is not playing a role (the second day of the simulation), modeled HCHO exhibits a diurnal cycle with higher concentrations during the day especially in the BASE and MIM cases. Both above and below the canopy, the change to MIM increases midday HCHO concentrations by about 15 % due to larger HCHO yields from BVOC oxidation (*Geiger et al.*, 2003). MIM makes additional HCHO from the isoprene peroxy self-reaction (ISOP+ISOP), plus the new methacrolein peroxy radicals (MACP). Enhanced mixing (MIX and MIX+MIM) weakens the diurnal pattern of HCHO, better reflecting observations.

Other key BVOC oxidation products are the lumped species methacrolein and methyl vinyl ketone (MACR+MVK or C_4H_6O). These compounds are detected at the same nominal mass on the PTR-MS and are also lumped in the RACM mechanism. Observed concentrations peak in the early portion of the simulation both above and below the canopy (Fig. 2.10) due to advection of oxidation products from the south. Adding an advective source of MACR aloft (Table 2.2) improves measured-modeled agreement at the beginning of the simulation at all measurement heights. The MIX case improves concentrations as compared to observations, yet removes the

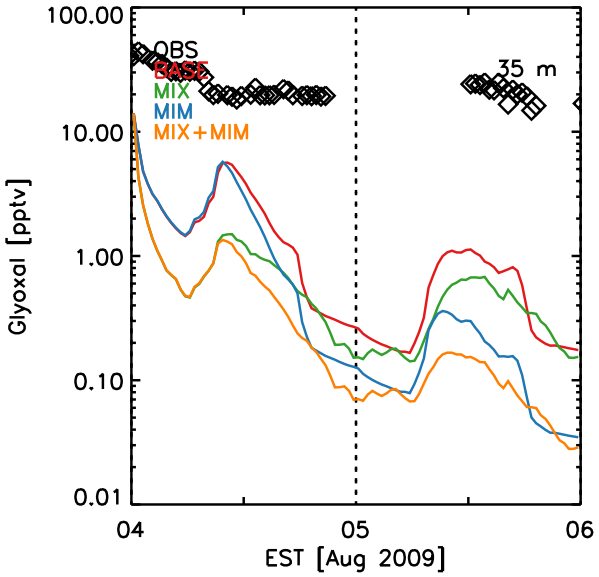

Figure 2.11: Measured and modeled glyoxal concentrations during the 4–5 August 2009 simulation period.

observed diurnal pattern. Changing to the MIM mechanism doubles the BASE-case concentrations of MACR+MVK due to the increased yield in MACR+MVK by the reaction of first-generation oxidation products of isoprene with NO. Consequently, modeled concentrations of the MACR RACM-MIM surrogate overestimate measured MACR+MVK by a factor of three throughout the profile. This finding is consistent with chamber study comparisons of RACM and RACM-MIM by *Geiger et al.* (2003), who attribute the result to measurements only accounting for MACR+MVK, while the RACM species also includes all other unsaturated C_4 carbonyls. Past studies suggest that dry deposition rates for MACR+MVK may be underestimated (*Karl et al.*, 2004, 2010; *Pugh et al.*, 2010), yet the modeled MACR+MVK deposition velocity at mid-day ($1.6\,\mathrm{cm\,s^{-1}}$, Fig. 2.3) compares well with observations by *Misztal et al.* (2011, 1–$2\,\mathrm{cm\,s^{-1}}$) and *Karl et al.* (2010, $< 2.4\,\mathrm{cm\,s^{-1}}$) after modifying the reactivity factor for oxidized VOC following *Karl et al.* (2010). Enhanced mixing reduces the MACR deposition velocity by about 5 %.

We also evaluate the simulation of the biogenic oxidation product hydroxyacetone ($C_3H_6O_2$) added to the RACM-MIM mechanism (denoted as HACE) representing a major product of MACR+MVK oxidation. While calibrated observations of HACE are not available, the model simulates a diurnal cycle with mixing ratios ranging up to 100 pptv that decrease slightly with increased mixing (Fig. 2.10), which is slightly lower than the range of the uncalibrated measurements (200–500 pptv). Glyoxal (GLY) was also measured at the site, with mixing ratios reaching up to 25 pptv during midday, and with a clear advective signal on the first day of the simulations (Fig. 2.11). However, both RACM versions only form GLY from anthropogenic precursors and do not include the production from any biogenic species; therefore, modeled mixing ratios are on the order of 0.01–1 pptv. Observations of GLY suggest local biogenic production of GLY, a source that could be included in future models.

We compare the daytime (11:00–17:00 EST) ratios of (MACR+MVK)/isoprene and HACE/(MACR+MVK) to evaluate the ability of the RACM and RACM-MIM mechanisms to reproduce observed BVOC oxidation. Over the full field campaign (not shown), the observed (MACR+MVK)/isoprene ratio is 0.18, substantially lower than observed in the Amazon (0.44, *Karl et al.*, 2009), yet comparable to observations from previous PROPHET studies (0.12, *Apel et al.*, 2002). *Apel et al.* (2002) observe lower MACR+MVK concentrations under westerly flow associated with clean-air advection from Lake Michigan, leading to lower MACR+MVK/isoprene ratios. Additionally, as shown by comparing the ratios of MACR+MVK/isoprene with wind direction over the full two-day simulation (Fig. 2.12), we observe elevated ratios (0.71) under southerly flow associated with polluted advection. Due to this strong variability in MACR+MVK with respect to wind direction at the PROPHET site, the correlation between MACR+MVK and isoprene is substantially weaker ($R^2 = 0.25$) than observed by *Karl et al.* (2009, $R^2 = 0.86$). Figure 2.13 compares the observed daytime ratios against the four model scenarios for the second day (5 Au-

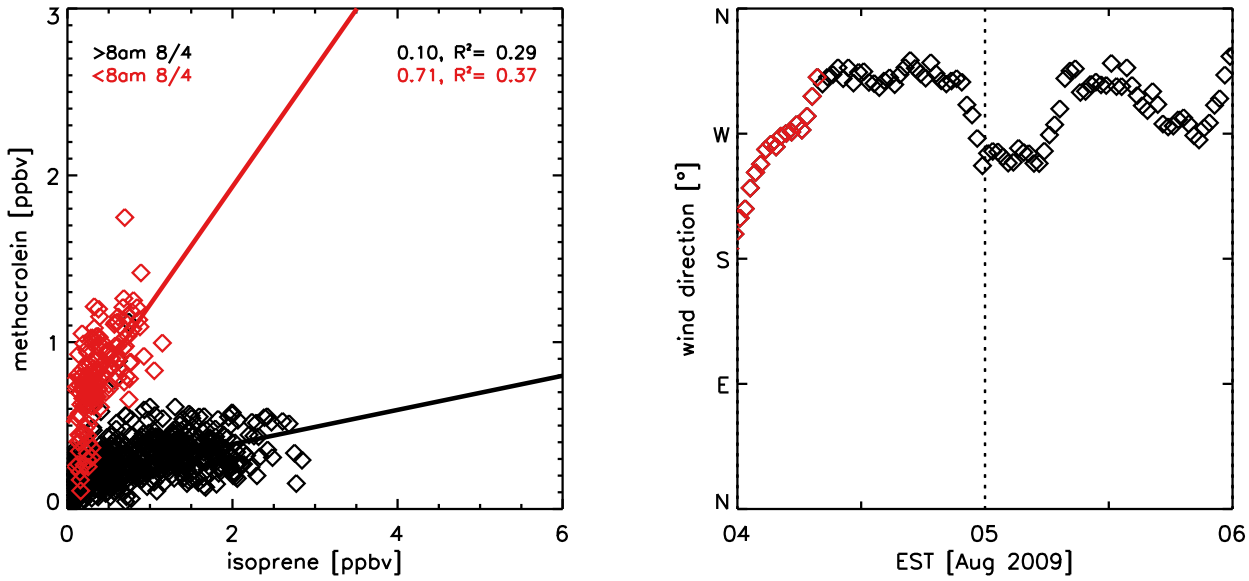

Figure 2.12: MACR+MVK/isoprene ratios for the full CABINEX 2009 campaign (1 Jul – 9 Aug, left) and the two-day case study (4–5 Aug, center). Wind direction for the two-day case study are shown at right. In the center and right plots, red values indicate observations prior to the frontal passage (approx. 8 AM), and the black values represent after the frontal passage. Slopes of the linear regressions and the correlation coefficients (R^2) are given in the upper right hand corner of the left and center figures.

gust) to examine local chemistry in the absence of pollution transport. The observed (MACR+MVK)/isoprene ratio of 0.03 is much lower than the mean daytime ratio for the full campaign (0.18), likely due to enhanced clean-air advection from the northwest (*Sillman et al.*, 2002). The BASE and MIM scenarios yield negative ratios, indicating inefficient oxidation of isoprene. This is consistent with the overestimation of isoprene by the BASE and MIM cases, particularly on the second day, as a result of inefficient mixing out of the canopy. In these scenarios, OH is depleted before isoprene is completely oxidized, leading to insufficient production of MACR+MVK given the amount of isoprene available. This is consistent with past studies, who propose the need for a OH recycling mechanism (*Lelieveld et al.*, 2008). With enhanced mixing (MIX and MIX+MIM scenarios), isoprene is oxidized more effectively leading to ratios

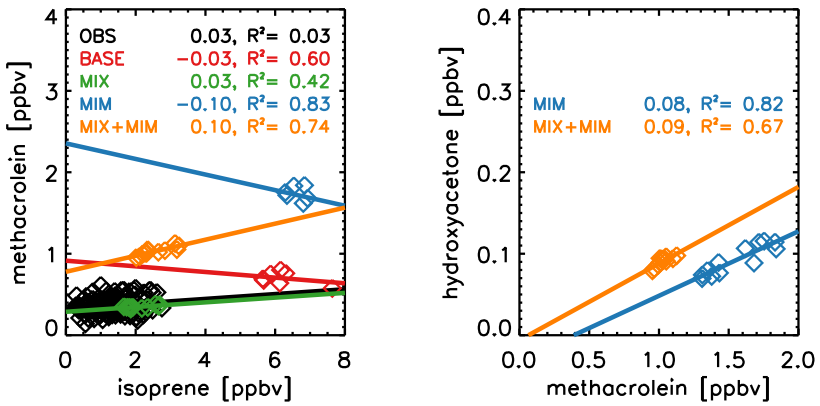

Figure 2.13: Measured and modeled correlations between MACR+MVK and isoprene (left), and hydroxyacetone and MACR+MVK (right) at 34 m for 5 August 2009 between 11:00–17:00 EST. The squared correlation coefficients (R^2) and slopes of the regression lines are given in the upper right-hand corners in colors corresponding to the appropriate model scenario.

that correlate well with observations. Additionally, the HACE/(MACR+MVK) relationship can highlight the added oxidation capacity when including the new MACR oxidation pathways in MIM. For local conditions on 5 Aug, the modeled ratios are 0.08 and 0.09 for the MIM and MIX+MIM cases, respectively, both of which are substantially lower than observed in the Amazon (0.3, *Karl et al.*, 2009) due to lower oxidant concentrations. While the MIX+MIM case ratios are lower than the MIM, we note that the correlation is weaker in the MIX+MIM case ($R^2 = 0.67$) than in the MIM case ($R^2 = 0.82$), indicating a large uncertainty with these ratios.

To summarize, the original CACHE BASE simulations strongly overestimate isoprene concentrations, particularly in the early evening and at nighttime. This is a known problem in models that occurs at all scales (e.g., 1-D models, 3-D models, etc.) and we attribute this increase at the end of the day to improper mixing in the model. The revised mixing scheme, which is based on observed friction velocities and vertical velocity standard deviations, greatly improves the simulation of primary BVOC at most model levels. Therefore, a realistic representation of boundary layer turbulence

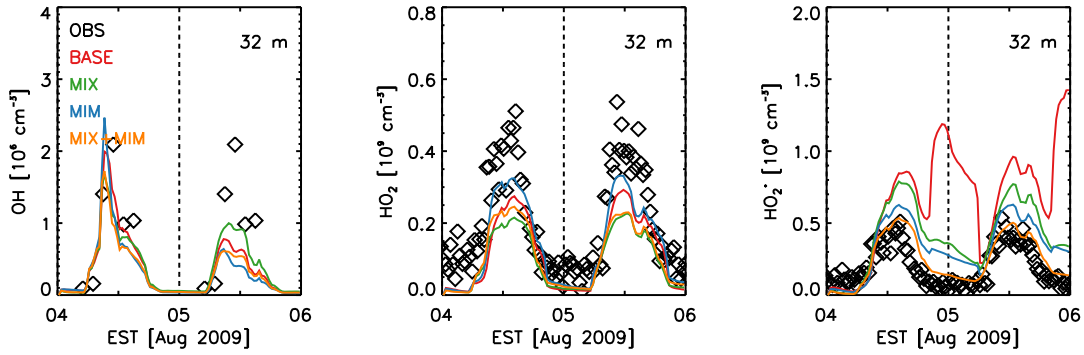

Figure 2.14: Same as Fig. 2.7, but for OH (left), HO_2 (middle), and HO_2^* (right) at 32 m.

is critical for modeling forest-canopy exchange and its effect on BVOC chemistry accurately. Oxidation products such as HCHO and MACR+MVK are overestimated by the BASE model simulations, with the greatest measured-modeled improvement resulting from the change in mixing parameterization versus the chemical mechanism. In general, the more detailed biogenic oxidation scheme (RACM-MIM) increases the oxidation products to three times more than observed, although the mechanism does improve modeled HO_x as will be discussed in the next section.

2.4.4 HO_x and OH reactivity

Modeled OH concentrations reproduce the diurnal cycle and magnitude of observed OH (1–2.5 $\times$ 10^6 molecules cm^{-3} at midday) (Fig. 2.14). Difficulties associated with transmission of laser power to the top of the tower led to few measurements of OH greater than the limit of the detection of the instrument (approximately 1 $\times$ 10^6 molecules cm^{-3}) during this time period; therefore, Fig. 2.14 displays an average diurnal cycle of OH of the two simulation days with a peak value of 2 $\times$ 10^6 molecules cm^{-3}. The model produces higher OH concentrations on the first day of simulation due to the higher oxidation from incoming advection, while modeled concentrations on the second day are approximately half the observed values. At

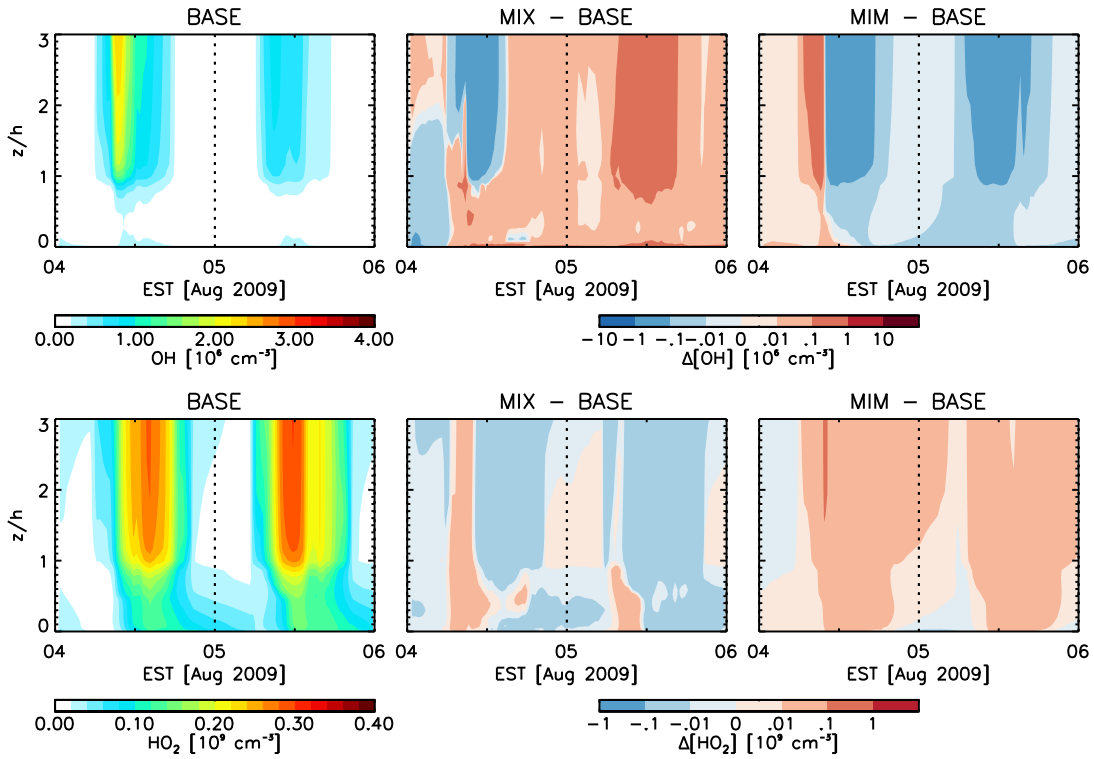

Figure 2.15: Vertical profiles of modeled OH (top) and HO_2 (bottom) for the BASE case (left) and the absolute difference between the BASE and MIX cases (middle) and BASE and MIM cases (right). Blue values indicate higher concentrations in the BASE case, and red values indicate higher concentrations in the MIX or MIM cases.

midday, the MIX and MIM cases decrease modeled OH by about 10 and 20 %, respectively, on the first day, and on day two, MIX increases modeled OH by about 10 %. From the vertical profiles (Fig. 2.15), in-canopy OH concentrations are low, suggesting small OH production rates. OH concentrations are highest above the canopy where substantial production from O_3 photolysis and subsequent reaction with H_2O occurs. In general, enhanced mixing increases the modeled OH concentrations at all heights, whereas the change from RACM to RACM-MIM decreases OH from the surface to 3 h. An exception is during the anthropogenic advection event on the morning of 4 August, when enhanced mixing increases above canopy OH and decreases OH within the canopy; implementing RACM-MIM increases OH throughout the column, due to increased production from the HO_2 + NO reaction.

For HO_2, the measurements show a strong diurnal cycle that is reproduced by the model (Fig. 2.14). In general, the model underestimates HO_2 in the BASE case simulation, with a slight increase in HO_2 from the MIM simulation. However, recent studies suggest that the detection of HO_2 radicals using chemical conversion to OH by reaction with added NO may be sensitive to the detection of a fraction of hydroxyalkyl peroxy radicals produced from the OH-initiated oxidation of alkenes (*Fuchs et al.*, 2011). Calibrations of the Indiana University FAGE instrument indicate that approximately 90 % of isoprene-based hydroxyalkyl peroxy radicals are detected in addition to HO_2, while only 5 % of propane-based alkyl peroxy radicals are detected. Given that isoprene dominates the HO_2 radical chemistry at this site, the measured HO_2 concentrations (HO_2^*) likely reflect the sum of both HO_2 and isoprene peroxy radicals (ISOP). In Fig. 2.14, we compare measured HO_2^* with a similar metric from the model ($HO_2^* = HO_2$ + ISOP) and this greatly improves measured-modeled agreement. The increase in late evening modeled HO_2^* is due to an accumulation of the ISOP radicals, an artifact from the end-of-day increase in isoprene concentrations (see Sect. 2.4.3). When changing to RACM-MIM, the reaction rate for HO_2 + ISOP

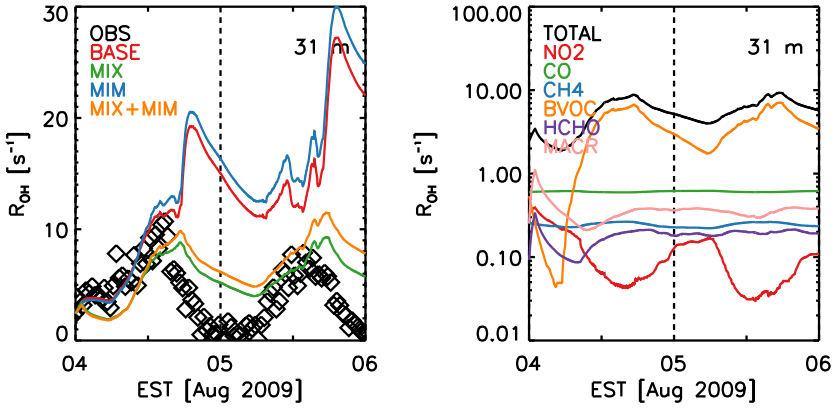

Figure 2.16: Total OH reactivity measured (OBS) and modeled (BASE, MIX, MIM, and MIX+MIM) at 30.9 m for 4–5 August 2009 (left); modeled total OH reactivity and from speciated contributions of NO_2, CO, CH_4, BVOC (ISO+API+LIM), HCHO, and MACR for the MIX case (right).

increases and the self-reaction ISOP + ISOP is explicitly added, leading to greater HO_2^* destruction and improving the model-measurement agreement. In the vertical profiles (Fig. 2.15), the model produces a strong source of HO_2 above the canopy with some in-canopy production. RACM-MIM increases HO_2 throughout the vertical profile, particularly in the daytime. The enhanced mixing (MIX case) increases both in- and above-canopy HO_2 concentrations in the morning and above the canopy during the night. Otherwise, slight decreases in HO_2 occur. During the advection event on 4 August, increased NO_x leads to decreased HO_2 in both the MIX and MIM cases due to loss with NO.

OH reactivity (R_{OH}) represents the total first order loss rate of OH (inverse of the OH lifetime). Measured R_{OH} values during CABINEX 2009 range from 0–2 s^{-1} at night to up to 10 s^{-1} during the day (Fig. 2.16, left panel), which compare well with previous measurements at PROPHET (*Di Carlo et al.*, 2004). Modeled R_{OH} is calculated by summing the product of the rate constant and reactant concentrations for all species that consume OH. Modeled R_{OH} compares best with observations for the MIX scenario, due to the poor reproduction of the observed diurnal cycle of isoprene

simulated by the BASE and MIM simulations. This again suggests the dependence of modeled R_{OH} on the vertical mixing in the model. For modeled R_{OH}, we speciate contributions from BVOC (isoprene, API, LIM) and oxidation productions (HCHO and MACR+MVK). During the afternoon, BVOC account for approximately 85 % of the reactivity in the model, followed by the CO at 15 %, whereas the oxidation products and CO dominate at night and in the early morning (Fig. 2.16, right panel). Contributions from methane and NO_2 are relatively small. *Kim et al.* (2011) note that the oxidation products can account for about 8 % of the reactivity if NO concentrations are low. However, as noted by *Kim et al.* (2011) and *Karl et al.* (2009), the R_{OH} tends to increase when photochemically aged air masses arrive at the observation site, which is evident on the first day of the simulation. Because we are including the advection of some primary anthropogenic and secondary oxidation products (Table 2.2), we correctly model this increase in R_{OH} on the first day of simulation. The second day of the simulation reflects the local conditions, with slightly lower R_{OH} that is overestimated by the model.

2.5 Summary and conclusions

This chapter presents results from a 1-D canopy-chemistry model, CACHE, applied to a northern Michigan mixed hardwood forest to elucidate in-canopy atmospheric chemistry during the CABINEX 2009 field campaign. CACHE calculates vertical mixing within and above the forest canopy using K-theory, a parameterization used by many 1-D and 3-D models, despite its limitations in the canopy roughness layer. Chemical transformation is modeled using RACM, a condensed mechanism that can cover a broad range of chemical situations but with limited BVOC chemistry particularly under low-NO_x conditions. In this study, we test the model sensitivity of vertical gradients of BVOC and their oxidation products to (1) turbulent exchange and (2) chemistry. First, we account for turbulence in the canopy roughness layer by

applying the modified K-theory parameterization of *Makar et al.* (1999) and adjusting the model with high-time-resolution sonic anemometer measurements of friction velocity and vertical velocity standard deviation. Second, we implement an expanded version of RACM with more explicit BVOC chemistry, RACM-MIM.

Traditional K-theory (i.e., BASE) underestimates forest canopy exchange by 0.5–2 orders of magnitude, leading to an overly-strong diurnal cycle of ozone, and an overestimate of NO_x, BVOC and their oxidation products that accumulate within and above the canopy to 2–3 times higher than observed. This highlights the issue that models with differing turbulence parameterizations in and above the canopy may inhibit exchange across the top of the canopy due to a discontinuity in mixing between the two equations. In addition, traditional K-theory, in which turbulence is driven by a prognostic temperature profile, does not capture the observed gradual onset and termination of convective mixing due to uncertainties with the empirical stability parameter at the transition between stable and unstable conditions. This leads to anomalous spikes in primary BVOC near the canopy, particularly around sunset, that are not present in the observations. Driving near-canopy vertical mixing with micrometeorological observations (e.g., MIX) improves the representation of vertical mixing as evidenced in the improved vertical profiles and diurnal cycles of BVOC and their oxidation products. While this parameterization cannot account for asymmetric transport associated with coherent structures and other non-gradient processes, this method provides substantial improvement in the model simulations. We note, however, that this method requires input from sonic anemometer and thus is only applicable when and where such data is available. Adding new BVOC oxidation pathways with the RACM-MIM mechanism slightly increases isoprene and HCHO (15 %) with greater changes in MACR+MVK (80 %), although these concentrations were about five times higher than observed at all heights. Past research suggests that MACR+MVK may constitute only a fraction of the MACR RACM surrogate,

and that models may underestimate MACR+MVK surface deposition; however, deposition velocity for MACR+MVK in the model compares well with observations. Changes in O_3 and NO_x concentrations with enhanced isoprene chemistry were negligible. Overall, the parameterizations tested in this study suggest BVOC and their oxidation products can be very sensitive to the mixing parameterization.

The impact of vertical mixing on HO_x chemistry is dependent on the advection conditions. Advection from polluted regions (e.g., the first day of our simulation) increases OH in the region of advection (45–106 m) and decreases OH below the level of advection. When local chemistry dominates, an increase in mixing increases OH concentrations suggesting that the canopy can be a HO_x source. For HO_2, an increase in mixing tends to decrease concentrations regardless of advection conditions. With changes to the RACM-MIM chemistry, OH decreases due to increased secondary oxidation of biogenic oxidation products and HO_2 decreases throughout the profile. While the additional BVOC oxidation pathways of RACM-MIM improve HO_2, the overestimation of MACR+MVK suggests that the mechanism pathway may not be properly capturing the oxidation of the biogenic oxidation products. Additionally, we find that glyoxal is underestimated in the model by an order of magnitude (Fig. 2.11), suggesting a missing primary biogenic oxidation source.

Typically, 1-D models are subject to several aspects of uncertainty, including (1) the emissions from the canopy and soil, (2) the reactions described by the chemical mechanism, (3) the exchange driven by the turbulence parameterization, and (4) the sink to surface deposition. We have evaluated each of these aspects in this chapter, while focusing our sensitivity study on mixing and chemistry. The BVOC emissions have been fairly well-constrained by multiple measurements at the site; however, we find that observed emission factors for isoprene are likely on the lower end of the spectrum due to the unusually cool summer at UMBS. If emission rates were higher than modeled in this study, BVOC concentrations accumulate in the model to un-

realistic concentrations. In theory, this could be matched by higher reactivity in the forest, with increased oxidation by OH through the implementation of an OH recycling mechanism (*Lelieveld et al.*, 2008) or enhanced deposition of compounds competing for OH (e.g., oxygenated VOC, *Karl et al.*, 2004, 2010). With enhanced oxygenated VOC deposition according to *Karl et al.* (2010) applied in this study, BVOC still accumulate. OH concentrations were well-matched with the observations; therefore, we did not implement a recycling mechanism in this study. Additionally, underestimations in peroxide (e.g. H_2O_2) deposition may inhibit in-canopy photochemistry and exchange (*Ganzeveld et al.*, 2006); however, peroxide measurements were not available to constrain deposition rates. We tested the sensitivity of the model to higher NO_x, potentially from a local or advective source by increasing NO_2 advection rates until the NO_x concentrations match urban levels (not shown). With higher isoprene emissions (e.g., the mean value of *Ortega et al.*, 2007), higher NO_x can increase the oxidation and reduce BVOC concentrations to observed values, however modeled NO_x concentrations then exceed observed values by an order of magnitude. It is also possible that OH concentrations are too low in the model (e.g., Fig. 2.14, left panel); however, our modeled BVOC oxidation products are already higher than observed and we have good measured-modeled agreement in OH reactivity. Therefore, we have evidence to show that the modeled emissions and chemistry balance in the model represents the observed conditions fairly accurately.

Overall, we find that an improved representation of in-canopy turbulent transport based on micrometeorological observations and a consideration for near-field effects improves the simulation of concentrations and vertical gradients of BVOC and their oxidation products observed during the CABINEX 2009 campaign. The change to a mechanism with more specific BVOC pathways slightly improves agreement with observations for HO_2, but produces more BVOC oxidation products than observed (e.g., HCHO, MACR+MVK). While the yields of BVOC oxidation products in MIM

may be too high (e.g., *Geiger et al.*, 2003) or surface deposition rates may be too low (*Pugh et al.*, 2010), observed concentrations of these primary oxidation products suggest that our in-canopy oxidation is within the observational constraints. However, we note that implementation of other isoprene oxidation mechanisms (e.g., MCM, CACM) may yield different results. Our results show that mixing in the canopy may be more important than changes to BVOC chemistry mechanisms for accurate modeling of BVOC chemistry and forest-atmosphere exchange, and point to the need for a revised in-canopy turbulence parameterization in existing 1-D and 3D atmospheric models. A thorough intercomparison of turbulence and BVOC chemistry data from a variety of forest ecosystems is required to assess the applicability of our results on the global scale. Other aspects of the forest canopy, including the turbulence structure of the lower canopy and the effect of vertical heterogeneity of vegetation (i.e., an understory and overstory of differing plant type) on the oxidation capacity of the canopy and forest-atmosphere exchange of BVOC may provide further information for understanding the vertical profiles of BVOC, their oxidation products, and their contribution to tropospheric chemistry.

2.6 Acknowledgements

Funding for this work was provided by the National Science Foundation AGS-0904128 to M.A. Carroll and A.L. Steiner at the University of Michigan (UM). Additional support for A.M. Bryan was provided through the University of Michigan Elizabeth C. Crosby Research Foundation and the Michigan Space Grant Consortium. We thank C. Vogel at UMBS for providing ancillary meteorological data for our analysis, as well as Meghan Thurlow, Melissa Galloway, and Anthony O'Brien for providing the glyoxal measurements. We thank José Fuentes, Laurens Ganzeveld, and an anonymous reviewer for comments that greatly improved this chapter.

CHAPTER III

Forest-atmosphere BVOC exchange in diverse and structurally complex canopies: 1-D modeling of a successional forest in northern Michigan

3.1 Abstract

Foliar emissions of biogenic volatile organic compounds (BVOC)—important precursors of tropospheric ozone and secondary organic aerosols—vary widely by vegetation type, yet modeling studies thus far demonstrate limited capability in capturing the complexities in canopy structure and composition observed in mixed forests. To assess the sensitivity of biogenic chemistry to canopy structure and composition, we compare two 1-D canopy model simulations in which BVOC emission potentials are (1) uniform or (2) vary with canopy depth. Simulations are evaluated against multi-height observations from a successional, mixed hardwood forest at the University of Michigan Biological Station (UMBS). The heterogeneous simulation places the high isoprene-emitting foliage (e.g., aspen and oak) in the upper canopy as observed at UMBS, where higher sunlight availability increases the light-dependent isoprene emission by up to 72 %. The increased emission enhances mean canopy isoprene concentrations by 35 %, and improves agreement with observations for isoprene and formaldehyde. When accounting for canopy heterogeneity, the successional removal

of high-isoprene-emitting aspen reduces isoprene emissions by a factor of two as compared to a homogenous canopy. Overall, these results highlight the importance of adequately representing complexities in canopy structure for simulating biogenic VOC emissions and in-canopy chemistry.

3.2 Introduction

Forest ecosystems affect tropospheric chemistry and climate through the release of volatile organic compounds (VOC). VOC are key ingredients for ground-level ozone (O_3) and secondary organic aerosol (SOA) formation (*Logan*, 1985; *Claeys et al.*, 2004). Biogenic VOC (BVOC) sources dominate the global VOC budget (*Guenther et al.*, 1993), yet their contributions to global O_3 and SOA levels are not well known due to our limited understanding of biogenic chemistry in rural environments (*Di Carlo et al.*, 2004; *Lelieveld et al.*, 2008; *Ganzeveld et al.*, 2008; *Carlton et al.*, 2009; *Bryan and Steiner*, 2013). One aspect of forest ecosystems that is still uncertain with respect to its role in biogenic chemistry is the composition and architecture of canopy vegetation. Global- and regional-scale models are unable to resolve the complexities of ecosystems, resulting in highly parameterized sources, sinks, and transport of biogenic VOC. Local-scale, one-dimensional canopy-chemistry models (e.g., CACHE, SOSA, CAFÉ) with highly resolved canopy layers have been developed and utilized to examine the sensitivity of forest-atmosphere exchange to complex, sub-grid scale processes (*Forkel et al.*, 2006; *Boy et al.*, 2011; *Wolfe and Thornton*, 2011). Despite having many layers within the canopy, many 1-D models (e.g., CACHE, SOSA) assume uniform vegetation for all canopy layers. Many ecosystems, however, comprise of a complex mixture of vegetation species with different stand heights. In CAFÉ, *Wolfe and Thornton* (2011); *Wolfe et al.* (2011) separate the canopy into understory and overstory layers with distinct foliage attributes (area, mass, BVOC emission potential); however, the effect of splitting the canopy is not addressed by the authors nor

evident by their results, so the importance of distinguishing overstory and understory foliage is uncertain.

Vegetation heterogeneity has implications for BVOC chemistry given the variability in composition and abundance of chemical emissions across vegetation species. Isoprene (C_5H_8) generally derives from broadleaf vegetation whereas monoterpenes ($C_{10}H_{16}$) derive mostly from needle-leaf vegetation (*Steiner and Goldstein*, 2007). Isoprene is emitted in large quantities, making it globally abundant and one of the primary precursors of troposphere ozone. Monoterpene emissions are smaller in magnitude than isoprene, and are thought to be more important in the role of the formation of secondary organic aerosols (*Kroll and Seinfeld*, 2008). Such differences in the fate of the dominant BVOC types suggest that mixed forests have complex in-canopy chemistry that homogeneous canopy models may miss.

In this study, we assess the impact of canopy heterogeneity on BVOC chemistry at the University of Michigan Biological Station (UMBS) using the Canopy Atmospheric Chemistry Emissions (CACHE, *Forkel et al.*, 2006; *Bryan et al.*, 2012) model. Located remotely within a successional forest in the northern lower peninsula of Michigan, the UMBS forest comprises of a distinct lower canopy of monoterpene-emitting pine, maple, and beech beneath an upper canopy of high-isoprene-emitting aspen and oak. The research facility, known as the Program for Research on Oxidants: Photochemistry, Emissions, and Transport (PROPHET, *Carroll et al.*, 2001), has been the site of numerous field studies over the past 17 years (*Tan et al.*, 2001; *Di Carlo et al.*, 2004; *Bryan et al.*, 2012), including the Community Atmosphere-Biosphere Interactions Experiment (CABINEX) in 2009. Data from CABINEX 2009 offer an ideal opportunity to examine the role of canopy heterogeneity on biosphere-atmosphere interactions given the expansive array of multi-height measurements obtained. The timeline of this study also coincides with start of the Forest Accelerated Succession Experiment (FASET), in which the successional removal of high isoprene-emitting

aspen is expedited. As part of this study, aspen species within a 500-m-radius plot surrounding a flux tower were girdled to disrupt the flow of nutrients up the plant stem in 2008. By spring 2012, over 90% of the aspen within the plot had died.

To assess the effect of canopy heterogeneity on biogenic VOC and their atmospheric fate, we compare two simulations: a homogeneous canopy represented by a vertically uniform ecosystem-mean BVOC emission potential, and a heterogeneous canopy where BVOC emission potentials vary according to the mean stand heights of individual vegetation species. Section 3.3 describes the region of study, measurements obtained, model specifications, and simulation details. Section 3.4 examines the impact of heterogeneity on BVOC projections of post-successional conditions that excludes aspen. A summary and concluding remarks are given in Section 3.5.

3.3 Methods

3.3.1 Site description and CABINEX 2009 measurements

UMBS is located at the temperate-boreal transition zone at the northern tip of Michigan's lower peninsula (*Schmid et al.*, 2003). Its ecosystem contains a diverse array of broad- and needle-leaf vegetation, including a mature 23-m high upper canopy of bigtooth aspen (*Populus grandidentata*), quaking aspen (*Populus tremuloides*), and paper birch (*Betula papyrifera*), and a young lower canopy of Eastern white pine (*Pinus strobus*), red maple (*Acer rubrum*), and American Beech (*Fagus grandifolia*). Red oak (*Quercus rubra*) is present in both the upper and lower canopy due to coexistence of mature trees and young saplings (*Schmid et al.*, 2003; *Pressley et al.*, 2005). As such, BVOC emissions from the upper canopy are predominantly isoprene with monoterpene emissions dominating the lower canopy.

An extensive set of meteorological and gas-phase chemistry measurements were taken at multiple heights during the 1 July – 8 August 2009 observational period

as part of the CABINEX 2009 summer intensive. Simulated concentrations of primary BVOC (isoprene and monoterpenes) and first-generation oxidation products (formaldehyde, methacrolein, and methyl vinyl ketone) are evaluated using above- (34 m), upper- (20 4 m) and lower- canopy (6 m) observations from PTR-MS. Total (direct and diffuse) shortwave (visible and near-infrared) solar radiation measured at three levels (32.6 m, 20.4 m, and 2 m) is used to constrain the model radiation as described in Section 3.3.2. For instrumentation details and information about other measurements obtained during CABINEX 2009, see *Kim et al.* (2011), *Zhang et al.* (2012), *Bryan et al.* (2012), and *Griffith et al.* (2013).

3.3.2 Model description

CACHE is a one-dimensional vertical column model with a high-resolution canopy designed to simulate in- and above-canopy concentrations and vertical fluxes of heat and trace gases. CACHE simulates four main processes (*Bryan and Steiner*, 2013): (1) emissions of BVOC from foliage and nitrogen oxide (NO) from soil, (2) atmospheric chemistry, (3) turbulent exchange, and (4) deposition onto leaf and soil surfaces. *Bryan et al.* (2012) detail the treatment of these processes in CACHE and application to the UMBS site and the CABINEX 2009 campaign with the exception of a few modifications to enhance model performance at the site, described below.

Vertical transport and deposition processes follow the same procedure as outlined by *Bryan et al.* (2012). Vertical transport is modeled using the first-order closure flux-gradient relationship known as K-theory (*Blackadar*, 1979). Above-canopy turbulence is a function of the Richardson number, in which mechanical shear derives from the logarithmic wind equation and buoyancy derives from an empirical stability function (*Forkel et al.*, 1990). In-canopy turbulence is estimated by the model at each time step following *Baldocchi* (1988) and then adjusted following *Bryan et al.* (2012) based on the observed friction velocity and vertical velocity standard deviation to ac-

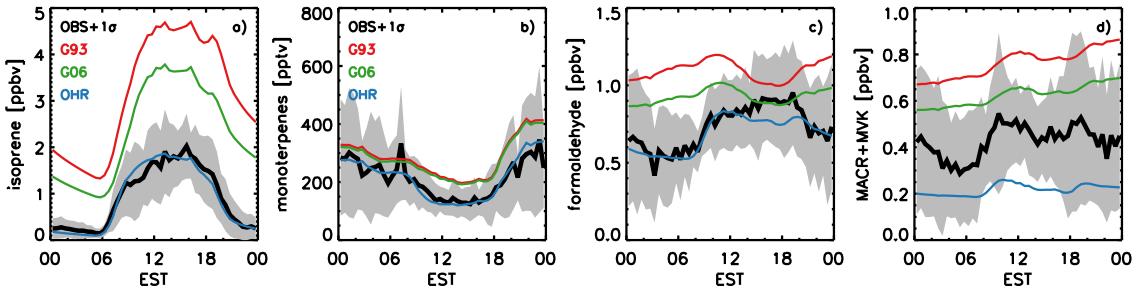

Figure 3.1: Observed (black, plus one standard deviation shaded) and simulated 20.4-m campaign-average (1 July–8 August, 2009) diel cycles of (a) ISO, (b) MT, (c) HCHO, and (d) MACR+MVK. Three simulations are shown: one applying the *Guenther et al.* (1993) BVOC emissions parameterization and no OH recycling (G93, red), another applying the MEGAN parameterization of *Guenther et al.* (2006) and no OH recycling (G06, green), and a third also applying MEGAN algorithm, as in G06, but with OH recycling applied (OHR, blue).

count for deficiencies in the turbulence parameterization. Dry deposition is modeled according to *Wesely* (1989) and *Gao et al.* (1993). The Henry's Law constants for the secondary organics (formaldehyde and the sum of methacrolein and methyl vinyl ketone, hereafter HCHO and MACR+MVK) was increased based on the findings of *Karl et al.* (2010). NO emissions from soil uses an emission factor observed at UMBS by *Alaghmand et al.* (2011).

For foliar emissions of BVOC, *Bryan et al.* (2012) used the parameterization following *Guenther et al.* (1993, hereafter G93), where emission potentials utilized observations from *Ortega et al.* (2007) and the CABINEX 2009 campaign. To account for the cool and cloudy conditions during the summer 2009 at UMBS, the authors lowered the emission potentials to one standard deviation below the observed mean. For the current application of CACHE, we implement the parameterization for BVOC emissions of the Model of Emissions of Gases and Aerosols from Nature (MEGAN, *Guenther et al.*, 2006, hereafter G06). As an extension of the G93 algorithm, the MEGAN parameterization incorporates 24- and 240-hour historical photosynthetically active radiation (PAR_{24} and PAR_{240}) and temperature (T_{24} and T_{240}) to ac-

count for the effect of prior meteorological conditions on emissions ($\frac{\partial c}{\partial t}_{\text{emission}}$, where c is concentration):

$$\frac{\partial c}{\partial t}_{\text{emission}} = \epsilon\gamma \tag{3.1}$$

where ϵ is an emission factor (or potential) and γ is an activity factor that scales the emissions based on light and temperature according to the following:

$$\gamma_P = C_{\text{PAR}}[(\alpha \cdot \text{PAR})/((1 + \alpha^2 \cdot \text{PAR}^2)^{0.5})] \tag{3.2}$$

$$\gamma_T = E_{\text{opt}} \cdot \frac{C_{T2} \cdot \exp(C_{T1} \cdot x)}{C_{T2} - C_{T1} \cdot (1 - \exp(C_{T1} \cdot x))} \tag{3.3}$$

where

$$C_{\text{PAR}} = 0.0468 \cdot \exp(0.0005 \cdot [\text{PAR}_{24} - \text{PAR}_0]) \cdot [\text{PAR}_{240}]^{0.6} \tag{3.4}$$

$$\alpha = 0.004 - 0.005 \ln(\text{PAR}_{240}) \tag{3.5}$$

$$E_{\text{opt}} = 2.034 \cdot \exp(0.05 \cdot (T_{24} - 297)) \cdot \exp(0.05 \cdot (T_{240} - 297)) \tag{3.6}$$

$$x = [(1/T_{\text{opt}}) - (1/T)]/0.00831 \tag{3.7}$$

$$T_{\text{opt}} = 313 + (0.6 \cdot (T_{240} - 297) \tag{3.8}$$

and C_{T1} and C_{T2} are 95 and 230, respectively, and P_0 is 200 and 50 $\mu\text{mol}\,\text{m}^{-2}\,\text{s}^{-1}$ for sunlit and shaded leaves, respectively. For 24- and 240-hour historical PAR and T, we use the campaign-average values ($\text{PAR} = 498\,\mu\text{mol}\,\text{m}^{-2}\,\text{s}^{-1}$, $T = 17\,^{\circ}\text{C}$). At these values for historical PAR and T, G06 yield 32% and 5% less isoprene and monoterpene concentrations, respectively, than the G93 algorithm, resulting in a 20% and 32% decrease in formaldehyde and MACR+MVK, respectively (Figure 3.1). While this decrease improves the magnitude of HCHO and MACR+MVK, neither simulation captures the observed amplitude of diel cycle, in particular the morning minimum, due to missing daytime production (not shown). For simplicity, we assume isoprene emission is a function of light and temperature, and monoterpene emissions depend

on temperature alone. Monoterpenes emissions exhibit a temperature dependence different from that of isoprene according to *Guenther et al.* (1993):

$$\gamma_T = \exp\left(\beta(T_{\text{leaf}} - 303)\right) \tag{3.9}$$

where β is a species-specific scaling factor. In most applications, β is given by a multi-species average value of 0.09 (*Guenther et al.*, 1993). Here, we prescribe a β value of 0.11 corresponding to the value given for *P. strobus*, the dominant monoterpene emitter at UMBS (*Guenther et al.*, 1993). This value is similar to that derived in the field by *Ortega et al.* (2007, 0.12). With the MEGAN parameterization, we no longer need to subtract one standard deviation as in *Bryan et al.* (2012). However, given the wide range in observed emission potentials reported in the literature and known uncertainty in the emission potentials (*Niinemets et al.*, 2010), we use the mean genus-level isoprene and monoterpene emission potential for all tree species provided by *Guenther et al.* (1994), as is typical for modeling applications. Monoterpene composition by vegetation type derives from the comprehensive tabulation provided by *Geron et al.* (2000).

As in *Bryan et al.* (2012), gas-phase chemistry is driven by the Regional Atmospheric Chemistry Mechanism *Stockwell et al.* (RACM, 1997). Three of the 77 RACM species represent the primary biogenic emissions (isoprene, α-pinene, and *d*-limonene). ISO denotes isoprene. Monoterpenes are lumped into cyclic terpenes containing one double bond, like α-pinene (denoted API), and cyclic dienes, such as *d*-limonene (LIM). API includes α- and β-pinene, camphene, sabinene, 1,8-Cineole, Δ^3-Carene, and p-Cymene; LIM includes *d*-Limonene, β-myrcene, β-Phellandrene, α- and β-camphor, and γ-terpinene (*Stockwell et al.*, 1997; *Tan et al.*, 2001). Many studies find that current chemical mechanisms simulate insufficient BVOC oxidation in low-NO_x environments (*Tan et al.*, 2001; *Di Carlo et al.*, 2004; *Pugh et al.*, 2010). To account

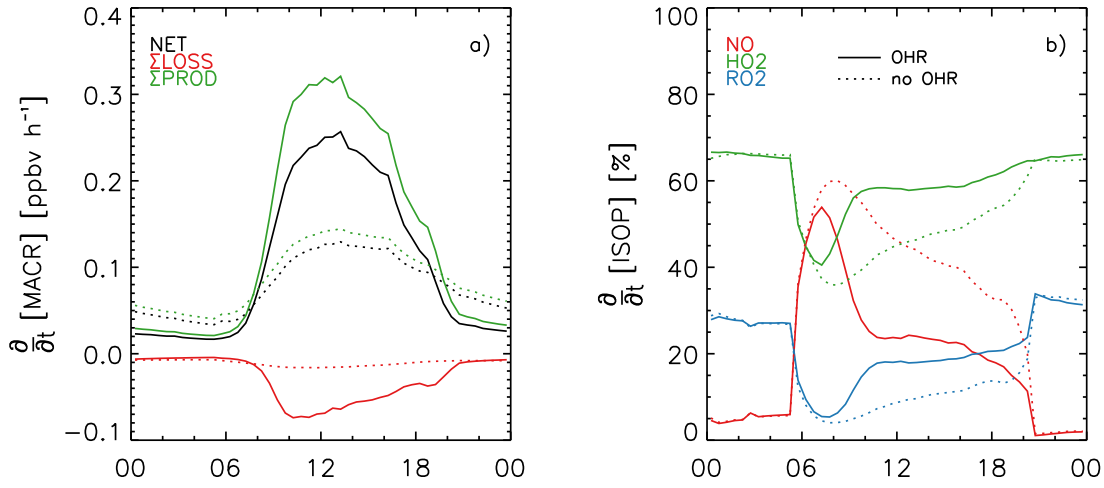

Figure 3.2: (a) Rate of change of methacrolein (MACR+MVK) with respect to production (green), loss (red), and net change (black); (b) loss rate of change (%) of isoprene peroxy radicals (ISOP) with respect to NO (red), HO2 (green), and RO2 (blue, ISOP + MO2 + ACO3). In both panels, solid and dotted lines represent with and without OH recycling, respectively.

for this, *Lelieveld et al.* (2008) proposed that OH recycles during isoprene oxidation. *Pugh et al.* (2010) found that the ISOP + HO_2 reaction yielding 2–4 OH provided the best model-measurement agreement. We apply the methodology of *Pugh et al.* (2010) and find that a mid-range OH yield of 3 from the ISOP + HO2 reaction allows sufficient BVOC oxidation relative to CABINEX 2009 measurements, as indicated by adequate isoprene destruction by the end of the day (Figure 3.1). OH recycling also improves HCHO by lowering concentrations and enhancing the amplitude to the diel cycle. For MACR+MVK, however, concentrations fall below observations with OH recycling. Other studies confirm that RACM tends to underestimate MACR+MVK in low-NO_x environments (*Geiger et al.*, 2003). *Bryan et al.* (2012) find that updating RACM with the Mainz Isoprene Mechanism (MIM) following *Geiger et al.* (2003) improves the MACR+MVK diel cycle by increasing the amplitude; however, the updated mechanism vastly overestimates observed MACR+MVK concentrations,

hence we continue to use the original RACM in this study. To explain the decrease in MACR+MVK with OH recycling in RACM, we examine the isoprene oxidation chemistry more closely. The enhanced isoprene oxidation increases the primary ingredient for MACR+MVK: isoprene peroxy radicals (ISOP). While OH recycling strengthens the MACR+MVK sink to OH, the enhanced production from the increased ISOP exceeds the increased loss to OH (Figure 3.2a), thus the enhanced sink does not fully explain the decreased MACR+MVK concentrations. The MACR+MVK decrease results from a switch in dominant loss pathway for ISOP from NO_x-dominated to HO_x-dominated induced by the enhanced OH concentrations (Figure 3.2b). MACR+MVK forms predominantly from ISOP + NO, followed by ISOP + RO2 (RO2 = ISOP + MO2 + ACO3). In RACM, MACR+MVK is not formed under the ISOP+HO2 reaction. Therefore, as the ISOP+HO2 pathway becomes increasingly dominant, the net MACR+MVK yield decreases. OH recycling dampens the ISOP+NO reaction and strengthens the ISOP+HO2 reaction, resulting in less ISOP going toward MACR formation.

3.3.3 Experiment design

We simulate gas-phase chemistry, turbulent transport, BVOC and soil NO emissions, and dry deposition at UMBS for one 24-hour period representing campaign-average (1 Jul–8 Aug) conditions during CABINEX 2009. The temperature profile is initialized based on the campaign-average mean temperature of 290 K. The initial vertical temperature profile follows the standard moist adiabatic lapse rate ($\gamma = 6.5\,^{\circ}\mathrm{C\,km^{-1}}$). Total solar radiation measured above the canopy is provided as input to drive photochemistry, isoprene emissions, and the prognostic temperature profile via surface heating and subsequent buoyant turbulence. Near-canopy turbulence is modified following *Bryan et al.* (2012) using observed friction velocity and vertical velocity standard deviation measured by a sonic anemometer at two heights

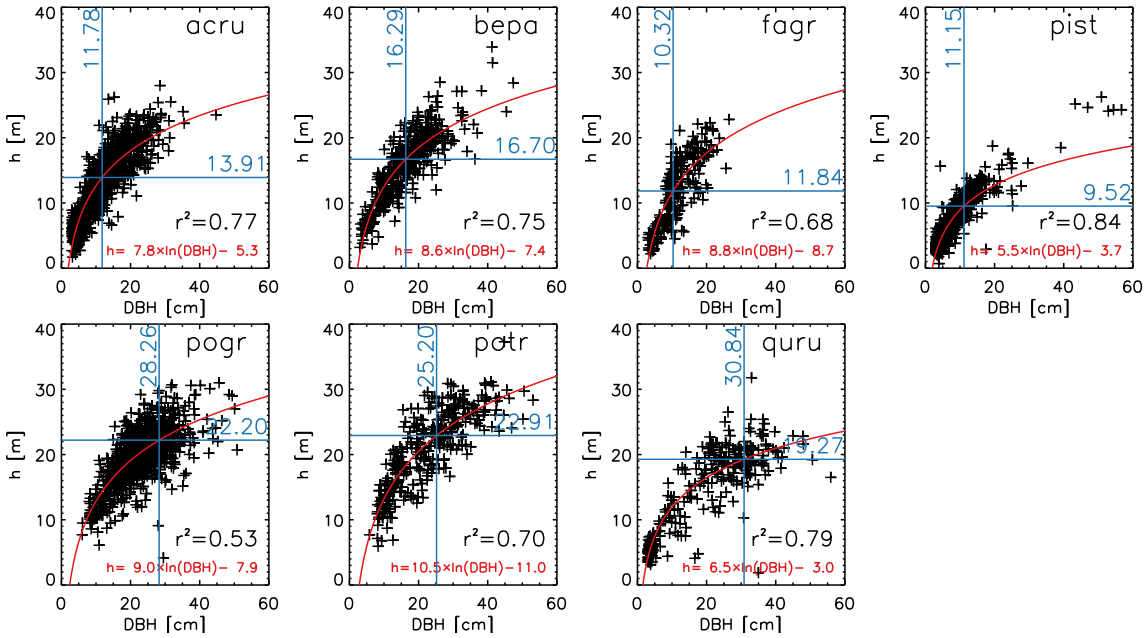

Figure 3.3: Observed tree height with respect to DBH by species. Regressions (red) were obtained following *Garrity et al.* (2012). Current mean DBH (vertical lines) were applied to the regressions to obtain the current mean tree height (horizontal lines).

within the canopy.

To construct the heterogeneous forest canopy, we used multiple measurements from a 60-m-radius census plot surrounding the UMBS FLUXNET tower (400 m northeast of PROPHET). Tree height and diameter at breast height (DBH) measurements for over 6000 trees within a 1-km radius circle surrounding the tower were collected in 1997 and used to develop allometric relationships between the two quantities following *Garrity et al.* (2012) (Figure 3.3). These relationships were used with July 2012 DBH measurements for 271 trees in the 60-m plot (1 *P. tremuloides*, 44 *F. grandifolia*, and 45 of the remaining five species mentioned above, excluding 22 oak saplings) to estimate the height of the crown top for each vegetation type. The crown base height (i.e., distance from the ground to the first branch containing foliage) for the same 271 trees was measured using a clinometer for large trees and a standard tape measure for shorter trees. The leaf area density (LAD) between the crown base

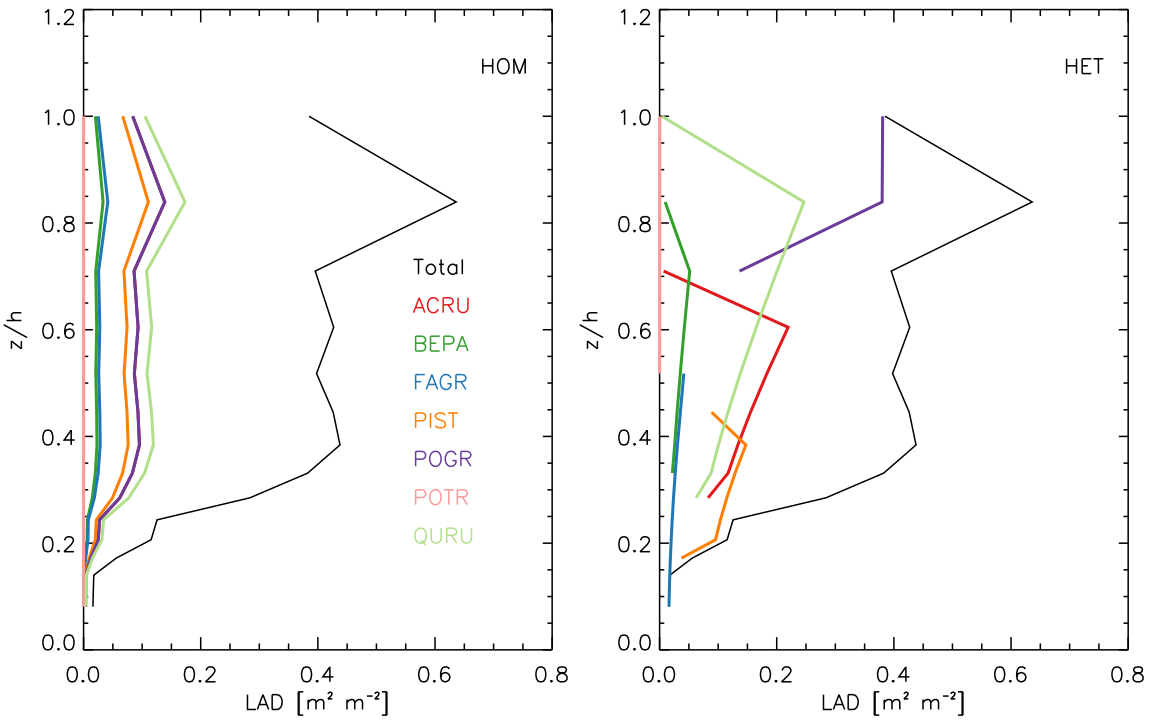

Figure 3.4: Vertical profiles of leaf area density (LAD) by species for the HOM (left) and HET (right) simulations. Height is normalized by the height of the canopy ($h = 22.9$ m) where $z/h = 1$ represents the canopy top.

and top was derived from the specific leaf mass, estimated from mean leaf area and dry weight measured from 2011 litter traps. Sensitivity tests with varying LAD distributions reveal that BVOC emissions are relatively insensitive to crown shape (not shown). Therefore, we assume a constant LAD with height throughout the crown (i.e., the total column leaf mass is evenly distributed between the crown base and top) for simplicity, noting that some species may have greater LAD at the crown top while others have more at the crown base.

Using the seven individual LAD profile estimates described above, we simulate two vertical distributions of canopy foliage (Figure 3.4), represented by an adjustment in the BVOC emission potentials (ϵ, μg g^{-1} h^{-1}, in Equation 3.1, Figure 3.5). In the first simulation, hereafter the homogeneous (HOM, Figure 3.4, left) simulation, we assume

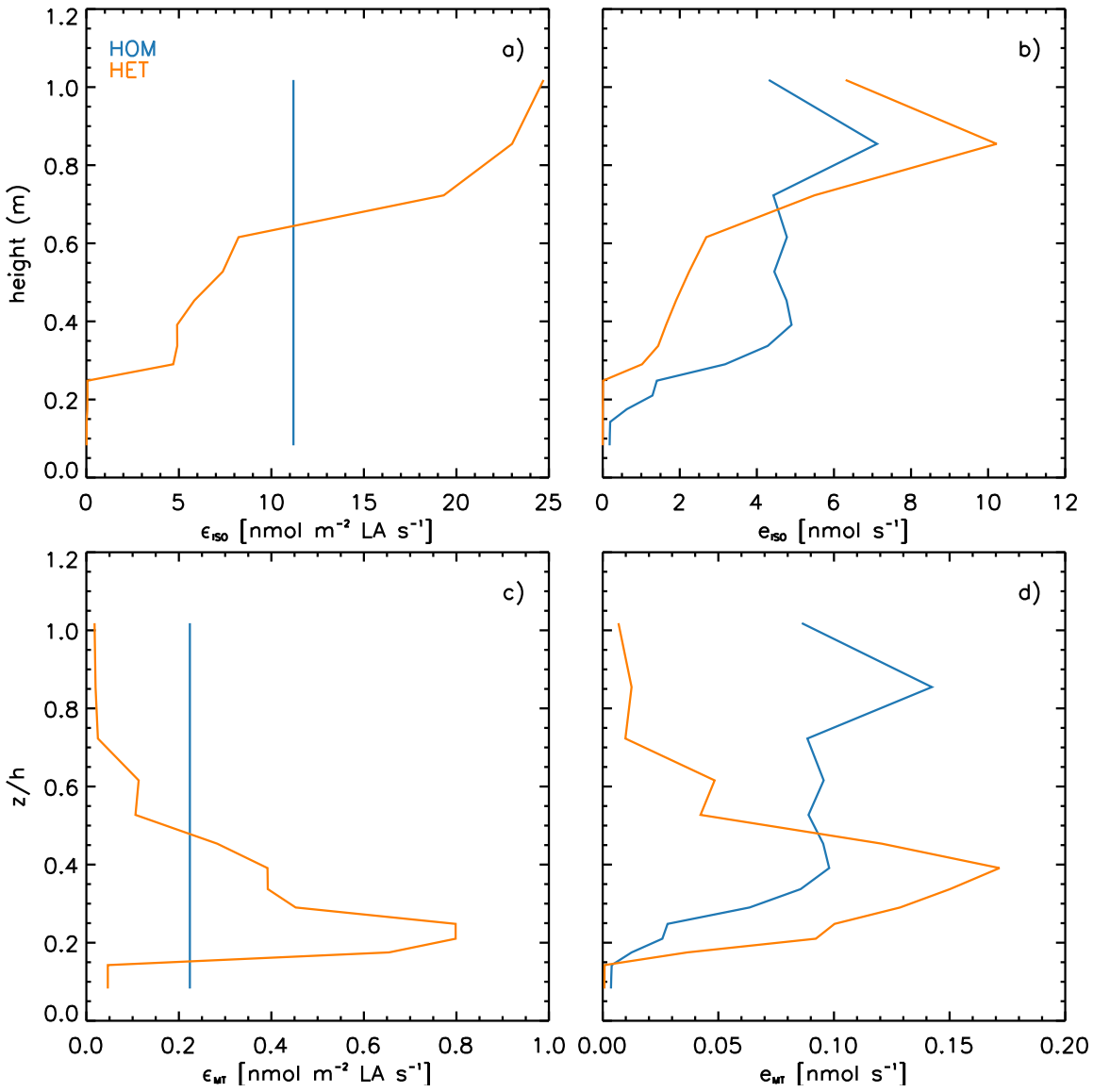

Figure 3.5: Vertical profile of emission factors at standard conditions (left) and scaled by LAD (right) for isoprene (top) and monoterpenes (bottom), as simulated by the homogeneous (HOM, blue) and heterogeneous (HET, orange) canopy structure model scenarios.

all vegetation species have the same crown base and top heights, selected as ecosystem-level means of 1.22 and 22.91 m, respectively. The leaf area index (LAI), as measured by litter trap, is spread out between the mean crown base and top and prescribed with the same ecosystem-level mean LAD profile for each species, as depicted in the left panel of Figure 3.4. This is represented in the model by presuming constant BVOC emission potentials (ϵ,) throughout the full canopy depth, as is traditionally done in 1-D models (Figure 3.5a, c, blue line). The effect on emission rates (at standard conditions, i.e. ϵ scaled by the LAD profile) is shown in Figure 3.5b, d. Previous implementations of CACHE and similar 1-D models apply this simplified approach for BVOC emissions, which is similar to that of a 0-D big-leaf model and thus does not take full advantage of the increased resolution in the canopy.

In the second simulation, referred hereafter as the heterogeneous (HET) simulation, the foliage for a given vegetation species is distributed within the measured trunk and tree heights for respective species (Figure 3.4, right). For instance, *Q. rubra* has a total column LAI of 0.898 $m^2\,m^{-2}$, which we evenly distributed between the species mean trunk height of 5.77 m and stand height of 13.91 m. To represent this effect in the modeled BVOC emissions, the BVOC emission factors of *Q. rubra* are only included at the model vertical grid points between 5.77 and 13.91 m and are scaled at each grid point by the LAI per number of model levels between 5.77 and 13.91 m. The end result is a more realistic representation of canopy emissions in which the composition of emissions along the canopy depth depends on where foliage of each tree species exists within the canopy (Figure 3.5a, c, orange line). While this approach increases the precision of the vegetation description, we note that the species-specific measurements used here are not currently available at other forest sites, or even in other plots at the UMBS site. However, it is feasible to estimate species-level mean crown heights and depths at other sites or larger regions using gridded datasets of vegetation density and age. Such datasets would be ideal for

similar investigations using 3-D regional models.

3.4 Results

We first show how observations vary vertically (Section 3.4.1) and compare the HOM and HET simulations to assess the impact of canopy heterogeneity on BVOC emissions (Section 3.4.2). Finally, we simulate UMBS following succession by omitting aspen and compare the feedbacks predicted by the HOM and HET cases (Section 3.4.3).

3.4.1 Observations

Figure 3.6 shows observed campaign-average diel cycles of the primary BVOC (ISO and MT = API + LIM) and their dominant oxidation products (HCHO and MACR+MVK) at the upper (20.4 m) and lower (6 m) canopy. Due to the cool and cloudy conditions in 2009, isoprene concentrations peak at about 2 ppbv with a standard deviation of 1 ppbv (Figure 3.6a). Lower and upper canopy isoprene concentrations are within 1% despite the dominance of isoprene-emitting foliage in the upper canopy, suggesting fairly well mixed conditions within the canopy. Many previous studies suggest that the turbulent transport and chemistry timescales of isoprene are comparable (*Molemaker and Vilà-Guerau de Arellano*, 1998; *Krol et al.*, 2000; *Pugh et al.*, 2010). While this may be true above the canopy, these results suggest mixing is more efficient than chemistry within the canopy. In fact, canopy shading reduces photochemistry (*Stroud et al.*, 2005) and mixing may be much more efficient than we currently simulate (*Bryan et al.*, 2012), both of which support a lower turbulence timescale relative to chemistry.

For monoterpenes, lower-canopy concentrations are 5% higher than the upper canopy during the day and up to 15% higher at night (Figure 3.6b), highlighting the influence of the pine and beech in the lower canopy. Monoterpenes exhibit a nighttime

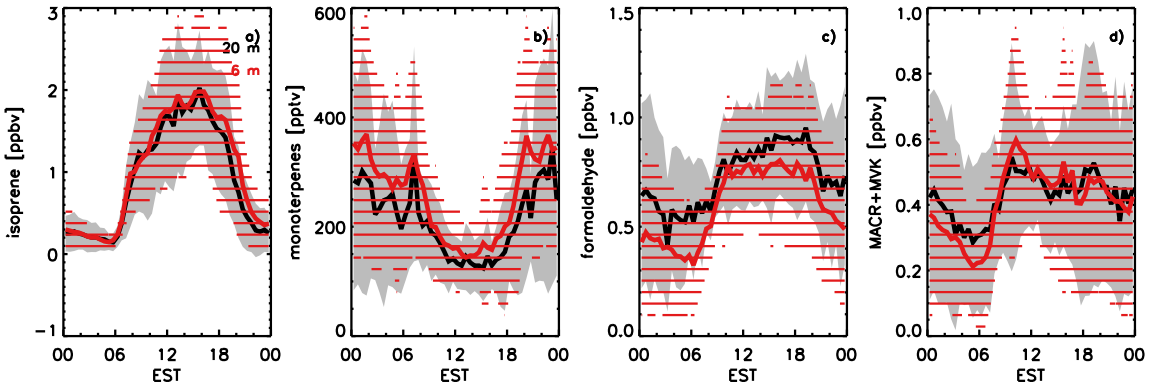

Figure 3.6: Campaign-average (1 July–8 August, 2009) diel cycles of (a) isoprene, (b) monoterpenes, (c) formaldehyde, and (d) the sum of methacrolein and methyl vinyl ketone observed at 20.4 m (black) and 6 m (red). The range of one standard deviation is shaded.

peak of 300–350 pptv, up to 7 times lower than observed at the ponderosa pine plantation in Blodgett Forest Ameriflux site (*Bouvier-Brown et al.*, 2009). Relative to isoprene, monoterpenes are generally more reactive and thus chemistry is more efficient than turbulence. Consequently, monoterpenes are not well mixed within the canopy.

Formaldehyde and MACR+MVK peak during the day at 0.8 and 0.6 ppbv, respectively (Figure 3.6c–d). HCHO is generally higher in the upper canopy than lower canopy, with daytime and nighttime enhancements in the upper canopy of up to 18 and 36%, respectively. This result could indicate increased photochemical production in the upper canopy. In addition, HCHO deposits more effectively than other species, and formation may exceed deposition in the upper canopy. Relative to primary BVOC, HCHO has a longer chemical lifetime, yet conditions do not appear to be well mixed. This suggests that the combined effects of photochemical production and deposition, which are dominant in the upper and lower canopy, respectively, outweigh the effects of turbulent mixing. Similar to HCHO, the upper canopy has higher concentrations for MACR+MVK as well. The lower and upper canopy MACR+MVK are generally equivalent during the day with up to 25% higher concentrations in the

upper canopy between midnight and 7 am.

3.4.2 Model sensitivity to canopy heterogeneity

Figures 3.7 and 3.9a show campaign-average diel cycles of BVOC concentrations and vertical profile of isoprene, respectively, simulated by HOM and HET versus observations in the lower (6 m), upper (20.4 m), and above canopy (34 m). HOM captures the observed isoprene. Adding canopy complexity through HET raises isoprene by 31% (Figures 3.7a, b and 3.9a). The isoprene enhancements in the HET simulation are due to the increased upper canopy emission potential profiles (Figure 3.5a, b) that capture the vertical locations of broad- and needle-leaf foliage observed at UMBS. These results show that isoprene emissions and concentrations are highly sensitive to canopy heterogeneity. In addition, these results suggest the isoprene emission potentials applied in this study from *Guenther et al.* (1994) may be too high, or too much light penetrates the canopy in our model simulations. Relative to the emission factors in HOM, which are constant with height, the HET case has greater isoprene emission potentials in the upper canopy and greater monoterpenes emission potentials in the lower canopy (Figures 3.5). The higher light availability in the upper canopy (Figure 3.8) increases the light-dependent isoprene emission rate in the upper canopy (Figures 3.5b and 3.9b). The uniform emission potentials in the HOM simulation lead to emission rates under standard light and temperature that resemble the LAD profile (Figure 3.4). Unlike isoprene, monoterpenes vary by less than 5% between the HOM and HET simulations (Figures 3.7c, d) despite much lower emission rates in the upper canopy and much higher emission rates in the lower canopy (Figure 3.5d). This is due to the relatively smaller magnitude of emissions, low emission rate variability between emitting species, and the lack of light dependence of these emissions. Both simulations are within 5% of the measured nighttime maximum and daytime minimum.

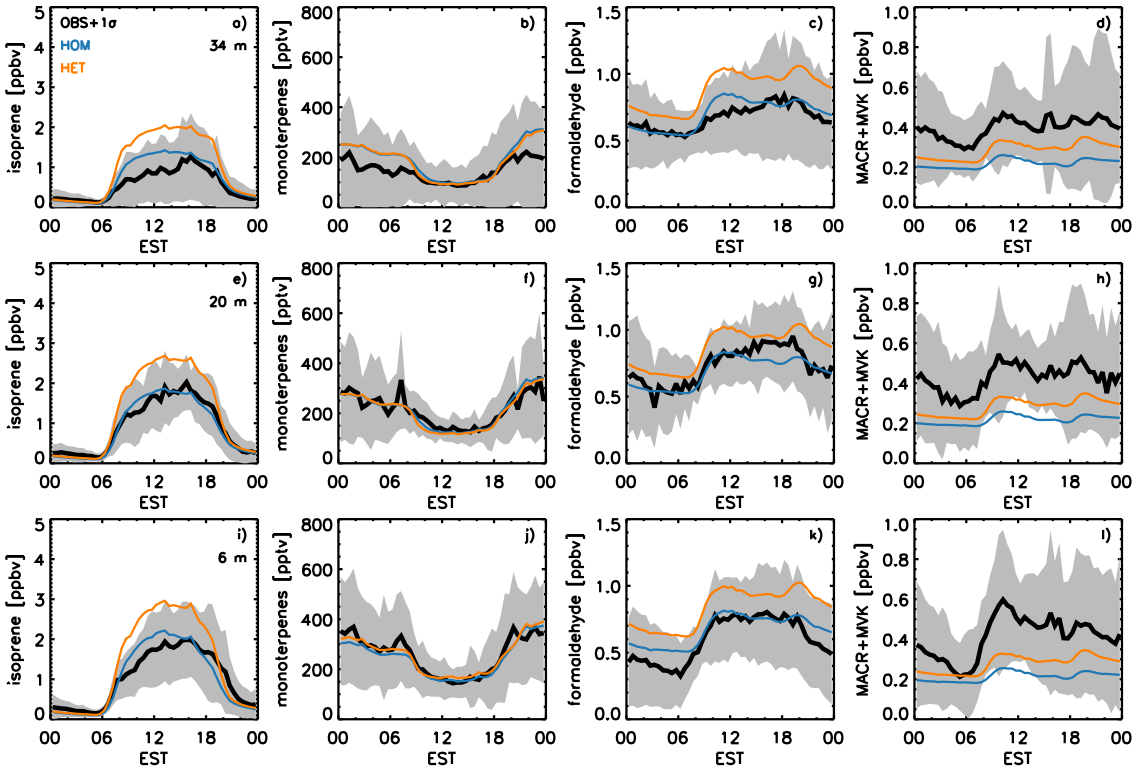

Figure 3.7: Observed (black, one standard deviation shaded) and HOM- (blue) and HET-simulated (orange) campaign-average diel cycles of (a, e, i) isoprene, (b, f, j) monoterpenes, (c, g, k) formaldehyde, and (d, h, l) MACR+MVK above the canopy (34 m, top row) and for the upper (20.4 m, middle row) and lower canopy (6 m, bottom row).

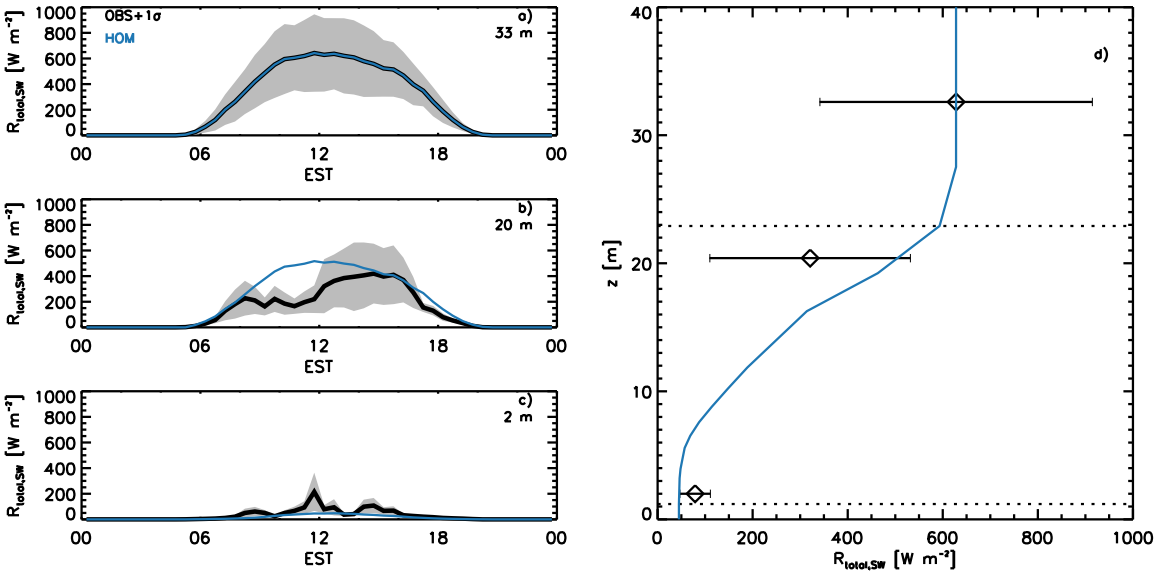

Figure 3.8: (a-c) Campaign-average diel cycle and (d) 12 PM EST vertical profile of observed (black, one standard deviation shaded and whiskers) and HOM simulated (blue) total solar radiation (W m^{-2}. Panels a, b, and c correspond to the 32.6, 20.4, and 2 m measurement heights, respectively.

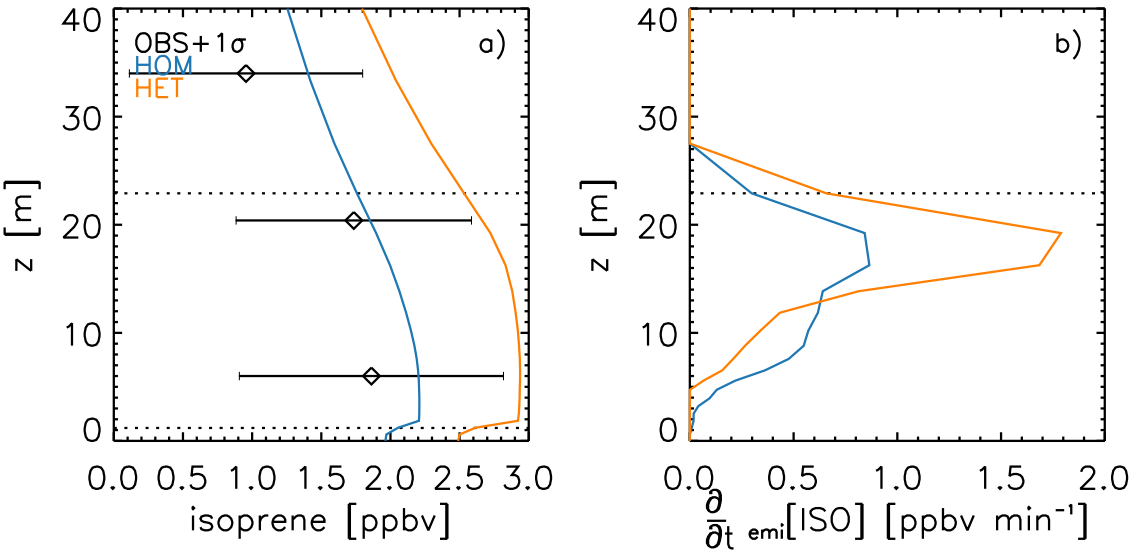

Figure 3.9: Midday (13:00 EST) vertical profiles of campaign-average (a) observed (black diamonds with one standard deviation in whiskers) and simulated (HOM and HET in blue and orange, respectively) isoprene concentration and (b) emission rate.

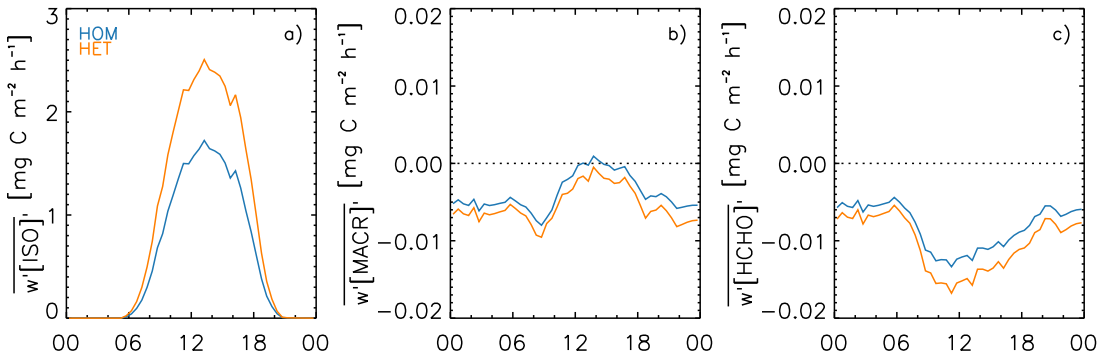

Figure 3.10: Top-of-canopy boundary fluxes for (a) isoprene (ISO), (b) MACR+MVK, and (c) HCHO as simulated by the HOM (blue) and HET (orange) simulations.

The isoprene enhancement raises formaldehyde and MACR+MVK by 21% and 24%, respectively (Figures 3.7e-h). While formaldehyde shows strong agreement with observations, the MACR+MVK increase is insufficient to account for the underestimated concentrations in the HOM simulation. In fact, the MACR+MVK increase is not proportional to the increase in isoprene in the HET case. As discussed in Section 3.3.2, other studies have found that RACM underestimates MACR+MVK in the field in low-NO_x environments. Therefore, it is not surprising that the HET case did not fully rectify the underestimation in HOM. In addition, Section 3.3.2 also noted the impact of OH recycling on MACR+MVK formation. In particular, OH recycling leads to a shift in dominant loss pathway in the primary MACR+MVK ingredient, ISOP, that results in reduced MACR+MVK yields. Switching to HET also does not improve the MACR+MVK diel cycle, specifically the amplitude in the lower canopy. As also discussed in Section 3.3.2, RACM-MIM improves the diel cycle, however results in large concentration overestimates. This suggests that RACM is missing a daytime source of MACR+MVK in low-NO_x environments that RACM-MIM has not fully captured.

Vertical heterogeneity also enhances the simulated exchange of BVOC out of the

canopy (Figure 3.10). CACHE simulates a positive flux of isoprene during the day (Figure 3.10a), indicating flow out of the canopy, whereas the negative formaldehyde and MACR+MVK fluxes signify fluxes into the canopy (Figures 3.10b-c). Due to enhanced isoprene emissions observed in the HET case, nearly 30% more isoprene escapes the canopy in this case than in the HOM scenario. The added isoprene enhances HCHO fluxes by 17% (Figure 3.10c), while the MACR+MVK flux exhibits no daytime enhancement (Figure 3.10b). While the simulated isoprene fluxes (1–1.5 mg C m-2 h-1, Figure 3.10a) are approximately half those observed at UMBS from 2000 to 2002 (2.8–3.2 mg C m-2 h-1, *Pressley et al.*, 2005), we note that 2009 was much cooler and cloudier than average, which may account for the reduced fluxes.

3.4.3 Implications for a post-succession forest

As concluded in the previous section, the specification of vegetation species in the lower and upper canopy vegetation foliage has a strong influence on in-canopy concentrations of isoprene and its oxidation products. Such a distinction is of particular importance for the aspen species at UMBS given that they contribute between half and up to 90% of the local isoprene (*Westberg et al.*, 2001; *Ortega et al.*, 2007) and dominate the upper canopy where sunlight is more plentiful. This suggests that their removal due to ecological succession will have a profound effect on the BVOC chemistry at UMBS (*Pratt et al.*, 2012). While observations at the post-mortality FASET site have not yet occurred, we can examine the atmospheric impacts of the loss of this species as simulated by CACHE, and the sensitivity of these projections to canopy heterogeneity and emissions profiles.

Figure 3.11 shows impact of aspen removal from the upper canopy on BVOC and its oxidation products. We approximate growth of the lower canopy vegetation by maintaining the same total canopy LAI in all simulations (with and without aspen) such that the LAI from the removed foliage is evenly distributed amongst the re-

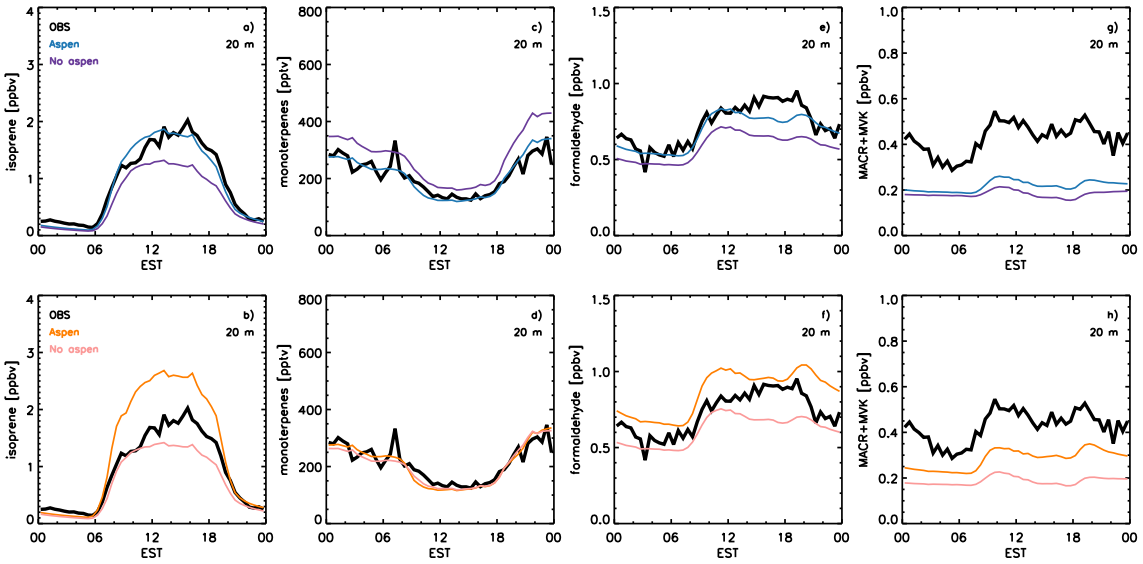

Figure 3.11: HOM- (top) and HET-simulated (bottom) diel cycles of (a, b) ISO, (c, d) MT, (e, f) HCHO, and (g, h) MACR+MVK at 20.4 m with aspen included (blue and orange, representing the HOM and HET simulations from Figure 3.7a, respectively) and excluded (purple and pink for HOM- and HET-based canopies), representing post-successional conditions. Campaign-average observations from CABINEX 2009 are shown as a baseline for present-day conditions.

maining species. CABINEX 2009 observations are shown to provide a baseline for comparison with the model and future studies. According to the model, aspen removal will reduce upper-canopy isoprene concentrations by 50% in the HOM case, resulting in a 24% and 40% decrease in formaldehyde and MACR+MVK, respectively. On the other hand, the HET case shows a 78% reduction in isoprene after aspen is removed, leading to 37% less formaldehyde and 67% less MACR+MVK. HET exhibits greater isoprene decreases than HOM because of the location of aspen foliage relative to light availability. In the HOM case, the aspen is evenly distributed throughout the canopy, whereas in the HET case, aspen is constrained to the upper canopy where light availability is the greatest and thus has the highest emission potential. Overall, HET predicts 62% greater reductions in isoprene with aspen removal than HOM, suggesting a need to adequately represent heterogeneous canopies in future impact studies of forest succession on biogenic chemistry.

3.5 Conclusions

We applied a 1-D canopy-chemistry model to a successional, mixed hardwood forest in northern Michigan to assess the influence of heterogeneities in vertical canopy structure and vegetation composition on canopy-scale atmospheric chemistry. To accomplish this, we conducted two simulations with variable treatment of biogenic VOC emissions: one simulating a homogeneous canopy represented by vertically uniform emission potentials and another simulating a heterogeneous canopy in which emissions potentials vary according to the relative positions of foliage for the dominant tree species. The upper canopy is composed of high-isoprene emitting aspen and oak, atop an understory of young monoterpene emitters, including pine, maple, and beech. In addition to comparing the concentrations and fluxes of BVOC between the two simulations and with observations from the CABINEX 2009 field campaign, we examine the influence of heterogeneity on BVOC projections following ecological

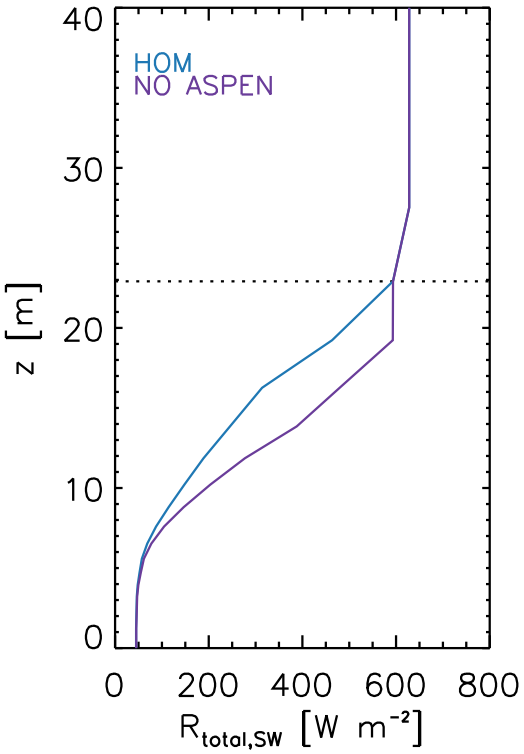

Figure 3.12: Midday (12 PM EST) total solar radiation simulated by the HOM case with (blue) and without aspen (purple). The vertical profiles are the same for the HET case with and without aspen.

succession by comparing the two simulations with and without aspen removed.

Our results show that isoprene and its secondary oxidation products (formaldehyde, methacrolein, and methyl vinyl ketone) are highly sensitive to the placement of emission sources in the canopy. Accounting for heterogeneity in canopy foliage enhances isoprene concentrations by nearly one-third, improving model-measurement agreement. Increased isoprene raises out-of-canopy fluxes and subsequently raises its oxidation products by nearly a quarter. Monoterpenes, on the other hand, show a negligible (less than 5%) sensitivity to canopy heterogeneity. BVOCs generally emit as a function of both light and temperature; however, isoprene emissions generally have a much stronger dependence on light than monoterpenes, and thus, considering the influence of radiation attenuation, the placement of isoprene sources has a much greater impact on BVOC concentrations and fluxes than that of monoterpene sources. In fact, both homogeneous and heterogeneous conditions yield excellent agreement for observed monoterpene concentrations. In light of these results, future modeling studies at UMBS and other FLUXNET sites within mixed forests should consider the role of foliage distribution on BVOC emissions.

The effects of the successional removal of aspen removal are more pronounced in the heterogeneous canopy than the homogeneous canopy by a factor of two. In particular, isoprene is reduced by nearly 80% in the heterogeneous canopy in relation to 50% reductions in the homogeneous case, corresponding to a difference of about 60%. These results highlight the importance of accounting for heterogeneous foliage distribution when analyzing biogenic chemistry in mixed forests.

We note several sources of uncertainty in the present study involving challenges within the community to identify consistent species-level emission factors (*Geron et al.*, 2001; *Niinemets et al.*, 2011). Observationally based emission factors reported in the literature are wide ranging, even for the same species in the same geographical region. In fact, emission factors may vary widely from leaf to leaf on a single

tree, due to variability in leaf age and thickness and any other adaptations to reduce water loss in low-light environments. In this UMBS study, we use the *Ortega et al.* (2007) emission factors for some species, yet note that this study used branch enclosure measurements from a single branch per tree species, which would be unable to capture the intraspecies variability. Finally, leaf and branch enclosures often provoke stress-induced emissions that are not observed under average conditions. Given these limitations, many modeling studies today revert to the genus-level mean values of *Guenther et al.* (1994). Lastly, we note that the emission factor test simulations (i.e., Figure 3.1) were conducted using the homogeneous (HOM) emission factor distribution; running these tests with the HET case may yield different results.

Overall, this work reveals a likely source of uncertainty in the representation of foliar BVOC emissions in 1-D canopy models. Future applications of CACHE and like models should consider the influence of canopy heterogeneity and other complexities pertaining to canopy structure and composition on simulations, particularly in biologically diverse ecosystems. This work also offers a novel and rigorous approach to constructing mixed heterogeneous canopies in 1-D canopy models that improves the simulation of biogenic emissions. Future work should test the robustness of this approach through applications to other sites with vertical biogenic VOC emissions gradients, particularly in other mixed forests. It is also very likely that heterogeneity impacts the accuracy of regional-scale air quality projections. Therefore, if they do not already exist, geographically continuous, gridded datasets of vegetation composition and age ought to be developed to investigate the impact of heterogeneous canopies in regional and global scale modeling of biogenic VOC emissions from plants.

CHAPTER IV

Regional modeling of surface-atmosphere interactions and their impact on Great Lakes hydroclimate

Previously, local-scale forest-atmosphere exchange was examined using a 1-D canopy chemistry model (CACHE) with volatile organic compounds (VOCs) as the tracer. Next, surface-atmosphere exchange at the regional scale and involving both the land and lake interfaces is explored using a 3-D regional climate model (RegCM) and water vapor as the tracer. Like many 1-D canopy models and 3-D regional climate models, CACHE and RegCM differ in terms of modeling framework, particularly at the surface (Section 1.3). While CACHE contains ten model layers within the canopy, RegCM contains only one. Consequently, RegCM is unable to resolve the fine-scale surface layer processes that drive forest-atmosphere exchange and thus either neglects these processes or parameterizes them in a very simple way. The following chapter evaluates and assesses the simplified treatment of land- and lake-atmosphere feedbacks in RegCM by examining how the model simulates the hydroloclimate of the Great Lakes watershed region.

4.1 Abstract

Land and water surfaces play a critical role in hydroclimate by supplying moisture to the atmosphere, yet the ability of climate models to capture their feedbacks with the atmosphere relative to large-scale transport is uncertain. To assess these land-lake-atmosphere feedbacks, we compare the controls on atmospheric moisture simulated by a Regional Climate Model (RegCM) with observations and reanalysis products for the Great Lakes region. Three 23-year simulations with different boundary conditions (one reanalysis product and two general circulation models) are performed to capture the hydroclimatic variability with synoptic conditions. RegCM simulates wetter winters and drier summers than observed by up to 31 and 21%, respectively. Moisture advection exhibits similar biases, suggesting the contribution of external sources, yet land surface fluxes account for nearly one third of summer precipitation. RegCM underestimates reanalysis evapotranspiration by nearly 50%; however, the reanalyses overestimate measurements at three flux towers by up to a factor of two. Neither RegCM nor the reanalyses capture the spatial variability in observed land evapotranspiration, possibly due to underestimations in the observed evapotranspiration response to its atmospheric drivers such as vapor pressure deficit and temperature. Over the lakes, one model member overestimates convective precipitation caused by enhanced evaporation under warm lake surface temperatures, highlighting the need for accurate representation of lake temperature in the surface boundary condition. We conclude that climate models, including those driving reanalyses, underestimate the observed surface-atmosphere feedbacks and their influence on regional hydroclimate.

4.2 Introduction

The Laurentian Great Lakes collectively represent the largest continental water bodies in the world and thus have a profound influence on the local and regional hydroclimate (*Changnon and Jones*, 1972; *Bates et al.*, 1993; *Scott and Huff*, 1996; *Li et al.*, 2010; *Notaro et al.*, 2013a). One classic example of local phenomenon is lake-effect snow, when warm lake surface temperatures beneath the cold winter air enhance evaporation from the lakes and precipitation just beyond the shoreline (*Scott and Huff*, 1996; *Wright et al.*, 2013). On a regional scale, the lakes can perturb atmospheric circulation patterns and other mesoscale features (*Petterssen and Calabrese*, 1959; *Sousounis and Fritsch*, 1994; *Notaro et al.*, 2013a). In addition to water bodies, the land surface exerts a substantial influence on regional climate, especially over dense terrestrial vegetation (*Bonan*, 2008). While the impacts of the land and lakes on regional weather and climate have been well documented, few studies have assessed and distinguished the relative impacts of the Great Lakes and the surrounding land on the regional hydroclimatology. In fact, it has long been assumed that precipitation derives primarily from moisture transported in from long distances relative to local evapotranspiration (*Budyko*, 1974; *Brubaker et al.*, 1993; *Eltahir and Bras*, 1994; *Li et al.*, 2010). While this assumption may be true in most regions dominated by land, the Great Lakes region may stand as an exception due to the vastness of its water bodies. This study aims to quantify the impacts of the land and lake surfaces on Great Lakes hydroclimate and evaluate the ability of a regional climate model to capture these feedbacks and their drivers.

Land and lake surfaces interact with the atmosphere in distinct ways to modify local hydroclimate. Moisture precipitated onto land surfaces can either recycle back to the atmosphere via evaporation (*Brubaker et al.*, 1993) or run off into the lakes. Land and lake evaporation rates typically exhibit offset seasonal cycles due to the thermal inertia of the lakes, with evaporation rates over land and lakes peaking in July and De-

cember, respectively (*Changnon and Jones*, 1972; *Lofgren*, 1997). The influence of the land surface on atmospheric conditions depends on the coupling strength between the land and atmosphere. Land-atmosphere coupling, where small perturbations in the land surface feed back to the atmosphere, have been defined as energy-limited or soil moisture-limited (*Seneviratne et al.*, 2010). Energy-limited regimes are limited by the surface energy balance, temperatures, and incoming radiation versus the amount of water availability. The northern location of the Great Lakes region (above 40° N) suggests that evapotranspiration is typically energy-limited (*Tawfik and Steiner*, 2013), and generally these regions tend to have weak land-atmosphere coupling relative to soil moisture-limited regions.

Several studies have applied regional climate models (RCMs) to the Great Lakes region to assess the complex lake-atmosphere interactions (*Bates et al.*, 1993, 1995; *Goyette et al.*, 2000; *Lofgren*, 2004; *Mao and Cherkauer*, 2009; *Mishra et al.*, 2010; *Cherkauer and Sinha*, 2010; *Zhong et al.*, 2012; *Notaro et al.*, 2013a,b). *Zhong et al.* (2012) use the Penn State-NCAR Mesoscale Model version 5 (MM5), driven by multiple boundary conditions, and find that the model accurately represents moisture fluxes estimated by NARR. *Notaro et al.* (2013b) found the Regional Climate Model (RegCM) reproduces lake-effect snowfall and ice coverage over the Great Lakes in the winter when using an interactive lake module. However, while RCMs generally simulate atmospheric conditions, their ability to simulate land-lake-atmosphere feedbacks remains uncertain (*Jimenez et al.*, 2014).

In this study, we use RegCM coupled with the NCAR Community Land Model (CLM version 3.5, *Oleson et al.*, 2004, 2008) to investigate the land- and lake-atmosphere feedbacks on hydroclimate in the Great Lakes region. We first evaluate the simulated moisture budget components (precipitation, evaporation, and moisture transport) against a suite of observational and reanalysis datasets to provide a baseline understanding of the model performance (Section 4.4). This evaluation also

compares moisture fluxes from the land and lake surfaces and surrounding regions to identify the relative sources and sinks of atmospheric moisture in the region. We then quantify and evaluate land-lake-atmosphere feedbacks by estimating local moisture recycling and by comparing observed and simulated relationships between land and lake moisture fluxes and their drivers (Section 4.5). This chapter expands upon previous work by comparing the land and lakes as atmospheric moisture sources and identifying the sources of error in the simulated moisture budget. We simulate the continental United States to capture the influence of large-scale dynamics and utilize an extensive array of observations to constrain our model evaluation. The overall goal of this chapter is to improve our understanding of the controls on atmospheric moisture in the Great Lakes region, particularly the role of the land and lake surfaces. Our results provide useful insights for improving the representation of hydroclimatic feedbacks in large-scale climate models, which may lead to more reliable projections of the impacts of climate change on the Great Lakes.

4.3 Methods

4.3.1 Model and simulation design

We simulate atmospheric and surface conditions, processes, and interactions using the Abdus Salam International Centre for Theoretical Physics (ICTP) Regional Climate Model version 4.3.4 (RegCM; *Giorgi et al.*, 2012) coupled with the National Center for Atmospheric Research (NCAR) Community Land Model version 3.5 (CLM; *Oleson et al.*, 2004). Precipitation is simulated with both large-scale and convective precipitation parameterizations. Large-scale (i.e., non-convective) precipitation is generated by the Subgrid Explicit Moisture Scheme (SUBEX; *Pal et al.*, 2000), which simulates precipitation instantaneously where and when relative humidity supports cloud formation and cloud water content exceeds an empirically derived temperature-

dependent threshold. Convective precipitation follows the *Grell* (1993) scheme, which treats cumulus convection as an updraft-downdraft circulation occurring within a single cloud plume. Several conditions must be met to generate circulation and cloud development: (1) Total column moisture tendency must be positive; (2) an updraft originating level, LCL, and LFC must exist below the maximum cloud base height ($\sigma = 0.4 \approx 400$ mb); (3) the LCL-LFC stable layer, if it exists, must be less than 150-mb thick; and (4) an equilibrium level must exist at least 150 mb above the LCL. The updraft-downdraft circulation is initialized between the maximum and minimum levels of moist static energy (MSE), with mass fluxes directly proportional to the available buoyant energy generated by the cloud work functions of *Arakawa and Schubert* (1974). The updraft mass flux decreases over a given timescale according to the *Fritsch and Chappell* (1980) closure scheme. The downdraft mass flux is equivalent to the updraft mass flux scaled by the fractions gained via condensation in the updraft and lost via evaporation. An additional convection scheme, the *Emanuel* (1991) scheme, was also tested over the model domain; however, this parameterization placed the summer local precipitation maximum over the Great Lakes instead of the Northern Great Plains as observed, resulting in overly wet conditions in the region of study (results not shown). Therefore, all simulations presented here utilize the Grell scheme.

RegCM has been coupled with two land surface models: the Biosphere-Atmosphere Transfer Scheme (BATS; *Dickinson et al.*, 1986, 1993) and CLM3.5 (*Tawfik and Steiner*, 2011). Compared to BATS, CLM has a more complex treatment of the land surface, including more soil layers and textures, and a wider array of vegetation classes that dynamically change based on their phenological cycles. This added complexity makes CLM an ideal choice for our investigation of land-atmosphere interactions. In addition, our study offers a comparison with the application of RegCM coupled with BATS to the Great Lakes region conducted by *Notaro et al.* (2013a,b). The CLM land

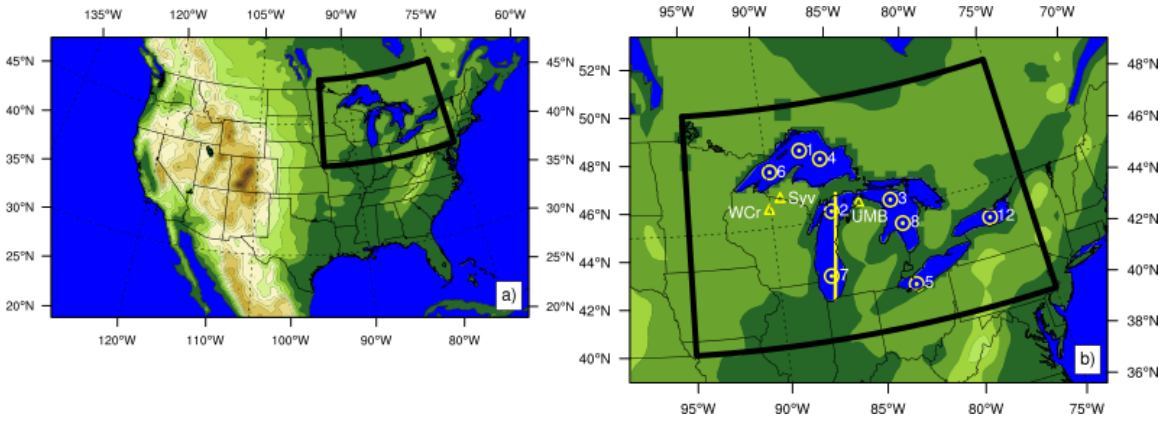

Figure 4.1: (a) Simulation domain and (b) GLW analysis domain (40–50° N, 95–75° W, black outline) with FLUXNET tower (triangles) and NDBC buoy (dotted circles) locations. UMB, WCr, and Syv denote the University of Michigan Biological Station, Willow Creek, and Sylvania Wilderness Area FLUXNET sites, respectively. The numbered buoy identifiers correspond to the last 1–2 digits of the station ID listed in Table 4.1. The yellow line spanning lengthwise through Lake Michigan denotes the latitudinal band used in the cross-sections in Figure 4.12.

surface model represents vegetation with 4–6 plant functional types (PFT) per model grid cell. Land cover types and PFTs are distinguished by several attributes affecting land-atmosphere interactions, including optical properties (e.g., albedo), aerodynamic roughness, and several factors that influence soil moisture exchange. While CLM contains a lake model that computes prognostic lake temperatures and ice coverage, test simulations with the lake model indicated that lake temperatures had cold bias of up to 10 °C in the winter, resulting in excessive winter ice coverage (results not shown). In order to capture the lake-atmosphere feedbacks, we constrain lake surface temperatures from global sea surface temperature (SST) datasets instead of the online lake model. In the absence of SST data over the lakes, RegCM interpolates the ocean SSTs along the nearest coastline to estimate lake surface temperatures.

We simulate climate and surface interactions in the continental United States (Figure 4.1a) for the 23-year historical period ranging from January 1980 to December 2002. Simulating the full continental U.S. allows the model to capture the influences

of synoptic scale weather patterns and topography, but we constrain our analysis to the sub-region encompassing the Great Lakes watershed (40–50° N, 95–75° W; Figure 4.1b), hereafter referred to as the GLW domain to distinguish from the full simulation domain over the continental U.S. Model simulations are at 25 km horizontal grid spacing to capture the fine-scale interactions between the Great Lakes and the overlying atmosphere.

We conduct three simulations constrained by different lateral boundary conditions and sea surface temperature datasets to assess the impact of input selection on simulation results and identify the effect of synoptic weather patterns on moisture transport (Section 4.4.3). First, we drive RegCM with the ECMWF ERA-Interim reanalysis dataset (hereafter RCM-ERA, *Dee et al.*, 2011) to accurately capture large-scale conditions. In addition to ERA reanalysis, we drive the model with two general circulation models (GCMs): GFDL-ESM2M (RCM-GFDL, *Dunne et al.*, 2012, 2013) and HadGEM2-ES (RCM-HADGEM, *Collins et al.*, 2011; *Martin et al.*, 2011). Climate change studies depend on GCMs to simulate future climate and thus it is necessary to evaluate the representation of land-lake-atmosphere feedbacks in GCM-driven regional models. Of the dozens of models from the Coupled Model Intercomparison Project Phase 5 (CMIP5), only eight are available for input into RegCM. Two of the eight members—GFDL-ESM2M and HadGEM2-ES—best capture the seasonal cycle of precipitation averaged spatially over the GLW domain (results not shown). RCM-ERA derives SSTs from the NCEP 2D-Var and the NOAA Optimum Interpolation Sea Surface Temperature (OISST, version 2) datasets (*Dee et al.*, 2011). Simulated skin temperatures are used for ocean, land, and lake surface temperatures in RCM-GFDL. While simulated SSTs from the parent model are used for the RCM-HADGEM simulation, we note that the dataset excludes lake surface temperatures and thus RegCM interpolates between the ocean coastlines, as previously discussed. In addition to the 23-year analysis period, we initialized the model with a 12- and 20-month spinup,

beginning January 1979 and May 1978 for the RCM-ERA and GCM-driven simulations, respectively, with the length of spinup depending on availability of input data. Dynamic vegetation is not included in our simulations.

4.3.2 Observational datasets

Observational datasets used in this study derive from three sources: (1) gridded observation products, (2) flux towers, and (3) lake buoys. We evaluate RegCM temperature and precipitation output with station data gridded globally at 0.5° resolution by the Climatic Research Unit of the University of East Anglia (CRU, *New et al.*, 2000). CRU compares well in the region with similar observational data products, including gridded precipitation datasets from the National Weather Service Climate Prediction Center retrospective analysis (CPC) and from Willmott, Matsuura, and Collaborators at University of Delaware (UDel) (results not shown).

Data are obtained from the FLUXNET database (*Baldocchi et al.*, 2001) to evaluate soil and air temperature, atmospheric moisture, and evapotranspiration rates. FLUXNET provides observational data from a widespread network of flux towers, which can be used to evaluate and constrain regional land models (*Williams et al.*, 2009). Our analysis domain (GLW) contains 21 FLUXNET locations; however, only three sites (Table 4.1, Figure 4.1b) contain more than one year of post-processed data within the simulation time frame for the variables explored in this study: (1) University of Michigan Biological Station (UMB hereafter in the text, *Schmid et al.*, 2003) in Pellston, MI, (2) Willow Creek (WCr, *Cook et al.*, 2004) in Park Falls, WI, and (3) Sylvania Wilderness Area (Syv, *Desai et al.*, 2005) in Watersmeet, MI. All three sites consist of deciduous broadleaf vegetation with subtle differences in species composition. The mid-successional UMB forest consists of an overstory of aspen and birch overlying a understory of white pine, red oak, and sugar maple (*Pressley et al.*, 2005). In contrast, Willow Creek contains sugar maple, basswood, and green ash

Table 4.1: Location, data availability, and measurement information for the point-based observational datasets used in this study. T_{air} height is the location of the air temperature measurement on the tower or buoy; the depth of the subsurface temperature measurement is given by T_{soil} and T_{lake} for towers and buoys, respectively. Tower and buoy data come from the FLUXNET database and the NOAA National Data Buoy Center (NDBC), respectively. Towers are located at the University of Michigan Biological Station (UMB), Willow Creek (WCr), and Sylvania Wilderness Area (Syv) forest sites. Tower and buoy locations are shown in Figure 4.1b.

	Location	Years available	T_{air} height	$T_{\text{soil}}/T_{\text{lake}}$ depth
Towers				
UMB	45.56 N, 84.71 W	1999 – present	46 m	2 cm
WCr	45.81 N, 90.08 W	1999 – present	30 m	0 cm
Syv	46.24 N, 89.35 W	2001 – 2008	36 m	5 cm
Buoys				
45001 (Superior)	48.06 N, 87.78 W	1980 – present	4.0 m	0.6 m
45002 (Michigan)	45.34 N, 86.41 W	1980 – present	4.0 m	1.0 m
45003 (Huron)	45.35 N, 82.84 W	1980 – present	3.2 m	1.0 m
45004 (Superior)	47.58 N, 86.69 W	1980 – present	4.0 m	1.0 m
45005 (Erie)	41.67 N, 82.40 W	1980 – present	4.0 m	0.6 m
45006 (Superior)	47.34 N, 89.79 W	1981 – present	4.0 m	0.6 m
45007 (Michigan)	42.67 N, 87.03 W	1981 – present	4.0 m	0.6 m
45008 (Huron)	44.28 N, 82.42 W	1981 – present	4.0 m	0.6 m
45012 (Ontario)	43.62 N, 77.41 W	2002 – present	4.0 m	0.6 m

Table 4.2: Percentage of the plant functional types (PFT) prescribed in the RegCM simulations for the three FLUXNET sites: University of Michigan Biological Station (UMB), Willow Creek (WCr), and Sylvania Wilderness Area (Syv). Values are spatial averages over a 3-by-3 grid (excluding lake points) centered on each flux tower (see geographical coordinates in Table 4.1).

	UMB	WCr	Syv
Needleleaf evergreen temperate tree	16	18	15
Needleleaf evergreen boreal tree	0	1	11
Broadleaf deciduous temperate tree	38	35	19
Broadleaf deciduous boreal tree	0	1	15
C3 non-arctic grass	27	14	29
Corn	18	31	12

(*Cook et al.*, 2004), and Sylvania Wilderness Area contains eastern hemlock, sugar maple, and birch (*Desai et al.*, 2005). These species are well represented in the model land cover description, as indicated by the PFTs prescribed in RegCM at the grid points corresponding to the three sites (Table 4.2). We use eddy-covariance-derived latent heat flux measurements to evaluate modeled evapotranspiration. When comparing with gridded model (Section 4.3.1) and reanalysis (Section 4.3.3) datasets, we average the gridded data over a 3-by-3 ($225\,\mathrm{km}^2$) grid centered on the geographical coordinates of each tower (Table 4.1). Due to its nearby proximity to lakes Michigan and Huron, the 3-by-3 grid centered on the UMB site contains lake points that we exclude from our analysis over land due to the contrasting nature of land- and lake-atmosphere feedbacks. The vegetation composition across the land-based grid points in the 3-by-3 grids are mostly consistent according to the PFT description.

We use buoy-based observations (Table 4.1) from the NOAA National Data Buoy Center to evaluate climatological lake and air surface temperatures. Each lake contains one to three buoys (Figure 4.1b) with air and lake surface measurements ranging from 3.2–4 m above the lake surface and 0.6–1 m below the surface, respectively. We compute a climatological average of the nine mid-lake buoys (Figure 4.1) for comparison against lake model grid points. Date ranges for the climatological averages vary due to data availability. Five buoys were first launched in 1980, three in 1981, and one (Lake Ontario) in 2002. Buoy stations are typically removed from the lakes over the winter to prevent ice-related damage and, consequently, winter and early spring data are limited or missing.

4.3.3 Reanalysis products

We supplement the observational datasets with reanalysis products, which assimilate a suite of observational data into global and regional models to create a spatially and temporally continuous atmospheric dataset. While these do not reflect pure

observations, they can be useful to evaluate models for parameters that cannot be measured, are challenging to measure accurately, or where measurements are sparse. Here, we use evaporation (land evapotranspiration and lake) and upper-level atmospheric moisture and winds from the NARR (*Mesinger et al.*, 2006) and ERA (*Dee et al.*, 2011) reanalysis products. In addition, comparing the global ERA reanalysis product with the RCM-ERA simulation allows us to distinguish the influence of the regional model from the lateral boundary conditions.

4.3.4 Precipitation recycling

To quantify the role of the land and lake surfaces in the Great Lakes hydroclimatology, we estimate the fraction of precipitation that derives from evaporation (P_E/P), or the "moisture recycling efficiency," using the following relationship (*Brubaker et al.*, 1993; *Eltahir and Bras*, 1994; *Schär et al.*, 1999; *Zangvil et al.*, 2004):

$$\frac{P_E}{P} = \frac{E}{E + \mathrm{IF}} \tag{4.1}$$

where E is the GLW-average evapotranspiration (Equation 4.2) and IF is the advective moisture inflow into the region through the perimeter of the GLW analysis domain outlined in Figure 4.1b (Equation 4.3). The validity of Equation 4.1 requires that water vapor deriving from local evaporation and horizontal transport be well mixed in the atmosphere, a condition that studies generally consider met as a result of efficient turbulent transport of evaporated moisture (*Budyko*, 1974). E is a function of the specific humidity gradient between the soil and canopy surfaces (q_{sfc}) and the overlying atmosphere (q_a), which is related to the gradient between the vapor

pressure of air (e_a) and the saturation vapor pressure of the surface ($e_s(T_{\text{sfc}})$):

$$\begin{aligned} E &= -\rho \frac{(q_a - q_{\text{sfc}})}{r_{aw}} \\ &= \frac{\rho c_p}{\gamma \lambda} \frac{(e_s(T_{\text{sfc}}) - e_a)}{r_W} \end{aligned} \tag{4.2}$$

where ρ is the density of the atmosphere, r_{aw} is the bulk aerodynamic resistance of the surface caused by vegetation and the frictional effects of the ground, c_p is the specific heat capacity of dry air at constant pressure, γ is the psychrometric constant, λ is the latent heat of vaporization ($2.5 \times 10^6\ \text{J kg}^{-1}$), and r_W is the resistance accounting for surface dryness. Unless specified otherwise, E includes both land and lake evaporation, where land evaporation comprises of soil evaporation, evaporation from interception storage, and transpiration from vegetation foliage. IF is derived using the relationship for moisture flux divergence given by *Zangvil et al.* (2004):

$$\text{IF} = \text{OF} - \frac{1}{g} \int_{p_t}^{p_s} \oint q V_n \, dl \, dp \tag{4.3}$$

where OF is the flow out of the side boundaries, q is the specific humidity at each boundary, V_n is the wind orthogonal to the respective boundary, p_s and p_t are the surface and top-of-atmosphere pressure, respectively, and dl is the length of the boundary.

By the conservation of mass, the moisture change within the GLW analysis domain ($\partial q / \partial t$) is equal to the sum of the sources and sinks through the surface and side boundaries:

$$\frac{\partial q}{\partial t} = E - P + \text{IF} - \text{OF} \tag{4.4}$$

Assuming the moisture tendency ($\partial q / \partial t$) to be negligible for monthly timescales, the moisture deficit ($E - P$) can be used to approximate the net loss through the side boundaries via advection ($\text{OF} - \text{IF}$), which denotes the moisture flux divergence.

4.4 Evaluation of Great Lakes hydroclimate

In this section, we evaluate the hydroclimate of the GLW region with a three-member ensemble of RegCM simulations driven by different lateral boundary conditions. Unless stated otherwise, we present 23-year (1980–2002) seasonal climatologies, averaged spatially over the GLW analysis domain (40–50° N, 95–75° W, Figure 4.1b). We evaluate the hydroclimate in terms of the moisture fluxes described in Section 4.3.4, including precipitation (Section 4.4.1), evaporation (Section 4.4.2), and advective moisture inflow (Section 4.4.3). For our evaluation, we compare these terms for the three RegCM simulations (Section 4.3.1) against ground-based observations (Section 4.3.2) and the NARR and ERA reanalysis products (Section 4.3.3).

4.4.1 Precipitation

Observed precipitation (CRU) in the GLW region exhibits a seasonal cycle with a winter (DJF) minimum climatological rate of 1.4 $\mathrm{mm\,day^{-1}}$ and a summer (JJA) maximum of 3.2 $\mathrm{mm\,day^{-1}}$ (Figure 4.2a). Other gridded products (e.g., CPC, UDel) show similar seasonal patterns and magnitudes as CRU (not shown). Both reanalysis products and all model simulations generally capture the seasonal trend, but show discrepancies with the observed amplitude. The NARR product underestimates precipitation year-round with biases of up to 14 and 24% in summer and winter, respectively. *Li et al.* (2010) found that NARR predicts a band of reduced precipitation along the U.S.-Canada border during the summer caused by discrepancies between U.S.- and Canada-based observational datasets. Using CRU observations, we confirm that the NARR not only under-predicts summer precipitation along the border, but also over the Great Lakes (Figure 4.3d). In winter, a related dry bias occurs between the Canadian shoreline of the Great Lakes and the 49th parallel (Figure 4.3c). Unlike NARR, the global ERA product overestimates precipitation in the winter, spring, and summer by as much as 22% (Figure 4.2a). Winter biases are strongest due to

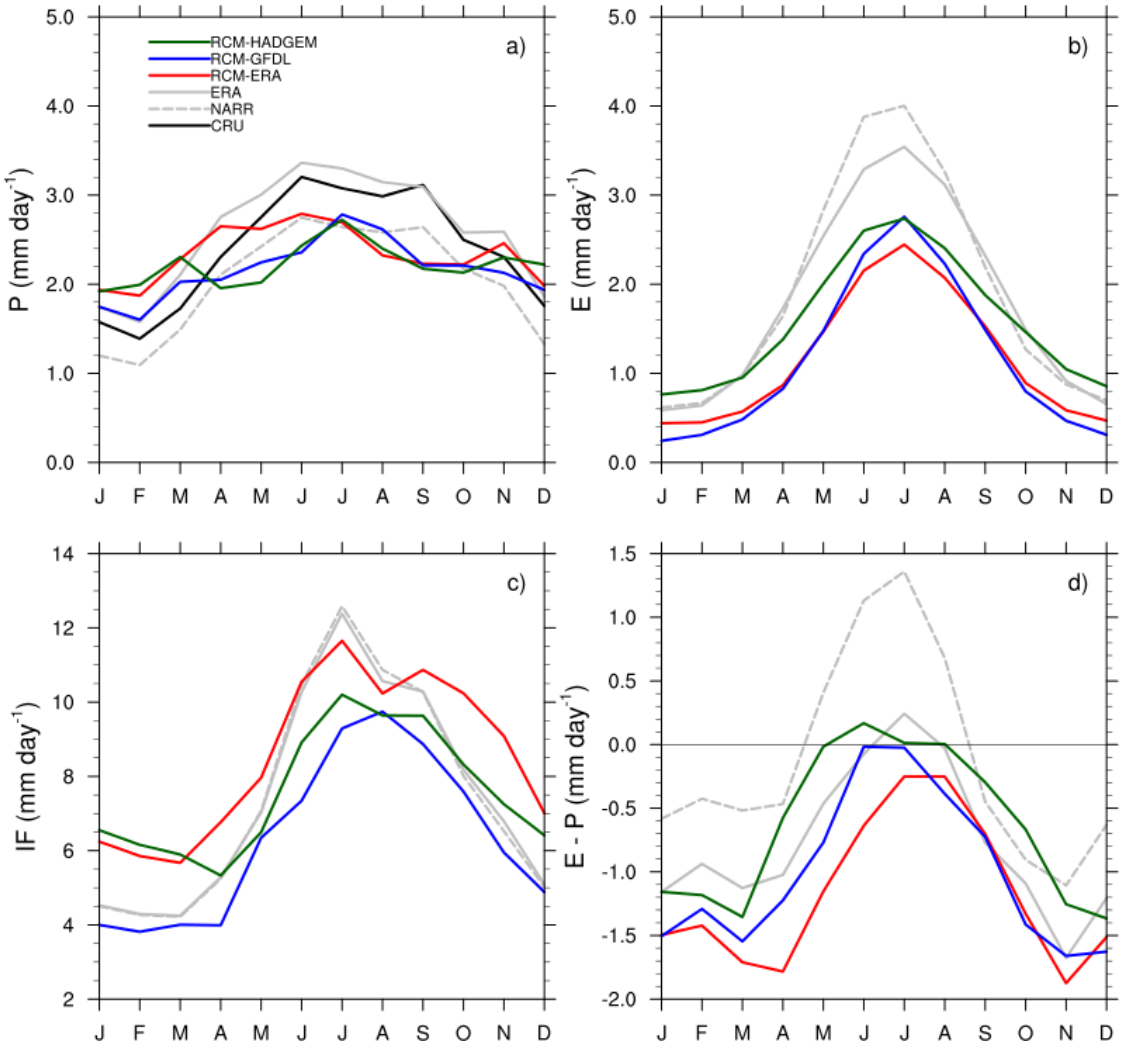

Figure 4.2: Seasonal climatology (1980–2002) of monthly GLW-average (a) precipitation, (b) evaporation, (c) advective inflow (Equation 4.3), and (d) moisture deficit ($E - P$) in mm day^{-1} for CRU observations (black, precipitation only), NARR (dashed grey), ERA (solid grey), RCM-ERA (red), RCM-GFDL (blue), and RCM-HADGEM (green).

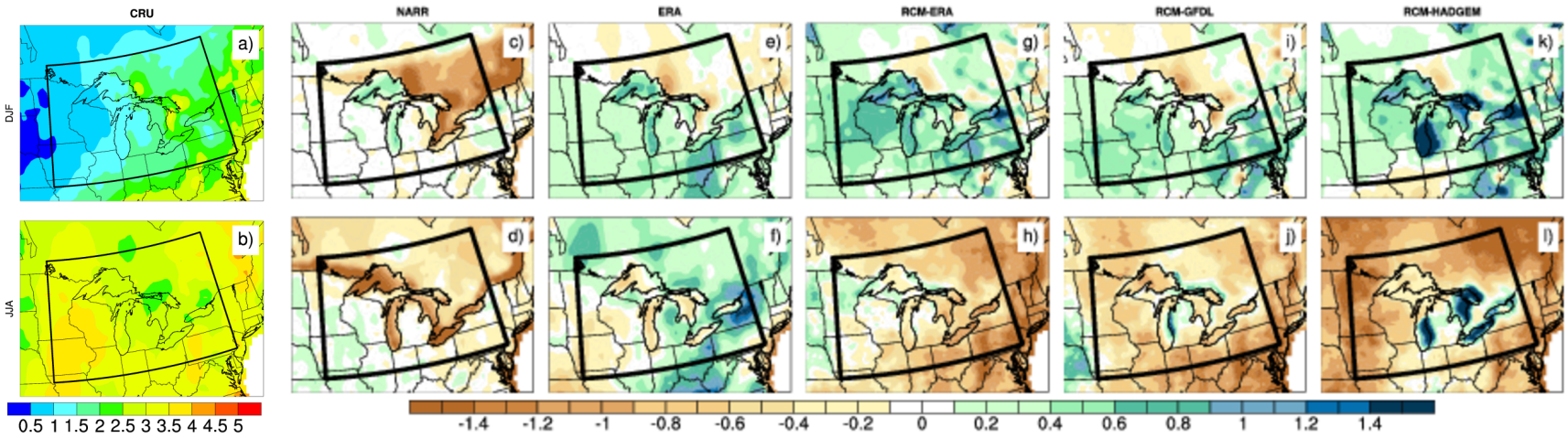

Figure 4.3: Winter (DJF, top row) and summer (JJA, bottom row) spatial distribution of observed precipitation (CRU, a and b; mm day^{-1}) and biases produced by the NARR (c and d), ERA (e and f) and RegCM simulations (g–l). Yellow and brown indicate a dry bias relative to CRU; green and blue indicate wet biases.

the combined contribution of land and the Great Lakes (Figure 4.3e), whereas dry biases over the lakes balance with wet biases over the surrounding land in summer (Figure 4.3f).

Relative to CRU observations and the reanalysis products, all three RegCM simulations have a weaker seasonal precipitation cycle with an average wet bias of up to 31% in winter and a dry bias of up to 21% in summer (Figure 4.2a, see discussion in Section 4.4.3). The biases are consistent over land and lakes in both seasons (Figure 4.3g–l) except for strong wet biases over southern Lake Michigan and Lakes Huron, Erie, and Ontario in the RCM-HADGEM simulation (Figure 4.3k–l) (see discussion in Section 4.5.3). RCM-ERA simulates a weaker seasonal precipitation cycle relative to the parent model (i.e., the global ERA product), indicating that the model physics within RegCM accounts for the precipitation biases rather than the boundary conditions. To identify the processes responsible for the precipitation biases, we evaluate the moisture sources to the region via evaporation and advection in Sections 4.4.2 and 4.4.3 below.

4.4.2 Evaporation

The NARR and ERA reanalysis products estimate GLW-average summer evaporation peaks of 4 and 3.5 mm day^{-1}, respectively, and winter minima of 0.6 mm day^{-1} (Figure 4.2b). RegCM captures the seasonal trend, but peaks 41 and 29% lower than NARR and ERA, respectively, on average across the three simulations in the summer. While evapotranspiration in the GLW is considered energy-limited rather than soil-moisture limited, it is possible that the reanlyses and model differ in whether soil evaporation derives from root-zone soil moisture or other level. Land evapotranspiration reflects the GLW-average (i.e., combined land and lake) seasonal cycle with a maximum in the summer (Figure 4.4a) and a simulation-average discrepancy with the NARR and ERA of 49 and 37%, respectively, indicating that the GLW-average

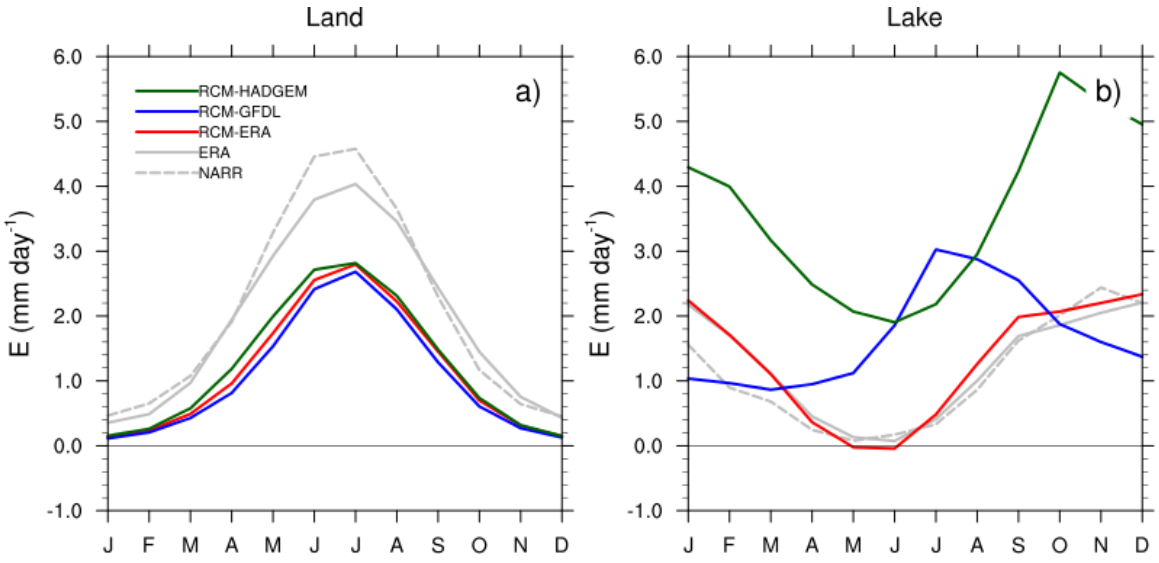

Figure 4.4: Seasonal climatology (1980–2002) of monthly average evaporation (mm day^{-1}), averaged spatially over the (a) land and (b) lake points within the GLW domain, for NARR (dashed grey), ERA (solid grey), RCM-ERA (red), RCM-GFDL (blue), and RCM-HADGEM (green).

model-reanalysis discrepancy in the summer derives from the land.

Latent heat fluxes measured via eddy covariance at three FLUXNET stations (Table 4.1) can evaluate land evapotranspiration produced by the model and reanalysis products (Figure 4.5). RegCM captures the observations at two of the three sites (WCr and Syv; Figures 4.5b–c), whereas both reanalysis products overestimate observations at all three sites by up to a factor of two. Mid-summer evaporation rates observed at the UMB site (Figure 4.5a) peak 24–34% higher than at the two Wisconsin-based sites, yet neither RegCM nor the reanalyses capture the observed enhancement. In fact, NARR shows less evaporation at UMB than the other sites. These results show the model land surface in RegCM more closely simulates observed evapotranspiration than the reanalyses, although both struggle to capture the variability across the three observation sites. As noted by previous studies (e.g., *Trenberth and Guillemot*, 1998), the evapotranspiration estimates in the reanalysis products are poorly constrained and model-dependent. It has long been known that large-scale cli-

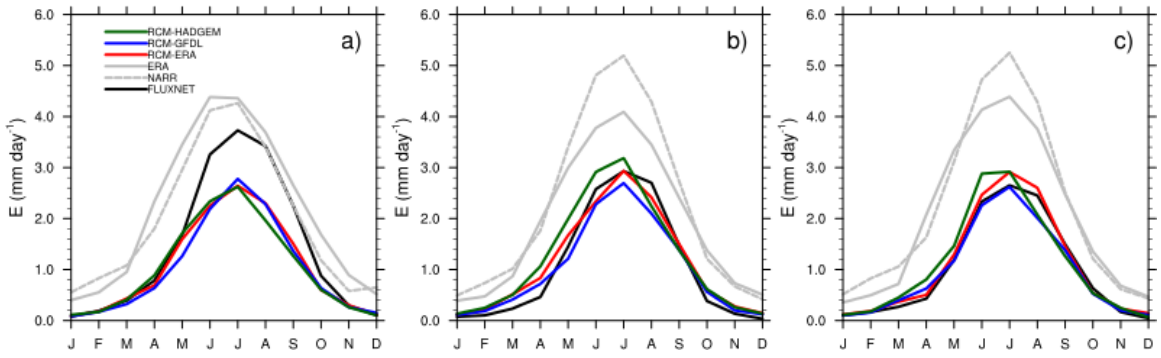

Figure 4.5: Seasonal climatology of evapotranspiration (mm day^{-1}) at the (a) UMB (1999–2002), (b) WCr (1999–2002), and (c) Syv (2001–2002) tower locations. Point-based observations (black) are shown with simulated spatial averages of a 3-by-3 grid (excluding lake points) centered on the tower coordinates (Table 1) for NARR (dashed grey), ERA (solid grey), RCM-ERA (red), RCM-GFDL (blue), and RCM-HADGEM (green).

mate models struggle to represent spatial variations in land-atmosphere interactions caused by sub-grid-scale heterogeneities in surface flux drivers (*Dickinson*, 1995). We note, however, that uncertainties in the eddy covariance measurement of evaporation (as much as 40% at some forest sites according to *Vickers et al.* (2010), though many studies, on average, find daytime and nighttime errors of less than 7 and 12 %, respectively (*Baldocchi*, 2003)) and soil water limitations on evapotranspiration may also lead to observation-model discrepancies.

As shown in previous studies (*Lofgren*, 1997), the lake evaporation seasonal cycle lags behind land evapotranspiration due to the high heat capacity of water. NARR and ERA estimate a 5–6-month delay in the lake evaporation peak, with winter fluxes reaching the same magnitude as land fluxes in the summer (Figure 4.4b). RCM-ERA reproduces both the seasonal cycle and magnitude of lake evaporation estimated by both reanalysis products. In contrast, RCM-HADGEM simulates 2–3 times higher lake evaporation than the reanalyses (Figure 4.4b) (see discussion in Section 4.5.3), and the RCM-GFDL simulation exhibits a seasonal cycle that is significantly phase shifted compared with reanalysis and the other RegCM simulations. The influence of

this strong variability between the model members on the GLW-average evaporation is small and mostly limited to winter, when lake evaporation is the dominant surface moisture source (Figure 4.2b). We note, however, that the lakes make up a relatively small fraction (11.8%) of the total surface area in our analysis domain and thus their influence is stronger on a more localized scale.

4.4.3 Moisture Transport

In addition to evaporative sources, precipitation also derives moisture from outside the GLW region via advection. Here, we focus on the flow into the GLW region through the side boundaries (IF, Equation 4.3) as it is utilized in the precipitation recycling estimate (Equation 4.1). IF has a distinct seasonal cycle that peaks in the late summer (Figure 4.2c). NARR and ERA show nearly identical seasonal trends with a summer peak near 12.5 mm day^{-1}, decreasing to 4 mm day^{-1} in the winter. The agreement between the reanalyses highlights the similarities between the assimilated temperature, wind, and moisture fields in the two datasets. On average, RegCM estimates an 17% lower summer peak inflow rate than the reanalyses with the GCM-driven simulations exhibiting the greatest discrepancies. In the winter, RCM-ERA and RCM-HADGEM advect 23–29% more moisture into the region than the reanalyses, whereas RCM-GFDL predicts 10–11% less. The summer dampening and winter enhancements in the model in part explain the simulated precipitation biases (Figure 4.2a). In addition, the spread across the model members indicates the influence of synoptic conditions, such as the pattern and position of the jet stream and placement of high and low pressure centers, on external moisture sources.

To illustrate the influence of synoptic weather patterns on regional moisture inflow, we identify the dominant moisture sources that control IF in the GLW region and compare the variability in moisture source across the three simulations. Figure 4.6 shows the climatological average winter and summer 850-mb moisture and wind fields

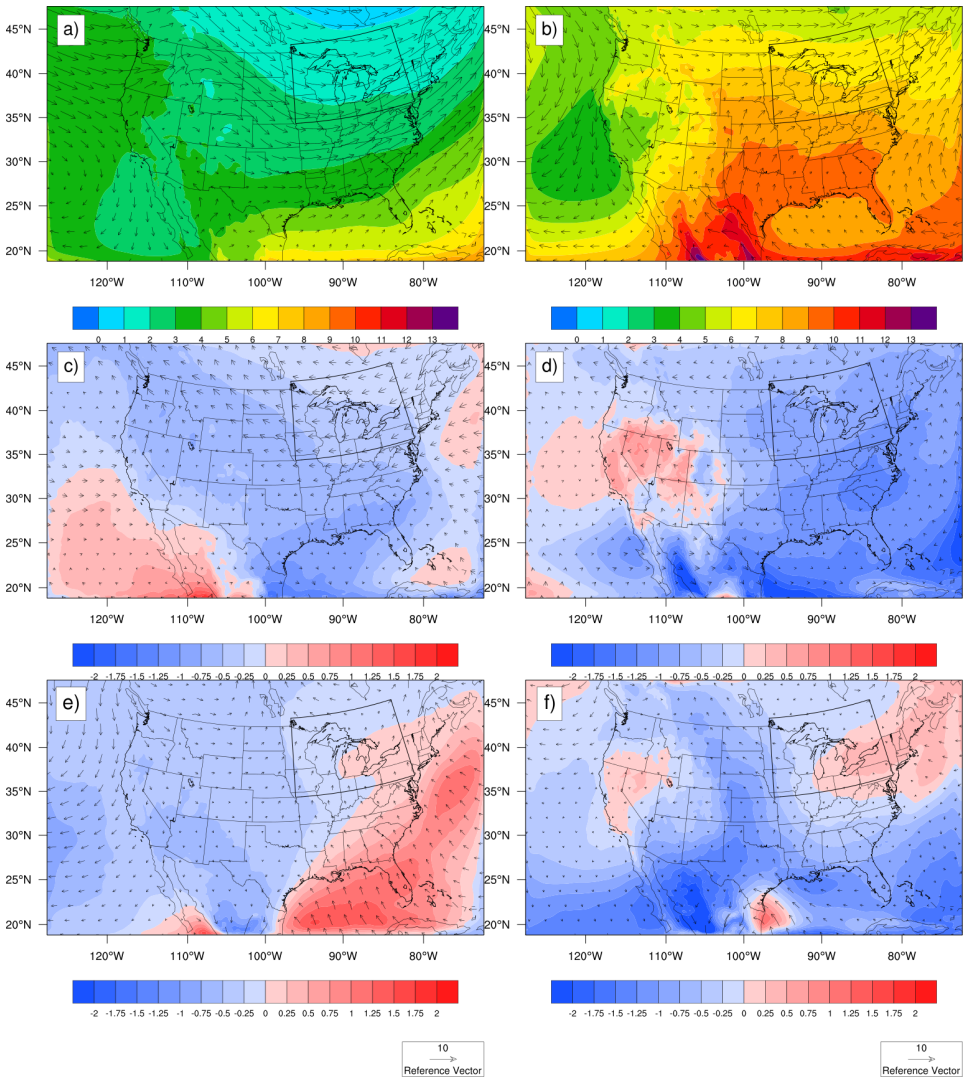

Figure 4.6: 23-year (1980–2002) climatological average winter (DJF, a, c, and e) and summer (JJA, b, d, and f) 850-mb specific humidity ($g\,kg^{-1}$, colored contours) and winds ($m\,s^{-1}$, vectors) for (a, b) RCM-ERA, and the differences between RCM-ERA and (c, d) RCM-GFDL and (e, f) RCM-HADGEM. Red and blue designate more and less moisture, respectively, relative to RCM-ERA. Vectors in panels (c–f) represent the change in wind speed between RCM-ERA and the GCM-driven simulations, so vectors oriented toward the west indicate weaker westerly winds or stronger easterly winds.

over the full model domain (Figure 4.1a) for the three RegCM simulations, where the GCM-driven members are expressed as differences from the reanalysis-driven member (RCM-ERA). RegCM captures the dominant flow patterns and moisture sources typically observed in the two seasons (*Mo et al.*, 2005). In winter (Figure 4.6a), the polar jet stream moves southward, transporting cold, dry air to the upper Midwestern U.S. from the northwest. In summer (Figure 4.6b), moisture increases due to the North American Monsoon (*Higgins et al.*, 1997) and the Great Plains low-level jet (LLJ), which brings moisture from the Gulf of Mexico. These seasonally contrasting flow patterns explain the precipitation (Figure 4.2a) and inflow (Figure 4.2c) that characterize a wet summer and dry winter climate.

In contrast with RCM-ERA, RCM-GFDL simulates approximately 30% less moisture in the northwest in winter (Figure 4.6c) and nearly 25% less in the western Gulf of Mexico in summer (Figure 4.6d) at 850 mb. In addition, zonal winds simulated by RCM-GFDL are half those in RCM-ERA, signifying a weaker polar jet in RCM-GFDL. Both the weaker upstream moisture availability and jet stream strength contributes to reduced IF year-round in RCM-GFDL relative to RCM-ERA (Figure 4.2c), resulting in up to 15% less atmospheric moisture in the GLW domain. Like RCM-GFDL, RCM-HADGEM simulates less moisture in the northwest and southern winter and summer moisture sources than RCM-ERA (Figure 4.6e–f), which promote IF reductions, as seen in summer (Figure 4.2c). In the winter, however, the reduced availability in upstream moisture, which is less substantial than in RCM-GFDL, is balanced by enhancements caused by increased southerly flow (Figure 4.6e), leading to similar inflow rates as RCM-ERA (Figure 4.2c).

Both GCM-driven simulations exhibit lower IF in the summer due to reduced moisture in the LLJ region, where other studies identify challenges simulating convective precipitation. *Dai et al.* (1999) found that, when driven by three convection schemes including the Grell scheme used in the present study, RegCM simulates the

onset of moist convection and thus convective precipitation too readily. Consequently, the atmospheric moisture and convective energy generated over the Rocky Mountains are depleted over the Great Plains resulting in insufficient convective precipitation in the upper Midwest compared to observations. Alternatively, the model may underestimate the influence of the LLJ on convective cloud formation in the Great Plains (*Ghan et al.*, 1996). While the spatial resolution used in our study (25 km) is among the highest applied to regional climate model simulations of the continental United States, the resolution is still too low to fully capture the small-scale physics of convection (*Iorio et al.*, 2004). Overall, our results illustrate that the placement of synoptic features strongly influences the contribution of external moisture sources toward local precipitation, which must be considered when estimating the relative roles of evaporative and advective moisture sources for a given region.

Moisture in the GLW domain exits via advective outflow. By assuming a negligible change in storage of atmospheric moisture within the domain over time at the monthly timescales considered here (i.e., $\frac{\partial q}{\partial t} \approx 0$), we can approximate the net loss (i.e., divergence, OF $-$ IF) of atmospheric moisture through the side boundaries by the net gain of moisture from the surface boundary ($E - P$, see Equation 4.4). The RegCM simulations and ERA reanalyses exhibit a net loss in atmospheric moisture through the surface boundary ($P > E$, Figure 4.2d) in the winter, drawing inflow to the region through the side boundaries and signifying convergence. In the summer, P approximately balances E, indicating negligible moisture loss or gain. In contrast, NARR estimates half to one-third the convergence of the ERA and three RCM simulations in the winter and strong divergence in the summer. The reduced precipitation (Figure 4.2a) combined with enhanced evaporation (Figure 4.2b) in NARR during the summer explains the offset from the other simulations in the moisture deficit. Excluding NARR, precipitation exceeds evaporation on average annually, inducing advection and convergence.

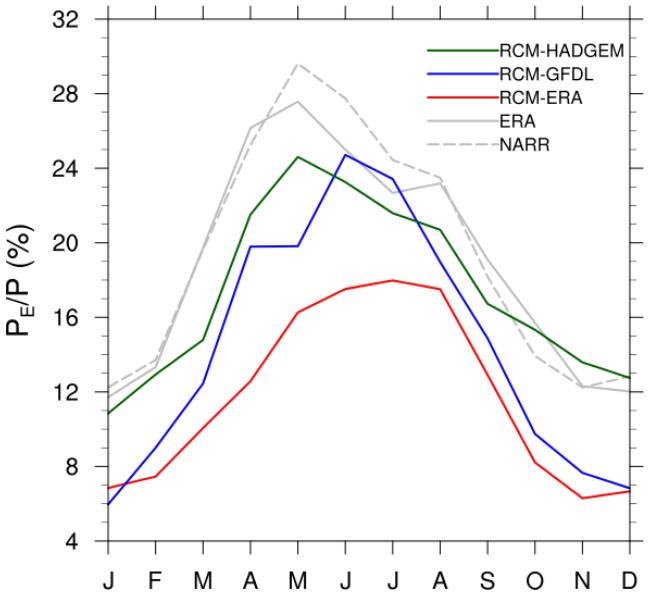

Figure 4.7: As in Figure 4.2, but for the moisture recycling efficiency (Equation 4.1).

4.5 Assessment of surface-atmosphere feedbacks on Great Lakes hydroclimate

In this section, we explore how the land and lake surfaces influence the atmosphere and affect Great Lakes hydroclimate feedbacks. First, we quantify the role of the surface sources as a local moisture source for precipitation relative to external, upstream moisture by estimating the efficiency of local moisture recycling (Equation 4.1). We then assess the ability of the regional climate model to capture the drivers of land-atmosphere and lake-atmosphere feedbacks by comparing simulated conditions and moisture fluxes across the interface against observations from FLUXNET and buoy data (Section 4.3.2).

4.5.1 Moisture recycling

The moisture recycling term (P_E/P, Equation 4.1) is one metric to quantify the feedbacks between the surface and atmosphere. This ratio yields the percentage of precipitation that derives from evaporation. P_E/P peaks in the summer, with the

NARR and ERA reanalysis estimating annual maxima of up to 30 and 28%, respectively, and minima of 12% in winter (Figure 4.7). Because winter lake evaporation exceeds that from land by up to an order of magnitude (Figure 4.4), lake feedbacks such as lake effect snow drive winter recycling. All RegCM members underestimate the recycling ratio estimated by the reanalyses year round, with discrepancies in the summer maximum ranging from 11–21% in the GCM-driven simulations to 49% in RCM-ERA. RCM-ERA estimates the lowest contribution (18% summer maximum) of local evaporation to local precipitation due to the combined effects of lower land evaporation (Figure 4.4a) and higher advective inflow (Figure 4.2c) relative to the other model members. All three simulations, however, exhibit similar evaporation (Figure 4.2b) and thus the recycling differences derive from differences in moisture transport (Figure 4.2c, Section 4.4.3). RCM-ERA recycles 42% less moisture than its global parent product, suggesting that the evaporation and transport discrepancies derive from the effect of dynamical downscaling and varying treatments of atmospheric and land surface processes rather than the boundary conditions. In winter, RCM-HADGEM has evaporation rates (Figure 4.2b) and thus recycling efficiencies that are twice as high as the other two members due to enhanced lake evaporation (Figure 4.4b, see discussion in Section 4.5.3). The concurrent enhancement in lake evaporation and precipitation along the shorelines of the Great Lakes in the RCM-HADGEM case (Figure 4.3k–l) illustrates the surface feedbacks on local precipitation.

We compare our moisture recycling efficiencies with those for nearby regions of the Midwest reported by other studies (*Zangvil et al.*, 2004; *Lamb et al.*, 2012) to identify the unique recycling conditions for the GLW domain. In a region southwest of this study and excluding the Great Lakes (36–43° N, 96–75° W), *Zangvil et al.* (2004) reported summer maximum recycling efficiencies comparable to our RegCM simulations (15–25%) despite reduced evaporation over the cool lakes (Figure 4.4b). In the southern Midwest (approximately 30–39° N, 102–94° W), *Lamb et al.* (2012) reported

lower recycling ratios than both our region and those of Zangvil et al. These comparisons suggest that the dampening effect of the cool lakes on summer evaporation is negligible compared to other factors. For example, *Lamb et al.* (2012) calculated higher advective inflow rates than we estimate, likely due to the enhanced influence of the LLJ in the Great Plains relative to the Great Lakes region. We note, however, that the lakes compose only 11.8% of our analysis domain, and thus our spatially averaged climatologies may diminish the lake feedbacks on moisture recycling. Additionally, these studies exclude the fall and winter seasons when the lakes have the strongest influence in enhancing evaporation (Figure 4.4b).

Despite little evidence of lake feedbacks on summer recycling, our results reveal that the surface contributes up to third of the moisture precipitated locally in the Great Lakes region relative to external sources. While our findings are consistent with studies of other regions, the discrepancies between simulated and reanalysis-estimated evaporation rates identified in Section 4.4.2 suggest that we may underestimate the role of the surface in the Great Lakes region.

4.5.2 Land-atmosphere feedbacks

To understand the control of fluxes from the land surface on the atmosphere, we examine the drivers of surface moisture fluxes based on FLUXNET observations and the RegCM model simulations. As shown by Equation 4.2, evapotranspiration occurs when the moisture content (or vapor pressure) of the surface exceeds that of air. Evapotranspiration is limited by the amount of water vapor the atmosphere can hold; therefore, the vapor pressure deficit of air (VPD $= e_s(T_a) - e_a$; i.e., the distance from saturation) is an effective proxy for evaporative demand. Measurements taken at three FLUXNET sites within the GLW domain show a linear relationship between evaporation and VPD, with evaporation increasing with increasing VPD from winter to summer (Figure 4.8a, c, e). The measurements can be fit with two linear relation-

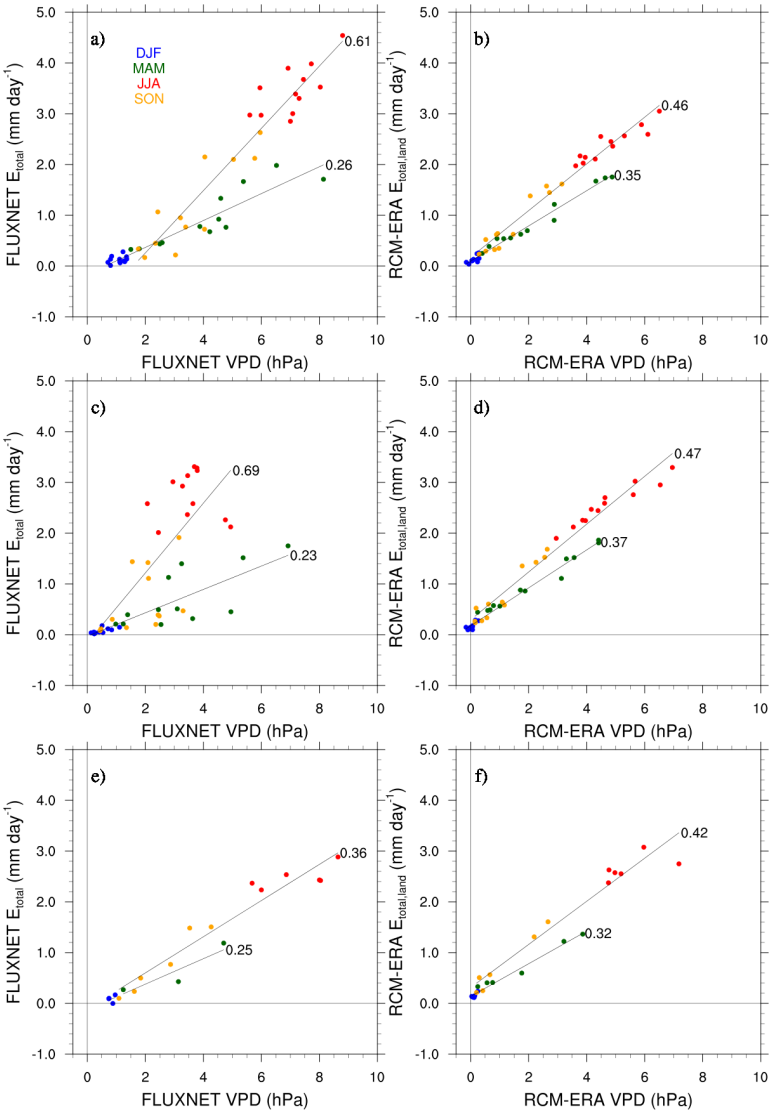

Figure 4.8: Observed (a, c, e) and simulated (b, d, f; RCM-ERA only, 2-m) monthly average evaporation ($\mathrm{mm\,day^{-1}}$) with respect to vapor pressure deficit (VPD, hPa) at the UMB (1999–2002, a and b), WCr (1999–2002, c and d), and Syv (2001–2002, e and f) tower locations. Linear regressions and corresponding slopes for the winter-spring and summer-fall seasonal groups are shown in black.

ships: one for winter and spring and another, with a steeper slope, for summer and fall. This pattern indicates that the evapotranspiration response to VPD is stronger in the summer and fall than in the winter and spring. One likely explanation for this phenomenon is that the cool soils inhibit evaporative fluxes in the winter and spring by lowering the surface saturation vapor pressure, and vice versa in summer and fall when the soil surface is warm. Another possibility is that leaf area in the spring and early summer exceed that in the late summer and fall. All three sites exhibit nearly identical winter-spring slopes ($\sim 0.25\,\mathrm{mm\,day^{-1}\,hPa^{-1}}$), whereas the summer-fall slope varies from 0.61 and $0.69\,\mathrm{mm\,day^{-1}\,hPa^{-1}}$ at UMB and WCr, respectively, to $0.36\,\mathrm{mm\,day^{-1}\,hPa^{-1}}$ at Syv. Like the observations, all model members (Figure 4.8b, d, f; RCM-ERA only shown) exhibit two linear relationships for the winter-spring and summer-fall regimes, where the summer-fall slope exceeds that of the winter-spring relationships; however, the model does not fully capture the magnitude and site-to-site variability in slope. RCM-ERA overestimates the winter-spring slope by 35 and 28% at UMB and Syv, respectively, and by 61% at WCr. In contrast, the model underestimates the summer-fall slope at UMB and WCr by 25 and 32%, respectively, and overestimates the slope at Syv by 17%. While the model captures the site-to-site variability in the winter-spring slope ($0.03\,\mathrm{mm\,day^{-1}\,hPa^{-1}}$ observed versus $0.05\,\mathrm{mm\,day^{-1}\,hPa^{-1}}$ simulated), the model displays insufficient variability in the summer-fall seasons ($0.33\,\mathrm{mm\,day^{-1}\,hPa^{-1}}$ observed, $0.05\,\mathrm{mm\,day^{-1}\,hPa^{-1}}$ simulated) when evapotranspiration is the strongest. This lack of variability across the three sites in the VPD-evaporation relationship may account for lack of variability in the summer evaporation peak (Section 4.4.2, Figure 4.5) and suggests that the model does not fully capture the dependence of evaporation on VPD.

To more fully understand what drives land evapotranspiration, we examine the controls on VPD. VPD depends exponentially on air temperature through the saturation vapor pressure ($e_s(T_a)$) according to the Clausius-Clapeyron relationship. Like

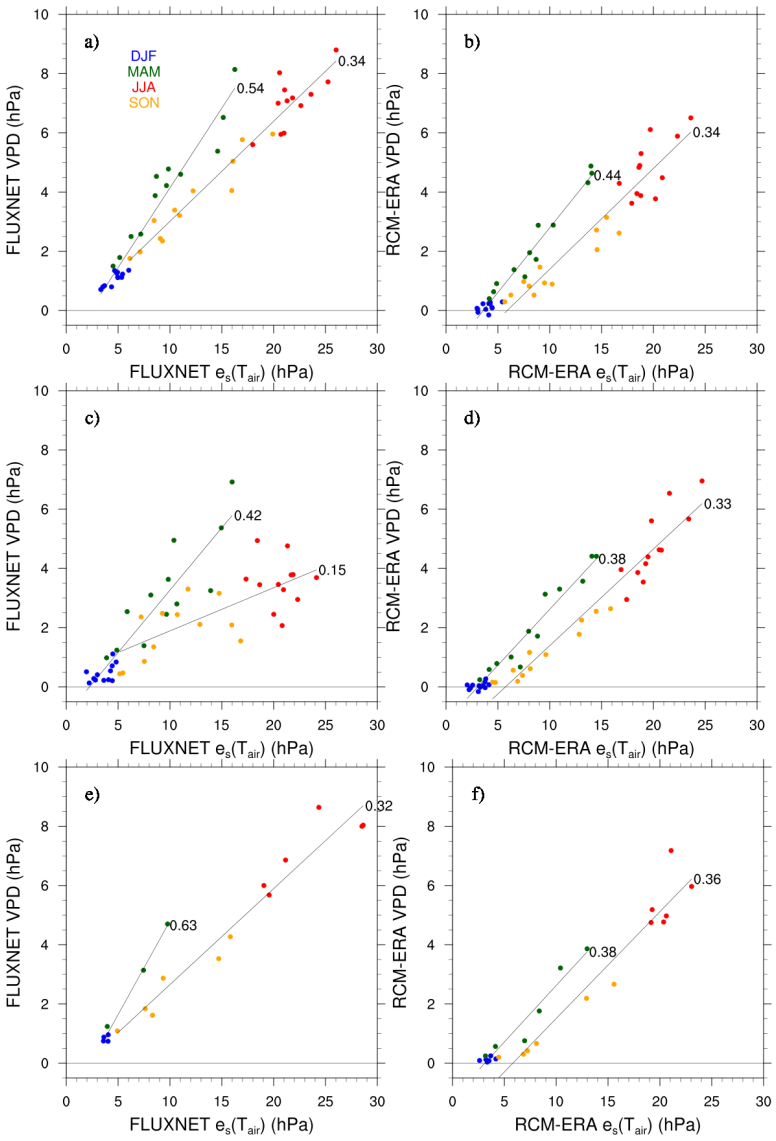

Figure 4.9: As in Figure 4.8, but for VPD (hPa) with respect to saturation vapor pressure of air (hPa).

the relationship between VPD and evaporation, VPD and $e_s(T_a)$ show two distinct linear relationships for the winter-spring and summer-fall seasons according to measurements (Figure 4.9). In this case, however, the winter-spring slope is steeper than the summer-fall slope, indicating a stronger VPD response to temperature in the winter and spring. As discussed above, evaporative fluxes in winter and spring may be lower than summer and fall due to cooler soils, which leads to drier air and thus enhanced VPD, or the reduced contribution from the canopy due to low leaf area densities. As with VPD and evaporation, the model does not capture the variability in slopes of the VPD-$e_s(T_a)$ relationship across the three sites. The model shows a range in slope between the sites of 0.06 and 0.03 $\mathrm{hPa\,hPa^{-1}}$ for the winter-spring and summer-fall regimes, respectively, contrasting with the observed ranges of 0.21 and 0.19 $\mathrm{hPa\,hPa^{-1}}$. While RegCM captures the summer-fall slope at UMB (Figure 4.9a, b) and Syv (Figure 4.9e, f), the model underestimates the winter-spring slope by 19 and 40%, respectively. At WCr (Figure 4.9c, d), the model underestimates the winter-spring slope by only 10%, yet overestimates the summer-fall slope by over a factor of two. These model-measurement comparisons of both the E-VPD and VPD-$e_s(T_a)$ relationships suggest that land-atmosphere feedbacks through evaporation and their dependence on atmospheric conditions such as temperature and VPD are not fully captured by the model, in particular the spatial variability of these feedbacks and their response to these atmospheric drivers.

4.5.3 Lake-atmosphere feedbacks

Land and lake evaporation exhibit different relationships with the surface-air temperature gradient, suggesting variability in the drivers of these two processes (Figure 4.10). Observed evaporation over land exhibits an inverse relationship with the soil-air temperature gradient (Figure 4.10a), likely due to cooler soil temperatures resulting from canopy shading. In contrast, simulated lake evaporation is strongly and

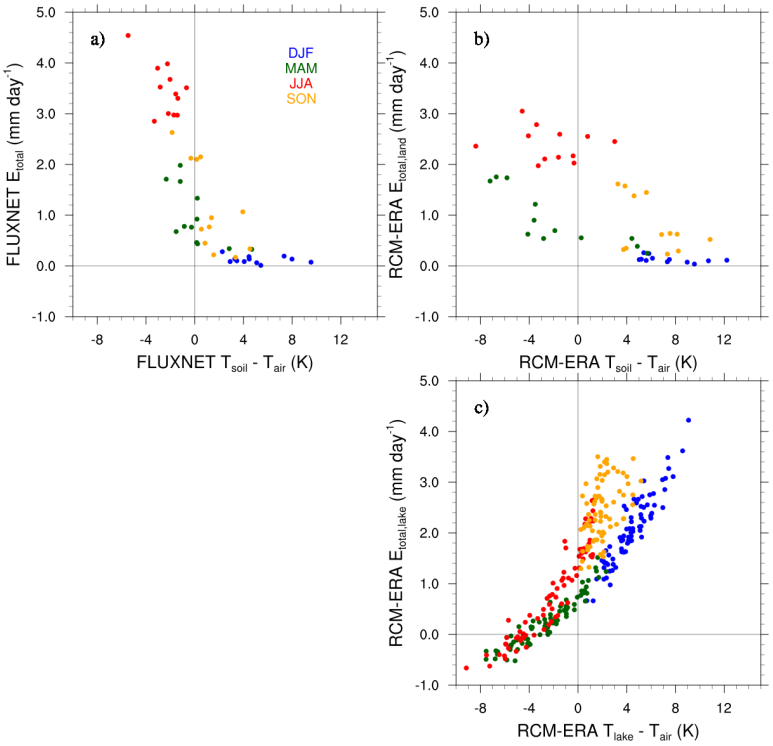

Figure 4.10: (a) Observed and (b) simulated (RCM-ERA) relationship between monthly average evaporation ($\mathrm{mm\,day^{-1}}$) and the soil-air temperature difference (K) at UMB (1999–2002); (c) simulated (RCM-ERA) evaporation ($\mathrm{mm\,day^{-1}}$) with respect to the lake-air temperature difference (K) at the 45007 buoy (1981–2002).

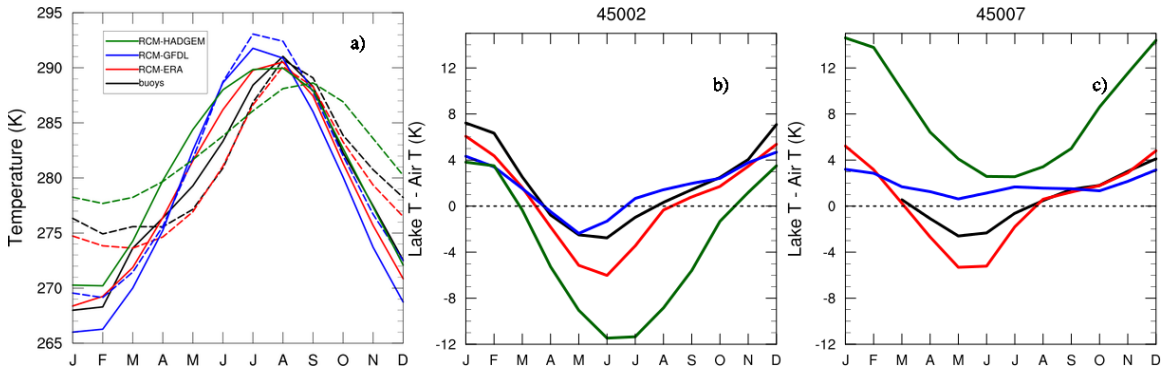

Figure 4.11: (a) Seasonal climatologies (1980–2002) of air- (solid) and lake-surface (dashed) temperatures observed by NDBC buoys (black) and simulated by RCM-ERA (red), RCM-GFDL (blue), and RCM-HADGEM (green). Observed values are averaged across all nine buoys (Table 4.1, Figure 4.1b). Simulated values are averaged spatially over the model lake points. (b) Climatological lake-air temperature gradient for the northern (buoy 45002; 1980–2002) and (c) southern (buoy 45007; 1981–2002) regions of Lake Michigan.

positively correlated with the air-lake temperature gradient (Figure 4.10c). As warm, unsaturated air passes over a cooler and more moist land surface, surface water evaporates, leading to positive evaporation values (Figure 4.10a). Alternatively, snow cover inhibits evaporation in the winter, while insulating the soil such that temperatures become warmer than air, whereas in the summer, canopy shading leads to cooler soils relative to air. Cool air passing over the warm lake surface induces lake evaporation via heating of the lower atmosphere (Figure 4.10c). The model generally captures the relationship over land (Figure 4.10b); however, we are unable to evaluate the lake evaporation dependence on the surface-air temperature gradient due to a lack of lake evaporation observations. These results demonstrate a significant distinction between the forces that drive surface-atmosphere feedbacks over land versus lake surfaces.

Buoy-based observations of near-surface lake and air temperatures allow us to evaluate the lake evaporation drivers, we examine evaluate the simulated lake and near-surface air temperatures (Figure 4.11a). Observed lake surface temperatures (LSTs) generally follow the air surface temperature seasonal cycle with a 1–2-month

lag in warming and cooling during the transition seasons (e.g., MAM and SON). As a result, LSTs are warmer than the overlying air in the fall and winter, which raises the VPD and induces lake evaporation (Figure 4.4b). In contrast, cool LSTs suppress evaporation in the spring and summer by stabilizing the atmosphere. Buoy-observed winter LSTs drop to just above freezing while the air temperature dips further down to 5 K below freezing (Figure 4.11a), resulting in large observed lake-air temperature differences of up to 8 K (Figure 4.11b–c). During the spring and early summer, the air can be up to 2.5 K warmer than the lake due to the existence of lake ice and the higher heat capacity of water. All three RegCM simulations capture the seasonal trend in the lake-air temperature difference with varying amplitude. RCM-ERA generally captures both air and lake surface temperatures (Figure 4.11a), leading to excellent agreement in lake-air temperature differences (Figure 4.11b,c) and evaporation rates (Figure 4.4b). In RCM-GFDL, LSTs follow air temperatures, leading to weak lake-air temperature differences year round and a weak seasonal offset in evaporation. RCM-HADGEM LSTs are 8 K warmer in winter and 3 K cooler in summer, leading to a stronger temperature gradient and evaporation rates that are twice that of NARR, ERA, and the other two simulations. We note that these biases are computed from spatial averages across all five lakes, and that each lake exhibits strong individual variability, particularly in the RCM-HADGEM case (Figure 4.11b–c), as discussed below.

The RCM-HADGEM member demonstrates the power of the lakes in modifying local hydroclimate in all seasons. Due to the lack of LST data in the parent HadGEM2-ES model, LSTs are obtained by interpolating between Pacific and Atlantic Ocean SSTs. This approximation yields unrealistic LSTs in the model, but also provides a unique opportunity to examine the climate impacts of the lakes under a range of LSTs. An artifact of the HadGEM SST interpolation is that the lakes are split into two regimes with contrasting atmospheric feedbacks: in the northern

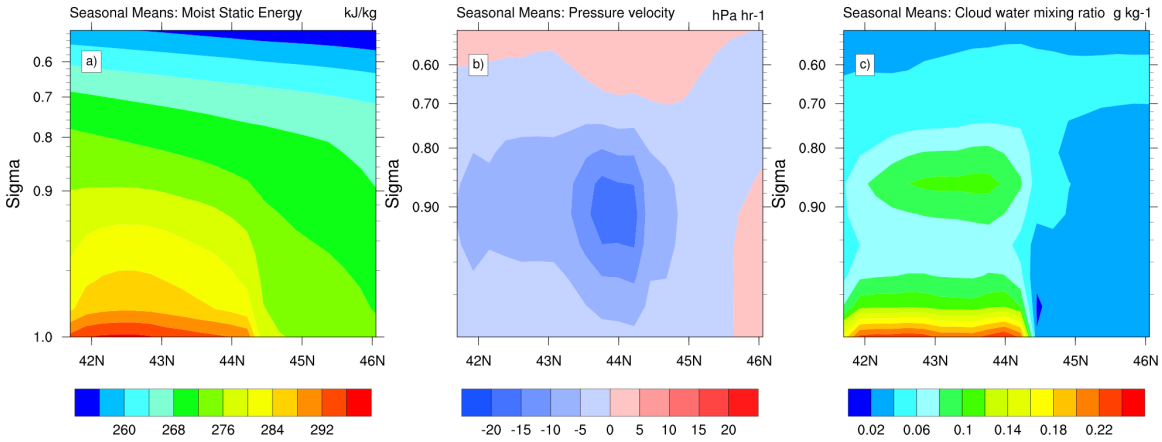

Figure 4.12: RCM-HADGEM-simulated climatological average winter (DJF) (a) moist static energy ($\mathrm{kJ\,kg^{-1}}$), (b) pressure tendency ($\mathrm{hPa\,hr^{-1}}$), and (c) cloud water vapor mixing ratio ($\mathrm{g\,kg^{-1}}$) from the surface ($\sigma = 1$) to approximately 500 mb ($\sigma = 0.5$) along the transect oriented north-south along central Lake Michigan shown in Figure 4.1b. Negative pressure tendency (blue) indicates rising motion.

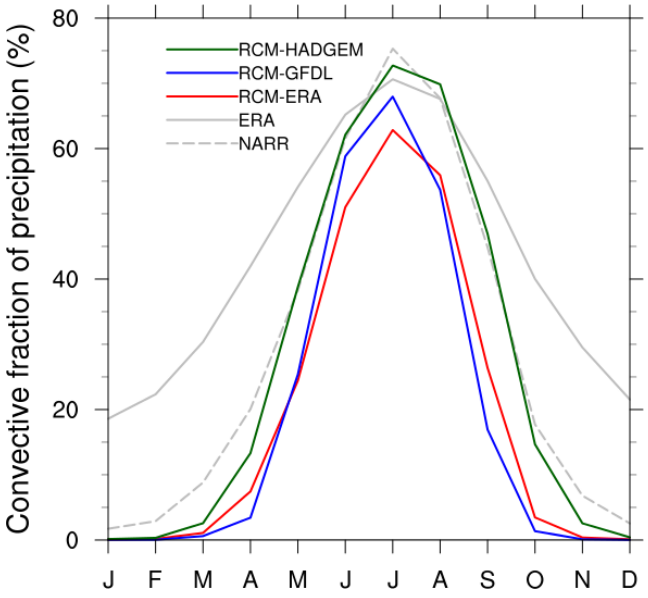

Figure 4.13: As in Figure 4.2, but for fraction of precipitation deriving from convection (%).

lakes (northern Lake Michigan and Superior), LSTs are colder than observed (Figure 4.11b, buoy 45002) and in the southern lakes (southern Michigan, Huron, Erie and Ontario), LSTs are warmer than observed (Figure 4.11c, buoy 45007). In the southern lakes, the warm LSTs heat the overlying atmosphere, resulting in enhanced evaporation (Figures 4.2b, 4.4b) and moisture recycling (Figure 4.7). In addition, convection is enhanced over the warm surface waters. This surface effect propagates into the atmosphere via its effect on vertical profiles of moist static energy (MSE), pressure tendency, and cloud water vapor mixing ratios along the N-S cross-section of Lake Michigan indicated in Figure 4.1b (Figure 4.12). Over the southern lakes (near buoy 45007), the higher atmospheric humidity and temperature over the warm lake waters increases the MSE (Figure 4.12a), which drives convection, as indicated by the enhanced rising motion (Figure 4.12b). The increased surface humidity and rising motion promotes the development of convective clouds above the warm surface waters (Figure 4.12c). Over the cooler northern lake waters (near buoy 45002), these effects on MSE, vertical velocity, and cloud development are not present. The increased convection over the warm southern waters leads to substantial enhancements in convective precipitation over the lakes and their shorelines downstream (Figure 4.3k–l), which increases the overall convective fraction of precipitation in the Great Lakes region by 7–14% (Figure 4.13). Overall, we find that a 4 K increase in LST between the RCM-ERA and RCM-HADGEM simulations in July (Figure 4.11c) increases convective precipitation by 10% (Figure 4.13), or a response rate of $2.5\%\,\mathrm{K}^{-1}$.

In contrast with the warm southern lake surface waters, the cool northern lake surfaces stabilize the atmosphere and inhibit evaporation. Reduced evaporation minimizes cloud cover over the region, increasing the solar radiation received at the surface (not shown), which also modify surface-atmosphere feedbacks, particularly over the land. Both the warm and cool LST regimes highlight the strong atmospheric feedbacks that can occur due to the lake lower boundary condition and their consequences

for variables such as precipitation.

4.6 Conclusions

Using a regional climate model, we simulate present-day hydroclimate to understand the role of surface-atmosphere interactions on regional precipitation in the Great Lakes region. We perform three simulations with different lateral boundary conditions and lake surface temperatures to identify how atmospheric and surface conditions modify these interactions. By evaluating the model with observations and examining the terms of the moisture budget, we can understand the ability of RegCM to capture regional water cycling. We then examine the feedbacks between the surface and atmosphere and their drivers by analyzing moisture recycling and assessing the model's ability to accurately capture these feedbacks.

Relative to a suite of observational datasets and two reanalysis products, RegCM underestimates the amplitude of the regional hydroclimate. For precipitation, the model simulates wetter winters and drier summers than observed. Evaporation is simulated up to 30–40% lower than the reanalysis products, yet is consistent with observations at two FLUXNET stations. However, the reanalyses overestimate evaporation rates at all three sites in the present study by up to twofold, yet neither the model nor the reanalyses capture the spatial variability in evaporation fluxes exhibited by the three sites. We also find that the model underestimates the amplitude of the seasonal cycle of moisture advection into the region as compared to reanalysis, which may contribute to the precipitation biases. Our analysis of the seasonal-average synoptic patterns suggests that regional climate models underestimate upstream moisture sources, particularly in the summer in the central Plains and Gulf of Mexico. As earlier studies suggest (e.g., *Ghan et al.*, 1996; *Dai et al.*, 1999; *Iorio et al.*, 2004), improved parameterizations are needed to better capture the onset and frequency of convection generated in the Rocky Mountains and enhance moisture

transport into the Great Lakes region via the Great Plains low level jet.

While precipitation predominantly originates from moisture sources external to the Great Lakes region, the surface can contribute up to 30% of the moisture during the summer and 12% during the winter. The evaporation bias reduces the modeled recycling efficiency of moisture, which suggests that moisture recycling in the Great Lakes region may be more efficient than that estimated by these regional climate model simulations. These results indicate that local feedbacks on regional hydroclimate are not negligible, as previous studies suggest (e.g., *Budyko*, 1974; *Li et al.*, 2010), and such feedbacks should be considered in future hydroclimate analyses. Comparisons of RegCM driven by ERA reanalysis with the global ERA product indicate that downscaling large-scale boundary conditions and the representation of land surface processes in regional models have a substantial effect on simulated surface-atmosphere feedbacks. Synoptic conditions also modify recycling via their effect on inflow rates.

Land-based evapotranspiration correlates with the vapor pressure deficit, which depends on the temperature and humidity of the lower atmosphere. FLUXNET observations indicate two different linear slopes between the winter-spring and summer-fall VPD-evaporation relationships. In addition, we find that the dependence of evaporation on VPD varies across the three sites. RegCM reproduces the winter-spring slope, but does not capture the variability in the summer-fall slope. Similar to the VPD-evaporation relationship, the model captures the dependence of VPD on temperature via the saturation vapor pressure but does not capture the variability in slopes across the three sites. These results show that RegCM does not fully capture the response of evaporation to its atmospheric drivers, in particular the spatial variability in these responses, which may explain the lack of spatial variability in evaporation in the model. Overall, our comparisons with FLUXNET demonstrate that deficiencies in the simulation of surface-atmosphere fluxes still exist despite vast improvements in

the representation and treatment of land surface properties and processes in complex land surface models such as CLM. To improve parameterizations of the fundamental surface-atmosphere hydrologic feedbacks, future model development would benefit from further examination with FLUXNET observations at other regions in effort to develop an improved global characterization of the controls on evaporative demand (e.g., near-surface air temperature).

The Great Lakes also interact with the atmosphere and affect the local hydroclimate. Warm lake surface temperatures can warm and moisten the lower atmosphere, leading to high moist static energy, decreased stability, strong rising motion and cloud formation, all of which promote enhanced convective precipitation along the downstream shoreline of the lakes. In contrast, cool lake surface temperatures stabilize the atmosphere and inhibit evaporation and subsequent cloud formation, thus allowing greater solar radiation and less precipitation into the surface. Our simulations show that lake temperature can drive precipitation changes of up to 10% in the overall GLW region with larger amounts on a more localized scale (e.g., along the downwind shorelines of the lakes). These results indicate the importance of lake temperature on the regional hydroclimate and the necessity to provide accurate lake temperature data for the surface boundary condition in climate models.

Our study contains a few limitations worth noting. First, many of the moisture budget components lack sufficient observational data for evaluating the model. While our evaluation of precipitation and surface energy fluxes has a network of ground-based observations, we rely on model-based reanalysis products to evaluate the other components of the moisture budget (e.g., evapotranspiration and moisture advection), which includes its own uncertainties. In fact, our evaluation indicates that the reanalyses overestimate evapotranspiration at all three FLUXNET sites in our analysis domain. The lack of evaporation measurements over the Great Lakes themselves provides a poor constraint for the models.

In addition to the reanalyses uncertainties, the RegCM hydroclimate variables depend on a number of physical parameterizations. In the results presented here, we focus on the variability that can be introduced by lateral boundary conditions, but note that details of the parameterizations chosen may affect our results. For precipitation, we use one convection scheme for simplicity but note that other schemes can provide varying estimates of precipitation. Additionally, RegCM does not distinguish between types of hydrometeors and uses a temperature diagnostic to distinguish rain from snow.

In the Great Lakes region, prior studies have shown that synoptic conditions drive the regional hydroclimate. We conclude that, while synoptic processes are important climatic drivers in the region, local feedbacks between the surface and atmosphere play an important role in the local hydroclimate. Synoptic conditions can strongly modify surface-atmosphere interactions, and the land and lake surface can modify synoptic conditions to further impact such interactions. Accurate representation of surface-atmosphere interactions and their response to synoptic conditions require careful selection of surface boundary conditions, such as the land surface model and lake temperature specification. Overall, our research highlights the role of the land and lake surfaces on local and regional climate and suggests further constraints on surface evaporation may improve the representation of these processes in climate models.

4.7 Acknowledgments

Funding for this work was provided by the National Science Foundation under Grant No. 1039043. Funding for UMB tower research was provided by the U.S. Department of Energy, Office of Science. Funding for operation of the WCr and Syv towers was provided by the Department of Energy and the Ameriflux Network Management Project Support for UW ChEAS Cluster. Additional funding supporting

WCr operations came from the Wisconsin Focus on Energy (EERD #10-06) and the USDA North Central Research Station. Additional support for Syv operations came from Department of Energy, Terrestrial Carbon Processes, now within the Terrestrial Ecosystem Science Program. We also thank Ahmed Tawfik and Travis O'Brien for helpful assistance with performing the model simulations, and Frank Marsik for assistance with the calculation of advective moisture fluxes. Observational data are provided by the sources cited in this chapter. NARR data are available at NOAA's Earth System Research Laboratory (http://www.esrl.noaa.gov/psd/data/gridded/data.narr.html). ERA data can be obtained from the ECMWF Data Server (http://apps.ecmwf.int). Users may obtain model output by contacting Alex Bryan (ambrya@umich.edu). Source code for RegCM is available at https://gforge.ictp.it/gf/project/regcm/.

CHAPTER V

Conclusions

5.1 Summary of work

Forests play a critical role in air quality and climate through their emission of trace gases, such as water vapor and BVOC. Their impact on climate and atmospheric chemistry depends on how efficiently these molecules escape the forest canopy into the atmosphere. BVOC oxidize on a similar timescale as they are mixed in the lower atmosphere (*Molemaker and Vilà-Guerau de Arellano*, 1998), and thus their escape depends on the balance between turbulence and chemistry. While water vapor does not have the same sensitivity to chemistry, exchange is tied with evapotranspiration rates that are controlled by atmospheric and vegetative drivers. This dissertation aims to determine the key drivers of the BVOC and water vapor exchange from the surface to the atmosphere and examine how their exchange is treated in multi-scale models. Ultimately, these exchange processes will impact regional atmospheric chemistry and climate.

We use observed quantities to develop relationships of exchange processes, and then utilize an extensive array of observational datasets on a variety of platforms to assess the model treatment of these processes. Such relationships analyzed here include the relative roles of in-canopy turbulence and chemistry (Chapter II), canopy structure and composition (Chapter III) on BVOC fluxes, and the influence of con-

ditions at the surface-atmosphere interface on water vapor (Chapter IV). This work ultimately highlights the role of the surface in air quality and climate, identifies uncertainties pertaining to the surface role that may impact air quality and climate projections (Section 5.2), and provides direction for future model development.

Chapter II applied the Canopy Atmospheric Chemistry Emission Model (CACHE, *Forkel et al.*, 2006) to observations from CABINEX, finding that near-canopy turbulence can be as important as gas-phase chemistry in modulating forest-atmosphere exchange. This was realized by contrasting two turbulence schemes with two chemistry schemes. Overall magnitudes and the diel patterns of BVOC concentrations were improved when modeled turbulence was driven partially by observations near the canopy. Changing the chemical mechanism to one that included more detailed isoprene degradation (*Geiger et al.*, 2003; *Bryan et al.*, 2012) yielded small changes in concentrations and fluxes out of the forest of primary BVOC (isoprene and monoterpenes), but caused large discrepancies in the secondary oxidation product, methacrolein and methyl vinyl ketone.

Expanding upon the previous chapter, Chapter III applies CACHE with the revised turbulence scheme implemented in Chapter II to the full CABINEX 2009 field campaign but incorporates a vertically heterogeneous canopy with respect to BVOC emissions corresponding to measured species-specific crown heights. The new canopy structure places the highest isoprene emitting foliage in the upper canopy where light is more available, resulting in higher isoprene emissions. Motivated by the FASET experiment, we examined how heterogeneity might affect future BVOC emission projections in a post-successional UMBS forest by removing the aspen from both the homogeneous and heterogeneous canopies and find that the heterogeneous canopy exhibits larger decreases in isoprene emissions than the homogeneous case.

To explore surface-atmosphere exchange in 3-D regional-scale models, land and lake evaporation and their drivers are explored using RegCM and a suite of observa-

tional datasets in Chapter IV. This work determines that the surface can contribute up to one-quarter of the local precipitation and thus adequate simulation of evaporative fluxes are necessary for accurate climate prediction. Compared to observations at three FLUXNET tower sites, which show strong variability between the UMBS site and two sites west of Lake Michigan, RegCM simulates equal magnitudes of evaporation at all sites. Likewise, RegCM does not capture the observed variability in evaporative demand, as evidenced by an invariable response of evaporation to vapor pressure deficit at all three sites. Over the lakes, one model member exhibited extreme lake surface temperatures that had a strong feedback with simulated evaporation and convective precipitation.

This dissertation includes original methodologies, incorporating both new measurements and new modeling techniques. Chapter II introduces both a new model constraint (in-canopy turbulence using observed friction velocity and vertical velocity standard deviation) and couples an updated mechanism (RACM-MIM) to the CACHE model. With the new turbulence scheme applied, Chapter III further modifies CACHE to account for vertical heterogeneity in mixed forests by devising a novel approach to scale BVOC emission factors using new and original field-observed crown height measurements. In addition, CACHE was further updated to include BVOC emissions parameterized by MEGAN and with the addition of OH recycling in RACM as suggested by recent studies. Finally, Chapter IV uniquely utilizes a wide variety of observational platforms to evaluate a regional climate model and the role of evaporation from forest canopies.

5.2 Broad implications

Vegetation sustains human life through its contributions to atmospheric oxygen, the water cycle, and removal of greenhouse gases. Policies to restrict or minimize deforestation in order to preserve these benefits are critical to the continued existence

of a sustainable world. However, the net benefit of forested ecosystems should be balanced with an understanding of the contribution of reactive carbon from vegetation and its influence on air quality. Mitigating these effects requires restricting the emission of anthropogenic precursors, especially in regions undergoing land-cover transformation and urbanization. Additionally, land-cover-change projects to address carbon sequestration and biofuel production should consider the BVOC emissions of these vegetation species to preclude the large addition of reactive carbon to the atmosphere. To adequately establish controls on emissions, understanding the natural processes that drive biogenic precursors and their role in air quality is critical. Any and all sustainability efforts aimed at the reduction of tropospheric ozone production should consider this research and attempt to include an understanding of this science in a holistic and sustainable manner.

5.3 Recommendations for future work

5.3.1 Forest canopy exchange and biogenic VOC and atmospheric chemistry

Forest vegetation provides a key contribution to the reactive carbon in the atmosphere, and understanding the intersection of biogenic and anthropogenic emission on atmospheric chemistry is still poorly constrained. Current chemical mechanisms were developed to investigate ozone pollution in urban areas, where concentrations can reach unsustainable levels due to anthropogenic emissions from industrial activity (*Sillman*, 1999; *Carslaw and Carslaw*, 2001). However, model applications to remote vegetated environments reveal gaps in our understanding of the role of VOCs in the formation of ozone and particulate matter (*Lelieveld et al.*, 2008; *Ganzeveld et al.*, 2008). These findings suggest that more VOC oxidation and thus more ozone formation may occur in forest environments than is presently simulated, which leads to

inaccurate projections of future air quality and climate that may misinform pollution mitigation legislation. Improving our understanding of the role of biogenic VOCs in ozone and particulate matter formation requires an improved understanding of the physical and chemical processes occurring within and above forest canopies that influence VOC concentrations and exchange across the forest-atmosphere boundary.

Above the canopy, robust observations of turbulence quantities are often insufficient due to measurement limitations, posing a challenge for model evaluation and validation in multiple locations. Observational data within the canopy are also limited, and more observations are required at multiple sites to capture the complexities of in-canopy turbulence. In particular, studies incorporating multiple sonic anemometers collocated with sensors measuring temperature and BVOC concentrations, distributed evenly and throughout the full vertical extent of the canopy, are needed to better characterize atmosphere turbulence. Lidar techniques may also provide a more complete picture of canopy turbulence. These data are necessary for characterizing the efficiency of forest-atmosphere BVOC exchange over a wide array of forest types, data that are especially important given the similar timescales of BVOC oxidation and turbulent transport.

Foliar emissions of BVOCs, particularly of isoprene, have been studied extensively over the past few decades, yet large uncertainties in observed emission rates have yet to be explained (*Smiatek and Steinbrecher*, 2006). While day-to-day BVOC emissions have a distinct light and temperature dependence, emissions rates vary in complex ways that are not well characterized (e.g., tree age, temperature history, and soil moisture). Since emissions are known to vary on a site-by-site basis, future research should entail additional inventory development of unexplored biomes, followed by a multi-site synthesis of BVOC emissions from a diverse set of forest ecosystem types. More measurements using a standardized method of observation are required to better quantify species-level emission factors (*Niinemets et al.*, 2011). In particular,

measurements at the top of the canopy using a non-intrusive and non-stress-inducing methodology are needed to estimate the emission potentials under full sunlight exposure. Given the large uncertainties in BVOC emission potentials, future work might consider applying a distribution of potentials as opposed to single values. Providing a rare opportunity to observe the impacts of forest succession on BVOC emissions and a point of model evaluation in Chapter III, the removed aspen at UMBS as part of the FASET campaign begs another field campaign to measure BVOC concentrations for comparison against the CABINEX 2009 measurements.

5.3.2 Vegetation in regional climate models and canopy-atmosphere exchange

Chapter IV highlights two needs for future research to improve surface-atmosphere exchange of water vapor in regional climate models. While much effort has been made to add complexity to the representation of vegetation and soil surfaces, our results point to a need to further develop the fundamental hydrologic functions that drive water vapor fluxes in regional climate models, even those with high resolution. Secondly, an improved representation of lake surface temperatures is needed to realistically capture the feedbacks between the lake and atmosphere before an accurate assessment of how the impact of the Great Lakes on regional hydroclimate will change after climate change.

To date, our understanding of forest-atmosphere exchange derives from studies performed on the local scale (i.e., for a single forest site). Future work is needed to bridge the gap between local-scale forest-atmosphere exchange and regional-scale ozone formation. For example, the K-theory-based surface layer wind and turbulence parameterizations in CLM ought to be explored in light of the results from the 1-D model evaluation in Chapter II. To extend the results from Chapter III to the regional scale, improved land descriptions are needed to account for heterogeneity in

the vegetation descriptions in regional air quality models. In particular, PFT datasets should distinguish vegetation by genus at a minimum, each category assigned representative VOC emission potentials. Each vegetation category should vary spatially in terms of canopy structure (e.g., stand age, height, and foliage density) and VOC emission potentials. Many resources may already be available for developing such datasets using geographic information system (GIS) products. A multi-site synthesis of the forest chemistry observations from various ecosystems would help identify differences in forest-atmosphere exchange across a variety of ecosystem types. Secondly, existing findings, particularly those from a multi-site synthesis, should be incorporated into a global or regional climate-chemistry model, with which the sensitivity of large-scale ozone concentrations to in-canopy processes can be assessed. Future work could include interdisciplinary studies that address the combined effects of the processes discussed in this review to develop a more holistic view of biosphere-atmosphere interactions and their role in forest-atmosphere BVOC exchange.

BIBLIOGRAPHY

BIBLIOGRAPHY

Alaghmand, M., et al. (2011), The morning no$_x$ maximum in the forest atmosphere boundary layer, *Atmos. Chem. Phys. Discuss.*, *11*(10), 29,251–29,282.

Apel, E. C., et al. (2002), Measurement and interpretation of isoprene fluxes and isoprene, methacrolein, and methyl vinyl ketone mixing ratios at the PROPHET site during the 1998 intensive, *J. Geophys. Res.*, *107*, D3, doi:10.1029/2000JD000225.

Arakawa, A., and W. H. Schubert (1974), Interaction of a cumulus cloud ensemble with the large-scale environment, Part I, *J. Atmos. Sci.*, *31*(3), 674–701.

Asner, G. P. (1998), Biophysical and biochemical sources of variability in canopy reflectance, *Remote Sens. Environ.*, *64*(3), 234–253.

Baldocchi, D. (1988), A multi-layer model for estimating sulfur dioxide deposition to a deciduous oak forest canopy, *Atmos. Environ.*, *22*(5), 869–884.

Baldocchi, D., et al. (2001), FLUXNET: A new tool to study the temporal and spatial variability of ecosystem–scale carbon dioxide, water vapor, and energy flux densities, *Bull. Amer. Meteor. Soc.*, *82*(11), 2415–2434.

Baldocchi, D. D. (2003), Assessing the eddy covariance technique for evaluating carbon dioxide exchange rates of ecosystems: past, present and future, *Glob. Change Biol.*, *9*(4), 479–492.

Barkley, M. P., et al. (2011), Can a "state of the art" chemistry transport model simulate amazonian tropospheric chemistry?, *J. Geophys. Res.*, *116*, D16302, doi: 10.1029/2011JD015893.

Bates, G. T., F. Giorgi, and S. W. Hostetler (1993), Toward the simulation of the effects of the Great Lakes on regional climate, *Mon. Wea. Rev.*, *121*(5), 1373–1387.

Bates, G. T., S. W. Hostetler, and F. Giorgi (1995), Two-year simulation of the Great Lakes region with a coupled modeling system, *Mon. Wea. Rev.*, *123*(5), 1505–1522.

Blackadar, A. K. (1979), High-resolution models of the planetary boundary layer, in *Advances in Environmental Science and Engineering*, vol. 1, pp. 50–85, Gordon and Breech Science Publishers, Inc., New York.

Bloomer, B. J., J. W. Stehr, C. A. Piety, R. J. Salawitch, and R. R. Dickerson (2009), Observed relationships of ozone air pollution with temperature and emissions, *Geophys. Res. Lett.*, *36*, L09803, doi:10.1029/2009GL037308.

Bonan, G. B. (1995), Land-atmosphere interactions for climate system models: coupling biophysical, biogeochemical, and ecosystem dynamical processes, *Rem. Sens. Environ.*, *51*(1), 57–73.

Bonan, G. B. (2008), Forests and climate change: Forcings, feedbacks, and the climate benefits of forests, *Science*, *320*(5882), 1444–1449.

Bouvier-Brown, N. C., A. H. Goldstein, J. B. Gilman, W. C. Kuster, and J. A. de Gouw (2009), In-situ ambient quantification of monoterpenes, sesquiterpenes, and related oxygenated compounds during BEARPEX 2007: implications for gas- and particle-phase chemistry, *Atmos. Chem. Phys.*, *9*(15), 5505–5518.

Boy, M., A. Sogachev, J. Lauros, L. Zhou, A. Guenther, and S. Smolander (2011), SOSA – a new model to simulate the concentrations of organic vapours and sulphuric acid inside the ABL – Part 1: Model description and initial evaluation, *Atmos. Chem. Phys.*, *11*(1), 43–51.

Brubaker, K. L., D. Entekhabi, and P. S. Eagleson (1993), Estimation of continental precipitation recycling, *J. Climate*, *6*(6), 1077–1089.

Bryan, A. M., and A. L. Steiner (2013), Canopy controls on the forest-atmosphere exchange of biogenic ozone and aerosol precursors, *Michigan J. Sustain.*, *1*(1), 31–49.

Bryan, A. M., et al. (2012), In-canopy gas-phase chemistry during CABINEX 2009: sensitivity of a 1-D canopy model to vertical mixing and isoprene chemistry, *Atmos. Chem. Phys.*, *12*(18), 8829–8849.

Budyko, M. I. (1974), *Climate and Life*, 508 pp., Academic Press.

Butler, T. M., D. Taraborrelli, C. Brühl, H. Fischer, H. Harder, M. Martinez, J. Williams, M. G. Lawrence, and J. Lelieveld (2008), Improved simulation of isoprene oxidation chemistry with the ECHAM5/MESSy chemistry-climate model: lessons from the GABRIEL airborne field campaign, *Atmos. Chem. Phys.*, *8*(16), 4529–4546.

Carlton, A. G., C. Wiedinmyer, and J. H. Kroll (2009), A review of secondary organic aerosol (SOA) formation from isoprene, *Atmos. Chem. Phys.*, *9*(14), 4987–5005.

Carroll, M. A., S. B. Bertman, and P. B. Shepson (2001), Overview of the Program for Research on Oxidants: PHotochemistry, Emissions, and Transport (PROPHET) summer 1998 measurements intensive, *J. Geophys. Res.*, *106*(D20), 24,275–24,288.

Carslaw, N., and D. Carslaw (2001), The gas-phase chemistry of urban atmospheres, *Surv. Geophys.*, *22*(1), 31–53.

Chameides, W. L., R. W. Lindsay, J. Richardson, and C. S. Kiang (1988), The role of biogenic hydrocarbons in urban photochemical smog: Atlanta as a case study, *Science*, *241*(4872), 1473–1475.

Changnon, S. A., and D. M. A. Jones (1972), Review of the influences of the Great Lakes on weather, *Water Resour. Res.*, *8*(2), 360–371.

Cherkauer, K. A., and T. Sinha (2010), Hydrologic impacts of projected future climate change in the Lake Michigan region, *J. Great Lakes Res.*, *36, Supplement 2*(0), 33–50.

Claeys, M., et al. (2004), Formation of secondary organic aerosols through photooxidation of isoprene, *Science*, *303*(5661), 1173–1176.

Collineau, S., and Y. Brunet (1993a), Detection of turbulent coherent motions in a forest canopy part i: Wavelet analysis, *Bound.-Lay. Meteor.*, *65*(4), 357–379.

Collineau, S., and Y. Brunet (1993b), Detection of turbulent coherent motions in a forest canopy part ii: Time-scales and conditional averages, *Bound.-Lay. Meteor.*, *66*(1), 49–73.

Collins, W. J., et al. (2011), Development and evaluation of an earth-system model – HadGEM2, *Geosci. Model Dev.*, *4*(4), 1051–1075.

Cook, B. D., et al. (2004), Carbon exchange and venting anomalies in an upland deciduous forest in northern Wisconsin, USA, *Agr. Forest Meteorol.*, *126*(3–4), 271–295.

Cooper, O. R., J. L. Moody, T. D. Thornberry, M. S. Town, and M. A. Carroll (2001), PROPHET 1998 meteorological overview and air-mass classification, *J. Geophys. Res.*, *106*(D20), 24,289–24,299.

Dai, A., F. Giorgi, and K. E. Trenberth (1999), Observed and model-simulated diurnal cycles of precipitation over the contiguous United States, *J. Geophys. Res.*, *104*(D6), 6377–6402.

Day, D. A., D. K. Farmer, A. H. Goldstein, P. J. Wooldridge, C. Minejima, and R. C. Cohen (2009), Observations of NO_x, ΣPNs, ΣANs, and HNO_3 at a rural site in the California Sierra Nevada Mountains: summertime diurnal cycles, *Atmos. Chem. Phys.*, *9*(14), 4879–4896.

de Gouw, J., and C. Warneke (2007), Measurements of volatile organic compounds in the Earth's atmosphere using proton-transfer-reaction mass spectrometry, *Mass. Spectrom. Rev.*, *26*, 223–257.

Dee, D. P., et al. (2011), The ERA-Interim reanalysis: configuration and performance of the data assimilation system, *Q.J.R. Meteorol. Soc.*, *137*(656), 553–597.

Desai, A. R., P. V. Bolstad, B. D. Cook, K. J. Davis, and E. V. Carey (2005), Comparing net ecosystem exchange of carbon dioxide between an old-growth and mature forest in the upper Midwest, USA, *Agr. Forest Meteorol.*, *128*(1–2), 33–55.

Di Carlo, P., et al. (2004), Missing OH reactivity in a forest: Evidence for unknown reactive biogenic VOCs, *Science*, *304*(5671), 722–725.

Dickinson, R. E. (1995), Land processes in climate models, *Rem. Sens. Environ.*, *51*(1), 27–38.

Dickinson, R. E., A. Henderson-Sellers, P. J. Kennedy, and M. F. Wilson (1986), Biosphere-atmosphere Transfer Scheme (BATS) for the NCAR Community Climate Model, *Tech. Rep. NCAR/TN-275-+STR*, NCAR, doi:10.5065/D6668B58.

Dickinson, R. E., A. Henderson-Sellers, and P. J. Kennedy (1993), Biosphere-atmosphere Transfer Scheme (BATS) version 1e as coupled to the NCAR Community Climate Model, *Tech. Rep. NCAR/TN-387+STR*, NCAR, doi: 10.5065/D67W6959.

DiGangi, J. P., et al. (2011), First direct measurements of formaldehyde flux via eddy covariance: implications for missing in-canopy formaldehyde sources, *Atmos. Chem. Phys.*, *11*(20), 10,565–10,578.

Dillon, T. J., and J. N. Crowley (2008), Direct detection of OH formation in the reactions of HO_2 with $CH_3C(O)O_2$ and other substituted peroxy radicals, *Atmos. Chem. Phys.*, *8*(16), 4877–4889.

Dunne, J. P., et al. (2012), GFDL's ESM2 global coupled climate–carbon earth system models. Part I: Physical formulation and baseline simulation characteristics, *J. Climate*, *25*(19), 6646–6665.

Dunne, J. P., et al. (2013), GFDL's ESM2 global coupled climatecarbon earth system models. Part II: Carbon system formulation and baseline simulation characteristics, *J. Climate*, *26*(7), 2247–2267.

Dusanter, S., D. Vimal, P. S. Stevens, R. Volkamer, and L. T. Molina (2009), Measurements of OH and HO_2 concentrations during the MCMA-2006 field campaign – Part 1: Deployment of the Indiana University laser-induced fluorescence instrument, *Atmos. Chem. Phys.*, *9*(5), 1665–1685.

Eltahir, E. A. B., and R. L. Bras (1994), Precipitation recycling in the Amazon basin, *Q. J. R. Meteorol. Soc.*, *120*(518), 861–880.

Emanuel, K. A. (1991), A scheme for representing cumulus convection in large-scale models, *J. Atmos. Sci.*, *48*(21), 2313–2329.

Fall, R., and R. K. Monson (1992), Isoprene emission rate and intercellular isoprene concentration as influenced by stomatal distribution and conductance, *Plant Physiol.*, *100*(2), 987–992.

Fall, R., and M. C. Wildermuth (1998), Isoprene synthase: From biochemical mechanism to emission algorithm, *J. Geophys. Res.*, *103*(D19), 25,599–25,609.

Faloona, I., et al. (2001), Nighttime observations of anomalously high levels of hydroxyl radicals above a deciduous forest canopy, *J. Geophys. Res.*, *106*(D20), 24,315–24,333.

Finkelstein, P. L., T. G. Ellestad, J. F. Clarke, T. P. Meyers, D. B. Schwede, E. O. Hebert, and J. A. Neal (2000), Ozone and sulfur dioxide dry deposition to forests: Observations and model evaluation, *J. Geophys. Res.*, *105*(D12), 15,365–15,377.

Finnigan, J. (2000), Turbulence in plant canopies, *Annu. Rev. Fluid Mech.*, *32*(1), 519–571.

Forkel, R., W. Seidl, R. Dlugi, and E. Deigele (1990), A one-dimensional numerical-model to simulate formation and balance of sulfate during radiation fog events, *J. Geophys. Res.*, *95*(D11), 18,501–18,515.

Forkel, R., O. Klemm, M. Graus, B. Rappenglück, W. R. Stockwell, W. Grabmer, A. Held, A. Hansel, and R. Steinbrecher (2006), Trace gas exchange and gas phase chemistry in a Norway spruce forest: A study with a coupled 1-dimensional canopy atmospheric chemistry emission model, *Atmos. Environ.*, *40*, 28–42.

Fritsch, J. M., and C. F. Chappell (1980), Numerical prediction of convectively driven mesoscale pressure systems. Part I: Convective parameterization, *J. Atmos. Sci.*, *37*(8), 1722–1733.

Fuchs, H., B. Bohn, A. Hofzumahaus, F. Holland, K. D. Lu, S. Nehr, F. Rohrer, and A. Wahner (2011), Detection of ho_2 by laser-induced fluorescence: calibration and interferences from ro_2 radicals, *Atmos. Meas. Tech.*, *4*(6), 1209–1225.

Fuentes, J. D., D. Wang, D. R. Bowling, M. Potosnak, R. K. Monson, W. S. Goliff, and W. R. Stockwell (2007), Biogenic hydrocarbon chemistry within and above a mixed deciduous forest, *J. Atmos. Chem.*, *56*(2), 165–185.

Fuentes, J. D., et al. (2000), Biogenic hydrocarbons in the atmospheric boundary layer: A review, *Bull. Amer. Meteor. Soc.*, *81*(7), 1537–1575.

Ganzeveld, L., J. Valverde-Canossa, G. Moortgat, and R. Steinbrecher (2006), Evaluation of peroxide exchanges over a coniferous forest in a single-column chemistry-climate model, *Atmos. Environ.*, *40*(0), 68–80.

Ganzeveld, L., et al. (2008), Surface and boundary layer exchanges of volatile organic compounds, nitrogen oxides and ozone during the GABRIEL campaign, *Atmos. Chem. Phys.*, *8*(20), 6223–6243.

Ganzeveld, L. N., J. Lelieveld, F. J. Dentener, M. C. Krol, A. J. Bouwman, and G.-J. Roelofs (2002), Global soil-biogenic NO_x emissions and the role of canopy processes, *J. Geophys. Res.*, *107*(D16), doi:10.1029/2001JD001289.

Gao, W., M. L. Wesely, and P. V. Doskey (1993), Numerical modeling of the turbulent diffusion and chemistry of NO_x, O_3, isoprene, and other reactive trace gases in and above a forest canopy, *J. Geophys. Res.*, *98*(D10), 18,339–18,353.

Garrity, S. R., K. Meyer, K. D. Maurer, B. Hardiman, and G. Bohrer (2012), Estimating plot-level tree structure in a deciduous forest by combining allometric equations, spatial wavelet analysis and airborne LiDAR, *Remote Sens. Lett.*, *3*(5), 443–451.

Geiger, H., I. Barnes, I. Bejan, T. Benter, and M. Spittler (2003), The tropospheric degradation of isoprene: an updated module for the regional atmospheric chemistry mechanism, *Atmos. Environ.*, *37*(11), 1503–1519.

Geron, C., R. Rasmussen, R. R. Arnts, and A. Guenther (2000), A review and synthesis of monoterpene speciation from forests in the united states, *Atmos. Environ.*, *34*(11), 1761–1781.

Geron, C., P. Harley, and A. Guenther (2001), Isoprene emission capacity for US tree species, *Atmos. Environ.*, *35*(19), 3341–3352.

Ghan, S. J., X. Bian, and L. Corsetti (1996), Simulation of the Great Plains low-level jet and associated clouds by general circulation models, *Mon. Wea. Rev.*, *124*(7), 1388–1408.

Giorgi, F., et al. (2012), RegCM4: model description and preliminary tests over multiple CORDEX domains, *Clim. Res.*, *52*, 7–29.

Goldstein, A. H., and I. E. Galbally (2007), Known and unexplored organic constituents in the Earth's atmosphere, *Environ. Sci. Technol.*, *41*(5), 1514–1521.

Goyette, S., N. A. McFarlane, and G. M. Flato (2000), Application of the Canadian regional climate model to the Laurentian Great Lakes region: Implementation of a lake model, *Atmos. Ocean*, *38*(3), 481–503.

Grell, G. A. (1993), Prognostic evaluation of assumptions used by cumulus parameterizations, *Mon. Wea. Rev.*, *121*(3), 764–787.

Griffith, S. M., et al. (2013), OH and HO_2 radical chemistry during PROPHET 2008 and CABINEX 2009 – Part 1: Measurements and model comparison, *Atmos. Chem. Phys.*, *13*(11), 5403–5423.

Guenther, A. (2013), Biological and chemical diversity of biogenic volatile organic emissions into the atmosphere, *ISRN Atmospheric Sciences*, *2013*, 786290, doi: 10.1155/2013/786290.

Guenther, A., P. Zimmerman, and M. Wildermuth (1994), Natural volatile organic compound emission rate estimates for U.S. woodland landscapes, *Atmos. Environ.*, *28*(6), 1197–1210.

Guenther, A., T. Karl, P. Harley, C. Wiedinmyer, P. I. Palmer, and C. Geron (2006), Estimates of global terrestrial isoprene emissions using MEGAN (Model of Emissions of Gases and Aerosols from Nature), *Atmos. Chem. Phys.*, *6*(11), 3181–3210.

Guenther, A., et al. (1995), A global model of natural volatile organic compound emissions, *J. Geophys. Res.*, *100*(D5), 8873–8892.

Guenther, A. B., R. K. Monson, and R. Fall (1991), Isoprene and monoterpene emission rate variability: Observations with eucalyptus and emission rate algorithm development, *J. Geophys. Res.*, *96*(D6), 10,799–10,808.

Guenther, A. B., P. R. Zimmerman, P. C. Harley, R. K. Monson, and R. Fall (1993), Isoprene and monoterpene emission rate variability: Model evaluations and sensitivity analyses, *J. Geophys. Res.*, *98*(D7), 12,609–12,617.

Hallquist, M., et al. (2009), The formation, properties and impact of secondary organic aerosol: current and emerging issues, *Atmos. Chem. Phys.*, *9*(14), 5155–5236.

Hanson, D. T., and T. D. Sharkey (2001), Rate of acclimation of the capacity for isoprene emission in response to light and temperature, *Plant Cell. Environ.*, *24*(9), 937–946.

Hari, P., M. Raivonen, T. Vesala, J. W. Munger, K. Pilegaard, and M. Kulmala (2003), Atmospheric science: Ultraviolet light and leaf emission of NO_x, *Nature*, *422*, 134.

Hasson, A. S., G. S. Tyndall, and J. J. Orlando (2004), A product yield study of the reaction of HO_2 radicals with ethyl peroxy ($C_2H_5O_2$), acetyl peroxy ($CH_3C(O)O_2$), and acetonyl peroxy ($CH_3C(O)CH_2O_2$) radicals, *J. Phys. Chem. A*, *108*(28), 5979–5989.

Heald, C. L., et al. (2008), Predicted change in global secondary organic aerosol concentrations in response to future climate, emissions, and land use change, *J. Geophys. Res.*, *113*, D05211, doi:10.1029/2007JD009092.

Heus, T., et al. (2010), Formulation of the Dutch Atmospheric Large-Eddy Simulation (DALES) and overview of its applications, *Geosci. Model Dev.*, *3*(2), 415–444.

Hewitt, C. N., et al. (2010), Overview: oxidant and particle photochemical processes above a south-east Asian tropical rainforest (the OP3 project): introduction, rationale, location characteristics and tools, *Atmos. Chem. Phys.*, *10*(1), 169–199.

Higgins, R. W., Y. Yao, and X. L. Wang (1997), Influence of the North American monsoon system on the U.S. summer precipitation regime, *J. Climate*, *10*(10), 2600–2622.

Hofzumahaus, A., et al. (2009), Amplified trace gas removal in the troposphere, *Science*, *324*(5935), 1702–1704.

Hogg, A., J. Uddling, D. Ellsworth, M. A. Carroll, S. Pressley, B. Lamb, and C. Vogel (2007), Stomatal and non-stomatal fluxes of ozone to a northern mixed hardwood forest, *Tellus B*, *59*(3), 514–525.

Horiguchi, M., T. Hayashi, H. Hashiguchi, Y. Ito, and H. Ueda (2010), Observations of coherent turbulence structures in the near-neutral atmospheric boundary layer, *Bound.-Lay. Meteor.*, *136*(1), 25–44.

Huisman, A. J., et al. (2011), Photochemical modeling of glyoxal at a rural site: observations and analysis from BEARPEX 2007, *Atmos. Chem. Phys.*, *11*(17), 8883–8897.

Hurst, J. M., et al. (2001), Investigation of the nighttime decay of isoprene, *J. Geophys. Res.*, *106*(D20), 24,335–24,346.

Iorio, J. P., P. B. Duffy, B. Govindasamy, S. L. Thompson, M. Khairoutdinov, and D. Randall (2004), Effects of model resolution and subgrid-scale physics on the simulation of precipitation in the continental United States, *Clim. Dynam.*, *23*(3–4), 243–258.

Jarvis, P. G. (1976), The interpretation of the variations in leaf water potential and stomatal conductance found in canopies in the field, *Philos. T. Roy. Soc. B*, *273*, 593–610.

Jenkin, M. E., M. D. Hurley, and T. J. Wallington (2007), Investigation of the radical product channel of the $CH_3C(O)O_2 + HO_2$ reaction in the gas phase, *Phys. Chem. Chem. Phys.*, *9*(24), 3149–3162.

Jimenez, P. A., J. V.-G. de Arellano, J. Navarro, and J. F. Gonzalez-Rouco (2014), Understanding landatmosphere interactions across a range of spatial and temporal scales, *Bull. Amer. Meteor. Soc.*, *95*(1), ES14–ES17.

Jobson, B. T., and J. K. McCoskey (2010), Sample drying to improve HCHO measurements by PTR-MS instruments: laboratory and field measurements, *Atmos. Chem. Phys.*, *10*(4), 1821–1835.

Karl, T., M. Potosnak, A. Guenther, D. Clark, J. Walker, J. D. Herrick, and C. Geron (2004), Exchange processes of volatile organic compounds above a tropical rain forest: Implications for modeling tropospheric chemistry above dense vegetation, *J. Geophys. Res.*, *109*, D18306, doi:10.1029/2004JD004738.

Karl, T., A. Guenther, A. Turnipseed, G. Tyndall, P. Artaxo, and S. Martin (2009), Rapid formation of isoprene photo-oxidation products observed in Amazonia, *Atmos. Chem. Phys.*, *9*(20), 7753–7767.

Karl, T., P. Harley, L. Emmons, B. Thornton, A. Guenther, C. Basu, A. Turnipseed, and K. Jardine (2010), Efficient atmospheric cleansing of oxidized organic trace gases by vegetation, *Science*, *330*(6005), 816–819.

Kerminen, V.-M., H. Lihavainen, M. Komppula, Y. Viisanen, and M. Kulmala (2005), Direct observational evidence linking atmospheric aerosol formation and cloud droplet activation, *Geophys. Res. Lett.*, *32*, L14803, doi:10.1029/2005GL023130.

Kesselmeier, J., and M. Staudt (1999), Biogenic volatile organic compounds (VOC): An overview on emission, physiology and ecology, *J. Atmos. Chem.*, *33*, 23, doi: 10.1023/A:1006127516791.

Kim, S., A. Guenther, T. Karl, and J. Greenberg (2011), Contributions of primary and secondary biogenic VOC tototal OH reactivity during the CABINEX (Community Atmosphere-Biosphere INteractions Experiments)-09 field campaign, *Atmos. Chem. Phys.*, *11*(16), 8613–8623.

Kim, S.-W., M. C. Barth, and M. Trainer (2012), Influence of fair-weather cumulus clouds on isoprene chemistry, *J. Geophys. Res.*, *117*, D10302, doi: 10.1029/2011JD017099.

Knohl, A., and D. D. Baldocchi (2008), Effects of diffuse radiation on canopy gas exchange processes in a forest ecosystem, *J. Geophys. Res.*, *113*, G02023, doi: 10.1029/2007JG000663.

Kovacs, T. A., and W. H. Brune (2001), Total OH loss rate measurement, *J. Atmos. Chem.*, *39*(2), 105–122, doi:10.1023/A:1010614113786.

Krol, M. C., M. J. Molemaker, and J. Vilà-Guerau de Arellano (2000), Effects of turbulence and heterogeneous emissions on photochemically active species in the convective boundary layer, *J. Geophys. Res.*, *105*(D5), 6871–6884.

Kroll, J. H., and J. H. Seinfeld (2008), Chemistry of secondary organic aerosol: Formation and evolution of low-volatility organics in the atmosphere, *Atmos. Environ.*, *42*(16), 3593–3624.

LADCO (2010), Regional network assessment: States of Illinois, Indiana, Michigan, Minnesota, Ohio, and Wisconsin, *Tech. rep.*, Lake Michigan Air Directors Consortium (LADCO), Des Plaines, IL, draft report, May 27.

Lamb, P. J., D. H. Portis, and A. Zangvil (2012), Investigation of large-scale atmospheric moisture budget and land surface interactions over U.S. southern Great Plains including for CLASIC (June 2007), *J. Hydrometeor.*, *13*(6), 1719–1738.

Lelieveld, J., et al. (2008), Atmospheric oxidation capacity sustained by a tropical forest, *Nature*, *452*(7188), 737–740.

Lerdau, M., A. Guenther, and R. Monson (1997), Plant production and emission of volatile organic compounds, *BioScience*, *47*(6), 373–383.

Li, X., S. Zhong, X. Bian, W. E. Heilman, Y. Luo, and W. Dong (2010), Hydroclimate and variability in the Great Lakes region as derived from the North American Regional Reanalysis, *J. Geophys. Res.*, *115*, D12104, doi:10.1029/2009JD012756.

Lofgren, B. M. (1997), Simulated effects of idealized Laurentian Great Lakes on regional and large-scale climate, *J. Climate*, *10*(11), 2847–2858.

Lofgren, B. M. (2004), A model for simulation of the climate and hydrology of the Great Lakes basin, *J. Geophys. Res.*, *109*, D18108, doi:10.1029/2004JD004602.

Logan, J. A. (1985), Tropospheric ozone: Seasonal behavior, trends, and anthropogenic influence, *J. Geophys. Res.*, *90*(D6), 10,463–10,482.

Loreto, F., and V. Velikova (2001), Isoprene produced by leaves protects the photosynthetic apparatus against ozone damage, quenches ozone products, and reduces lipid peroxidation of cellular membranes, *Plant Physiol.*, *127*(4), 1781–1787.

Loreto, F., P. Ciccioli, A. Cecinato, E. Brancaleoni, M. Frattoni, C. Fabozzi, and D. Tricoli (1996), Evidence of the photosynthetic origin of monoterpenes emitted by *Quercus ilex* L. leaves by ^{13}C labeling, *Plant Physiol.*, *110*(4), 1317–1322.

Makar, P. A., J. D. Fuentes, D. Wang, R. M. Staebler, and H. A. Wiebe (1999), Chemical processing of biogenic hydrocarbons within and above a temperate deciduous forest, *J. Geophys. Res.*, *104*(D3), 3581–3603.

Mao, D., and K. A. Cherkauer (2009), Impacts of land-use change on hydrologic responses in the Great Lakes region, *J. Hydrol.*, *374*(1–2), 71–82.

Martin, G. M., et al. (2011), The HadGEM2 family of Met Office Unified Model climate configurations, *Geosci. Model Dev.*, *4*(3), 723–757.

Martin, R. S., H. Westberg, E. Allwine, L. Ashman, J. C. Farmer, and B. Lamb (1991), Measurement of isoprene and its atmospheric oxidation products in a central Pennsylvania deciduous forest, *J. Atmos. Chem.*, *13*(1), 1–32.

Martin, S. T., et al. (2010), An overview of the Amazonian aerosol characterization experiment 2008 (AMAZE-08), *Atmos. Chem. Phys.*, *10*(23), 11,415–11,438.

Mesinger, F., et al. (2006), North American Regional Reanalysis, *Bull. Amer. Meteor. Soc.*, *87*(3), 343–360.

Meyers, T. P. (1987), The sensitivity of modeled SO_2 fluxes and profiles to stomatal and boundary layer resistances, *Water Air Soil Poll.*, *35*(3), 261–278.

Meyers, T. P., and D. D. Baldocchi (1988), A comparison of models for deriving dry deposition fluxes of O_3 and SO_2 to a forest canopy, *Tellus B*, *40B*(4), 270–284.

Mishra, V., K. A. Cherkauer, and L. C. Bowling (2010), Parameterization of lakes and wetlands for energy and water balance studies in the Great Lakes region, *J. Hydrometeor.*, *11*(5), 1057–1082.

Misztal, P. K., et al. (2011), Direct ecosystem fluxes of volatile organic compounds from oil palms in South-East Asia, *Atmos. Chem. Phys.*, *11*(17), 8995–9017.

Mo, K. C., M. Chelliah, M. L. Carrera, R. W. Higgins, and W. Ebisuzaki (2005), Atmospheric moisture transport over the United States and Mexico as evaluated in the NCEP Regional Reanalysis, *J. Hydrometeor.*, *6*(5), 710–728.

Molemaker, M. J., and J. Vilà-Guerau de Arellano (1998), Control of chemical reactions by convective turbulence in the boundary layer, *J. Atmos. Sci.*, *55*(4), 568–579.

Monson, R. K., C. H. Jaeger, W. W. Adams III, E. M. Driggers, G. M. Silver, and R. Fall (1992), Relationships among isoprene emission rate, photosynthesis, and isoprene synthase activity as influenced by temperature, *Plant Physiol.*, *98*(3), 1175–1180.

Muller, C. H. (1966), The role of chemical inhibition (allelopathy) in vegetational composition, *B. Torrey Bot. Club*, *93*(5), 332–351.

New, M., M. Hulme, and P. Jones (2000), Representing twentieth-century space–time climate variability. Part II: Development of 1901–96 monthly grids of terrestrial surface climate, *J. Climate*, *13*(13), 2217–2238.

Niinemets, U., R. K. Monson, A. Arneth, P. Ciccioli, J. Kesselmeier, U. Kuhn, S. M. Noe, J. Peñuelas, and M. Staudt (2010), The leaf-level emission factor of volatile isoprenoids: caveats, model algorithms, response shapes and scaling, *Biogeosciences*, *7*(6), 1809–1832.

Niinemets, U., et al. (2011), Estimations of isoprenoid emission capacity from enclosure studies: measurements, data processing, quality and standardized measurement protocols, *Biogeosciences*, *8*(8), 2209–2246.

Notaro, M., K. Holman, A. Zarrin, E. Fluck, S. Vavrus, and V. Bennington (2013a), Influence of the Laurentian Great Lakes on regional climate, *J. Climate*, *26*(3), 789–804.

Notaro, M., A. Zarrin, S. Vavrus, and V. Bennington (2013b), Simulation of heavy lake-effect snowstorms across the Great Lakes basin by RegCM4: Synoptic climatology and variability, *Mon. Wea. Rev.*, *141*(6), 1990–2014.

Oleson, K. W., et al. (2004), Technical description of version 4.0 of the Community Land Model (CLM), *Tech. Rep. NCAR/TN-478+STR*, NCAR, doi: 10.5065/D6FB50WZ.

Oleson, K. W., et al. (2008), Improvements to the Community Land Model and their impact on the hydrological cycle, *J. Geophys. Res.*, *113*, G01021, doi: 10.1029/2007JG000563.

Ortega, J., and D. Helmig (2008), Approaches for quantifying reactive and low-volatility biogenic organic compound emissions by vegetation enclosure techniques – Part a, *Chemosphere*, *72*(3), 343–364.

Ortega, J., D. Helmig, A. Guenther, P. Harley, S. Pressley, and C. Vogel (2007), Flux estimates and OH reaction potential of reactive biogenic volatile organic compounds (BVOCs) from a mixed northern hardwood forest, *Atmos. Environ.*, *41*(26), 5479–5495.

Pal, J. S., E. E. Small, and E. A. B. Eltahir (2000), Simulation of regional-scale water and energy budgets: Representation of subgrid cloud and precipitation processes within RegCM, *J. Geophys. Res.*, *105*(D24), 29,579–29,594.

Pang, X., Y. Mu, Y. Zhang, X. Lee, and J. Yuan (2009), Contribution of isoprene to formaldehyde and ozone formation based on its oxidation products measurement in Beijing, China, *Atmos. Environ.*, *43*(13), 2142–2147.

Patton, E., K. Davis, M. Barth, and P. Sullivan (2001), Decaying scalars emitted by a forest canopy: A numerical study, *Bound.-Lay. Meteor.*, *100*(1), 91–129.

Paulot, F., J. D. Crounse, H. G. Kjaergaard, J. H. Kroll, J. H. Seinfeld, and P. O. Wennberg (2009), Isoprene photooxidation: new insights into the production of acids and organic nitrates, *Atmos. Chem. Phys.*, *9*(4), 1479–1501.

Peeters, J., T. L. Nguyen, and L. Vereecken (2009), HO_x radical regeneration in the oxidation of isoprene, *Phys. Chem. Chem. Phys.*, *11*(28), 5935–5939.

Perterer, J., and C. Körner (1990), The problem of reference parameters in physiological-ecological research with conifer needles, *Forstwiss. Centralbl.*, *109*(4), 220–241.

Pétron, G., P. Harley, J. Greenberg, and A. Guenther (2001), Seasonal temperature variations influence isoprene emission, *Geophys. Res. Lett.*, *28*(9), 1707–1710.

Petterssen, S., and P. A. Calabrese (1959), On some weather influences due to warming of the air by the Great Lakes in winter, *J. Meteor.*, *16*(6), 646–652.

Phillips, M. A., and R. B. Croteau (1999), Resin-based defenses in conifers, *Trends Plant Sci.*, *4*(5), 184–190.

Poisson, N., M. Kanakidou, and P. J. Crutzen (2000), Impact of non-methane hydrocarbons on tropospheric chemistry and the oxidizing power of the global troposphere: 3-dimensional modelling results, *J. Atmos. Chem.*, *36*(2), 157–230.

Pöschl, U., R. von Kuhlmann, N. Poisson, and P. J. Crutzen (2000), Development and intercomparison of condensed isoprene oxidation mechanisms for global atmospheric modeling, *J. Atmos. Chem.*, *37*(1), 29–52.

Pratt, K. A., et al. (2012), A one-dimensional model study of individual reactive biogenic volatile organic compounds and their contributions to organic nitrates above a mixed forest, *Atmos. Chem. Phys.*, *12*(21), 10,125–10,143.

Pressley, S., B. Lamb, H. Westberg, J. Flaherty, J. Chen, and C. Vogel (2005), Long-term isoprene flux measurements above a northern hardwood forest, *J. Geophys. Res.*, *110*, D07301, doi:10.1029/2004JD005523.

Pugh, T. A. M., et al. (2010), Simulating atmospheric composition over a South-East Asian tropical rainforest: performance of a chemistry box model, *Atmos. Chem. Phys.*, *10*(1), 279–298.

Raupach, M. R. (1989), A practical lagrangian method for relating scalar concentrations to source distributions in vegetation canopies, *Q. J. Roy. Meteor. Soc.*, *115*(487), 609–632.

Raupach, M. R., J. J. Finnigan, and Y. Brunei (1996), Coherent eddies and turbulence in vegetation canopies: The mixing-layer analogy, *Bound.-Lay. Meteor.*, *78*(3), 351–382.

Schär, C., D. Lüthi, U. Beyerle, and E. Heise (1999), The soil–precipitation feedback: A process study with a regional climate model, *J. Climate*, *12*(3), 722–741.

Schmid, H. P., H.-B. Su, C. S. Vogel, and P. S. Curtis (2003), Ecosystem-atmosphere exchange of carbon dioxide over a mixed hardwood forest in northern lower Michigan, *J. Geophys. Res.*, *108*, 4417, doi:10.1029/2002JD003011.

Scott, R. W., and F. A. Huff (1996), Impacts of the Great Lakes on regional climate conditions, *J. Great Lakes Res.*, *22*(4), 845–863.

Sellers, P. J., et al. (1996), Comparison of radiative and physiological effects of doubled atmospheric CO_2 on climate, *Science*, *271*(5254), 1402–1406.

Seneviratne, S. I., T. Corti, E. L. Davin, M. Hirschi, E. B. Jaeger, I. Lehner, B. Orlowsky, and A. J. Teuling (2010), Investigating soil moisture–climate interactions in a changing climate: A review, *Earth-Sci. Rev.*, *99*(3–4), 125–161.

Sharkey, T. D., and E. L. Singsaas (1995), Why plants emit isoprene, *Nature*, *374*(6525), 769–769.

Sharkey, T. D., and S. Yeh (2001), Isoprene emission from plants, *Annu. Rev. Plant. Physiol. Plant. Mol. Biol.*, *52*(1), 407–436.

Sharkey, T. D., E. L. Singsaas, P. J. Vanderveer, and C. Geron (1996), Field measurements of isoprene emission from trees in response to temperature and light, *Tree Physiol.*, *16*(7), 649–654.

Sharkey, T. D., A. E. Wiberley, and A. R. Donohue (2008), Isoprene emission from plants: Why and how, *Ann. Bot.-London*, *101*(1), 5–18.

Sillman, S. (1999), The relation between ozone, NO_x and hydrocarbons in urban and polluted rural environments, *Atmos. Environ.*, *33*(12), 1821–1845.

Sillman, S., et al. (2002), Loss of isoprene and sources of nighttime OH radicals at a rural site in the United States: Results from photochemical models, *J. Geophys. Res.*, *107*, 4043, doi:10.1029/2001JD000449.

Simpson, D., A. Guenther, C. N. Hewitt, and R. Steinbrecher (1995), Biogenic emissions in Europe 1. estimates and uncertainties, *J. Geophys. Res.*, *100*(D11), 22,875–22,890.

Smiatek, G., and R. Steinbrecher (2006), Temporal and spatial variation of forest VOC emissions in Germany in the decade 1994–2003, *Atmos. Environ.*, *40, Supplement 1*(0), 166–177.

Sousounis, P. J., and J. M. Fritsch (1994), Lake-aggregate mesoscale disturbances. Part II: A case study of the effects on regional and synoptic-scale weather systems, *Bull. Amer. Meteor. Soc.*, *75*(10), 1793–1811.

Stavrakou, T., J. Peeters, and J.-F. Müller (2010), Improved global modelling of HO_x recycling in isoprene oxidation: evaluation against the GABRIEL and INTEX-A aircraft campaign measurements, *Atmos. Chem. Phys.*, *10*(20), 9863–9878.

Steinbrecher, R., K. Hauff, H. Hakola, and J. Rössler (1999), A revised parametrisation for emission modelling of isoprenoids for boreal plants, in *Biogenic VOC emissions and photochemistry in the boreal regions of Europe – Biphorep*, edited by T. Laurila and V. Lindfors, no. 70 in Air pollution research report, pp. 29–43, Commission of the European Communities, EUR 18910 EN. EC, Brussels.

Steiner, A. H., and A. L. Goldstein (2007), Biogenic VOCs, in *Volatile Organic Compounds in the Atmosphere*, edited by R. Koppmann, pp. 82–128, Blackwell Publishing Ltd, Oxford, UK, doi:10.1002/9780470988657.ch3.

Steiner, A. L., S. Tonse, R. C. Cohen, A. H. Goldstein, and R. A. Harley (2006), Influence of future climate and emissions on regional air quality in California, *J. Geophys. Res.*, *111*, D18303, doi:10.1029/2005JD006935.

Steiner, A. L., S. N. Pressley, A. Botros, E. Jones, S. H. Chung, and S. L. Edburg (2011), Analysis of coherent structures and atmosphere-canopy coupling strength during the CABINEX field campaign, *Atmos. Chem. Phys.*, *11*(23), 11,921–11,936.

Stevens, P., J. Mather, and W. Brune (1994), Measurement of tropospheric OH and HO_2 by laser-induced fluorescence at low pressure, *J. Geophys. Res.*, *99*(D2), 3543–3557.

Stockwell, W. R., F. Kirchner, M. Kuhn, and S. Seefeld (1997), A new mechanism for regional atmospheric chemistry modeling, *J. Geophys. Res.*, *102*(D22), 25,847–25,879.

Stroud, C., et al. (2005), Role of canopy-scale photochemistry in modifying biogenic-atmosphere exchange of reactive terpene species: Results from the CELTIC field study, *J. Geophys. Res.*, *110*, D17303, doi:10.1029/2005JD005775.

Stull, R. B. (1988), *An Introduction to Boundary Layer Meteorology*, Kluwer Academic Publishers, Dordrecht/Boston/London.

Sumner, A. L., et al. (2001), A study of formaldehyde chemistry above a forest canopy, *J. Geophys. Res.*, *106*(D20), 24,387–24,405.

Tan, D., et al. (2001), HO_x budgets in a deciduous forest: Results from the PROPHET summer 1998 campaign, *J. Geophys. Res.*, *106*(D20), 24,407–24,427.

Tawfik, A. B., and A. L. Steiner (2011), The role of soil ice in land-atmosphere coupling over the United States: A soil moisture–precipitation winter feedback mechanism, *J. Geophys. Res.*, *116*, D02113, doi:10.1029/2010JD014333.

Tawfik, A. B., and A. L. Steiner (2013), A proposed physical mechanism for ozone-meteorology correlations using land–atmosphere coupling regimes, *Atmos. Environ.*, *72*(0), 50–59.

Tawfik, A. B., R. Stöckli, A. Goldstein, S. Pressley, and A. L. Steiner (2012), Quantifying the contribution of environmental factors to isoprene flux interannual variability, *Atmos. Environ.*, *54*(0), 216–224.

Tingey, D. T., M. Manning, L. C. Grothaus, and W. F. Burns (1979), The influence of light and temperature on isoprene emission rates from live oak, *Physiol. Plantarum*, *47*(2), 112–118.

Trenberth, K. E., and C. J. Guillemot (1998), Evaluation of the atmospheric moisture and hydrological cycle in the NCEP/NCAR reanalyses, *Clim. Dynam.*, *14*(3), 213–231.

Vickers, D., M. Göckede, and B. E. Law (2010), Uncertainty estimates for 1-h averaged turbulence fluxes of carbon dioxide, latent heat and sensible heat, *Tellus B*, *62*(2), 87–99.

Warneke, C., et al. (2010), Biogenic emission measurement and inventories determination of biogenic emissions in the eastern United States and Texas and comparison with biogenic emission inventories, *J. Geophys. Res.*, *115*, D00F18, doi:10.1029/2009JD012445.

Wesely, M. L. (1989), Parameterization of surface resistances to gaseous dry deposition in regional-scale numerical models, *Atmos. Environ.*, *23*(6), 1293–1304.

Westberg, H., B. Lamb, R. Hafer, A. Hills, P. Shepson, and C. Vogel (2001), Measurement of isoprene fluxes at the PROPHET site, *J. Geophys. Res.*, *106*(D20), 24,347–24,358.

Williams, M., et al. (2009), Improving land surface models with FLUXNET data, *Biogeosciences*, *6*(7), 1341–1359.

Wolfe, G. M., and J. A. Thornton (2011), The Chemistry of Atmosphere-Forest Exchange (CAFE) model – Part 1: Model description and characterization, *Atmos. Chem. Phys.*, *11*(1), 77–101.

Wolfe, G. M., et al. (2011), The Chemistry of Atmosphere-Forest Exchange (CAFE) model – Part 2: Application to BEARPEX-2007 observations, *Atmos. Chem. Phys.*, *11*(3), 1269–1294.

Wright, D. M., D. J. Posselt, and A. L. Steiner (2013), Sensitivity of lake-effect snowfall to lake ice cover and temperature in the Great Lakes region, *Mon. Wea. Rev.*, *141*(2), 670–689.

Zangvil, A., D. H. Portis, and P. J. Lamb (2004), Investigation of the large-scale atmospheric moisture field over the midwestern United States in relation to summer precipitation. Part II: Recycling of local evapotranspiration and association with soil moisture and crop yields, *J. Climate*, *17*(17), 3283–3301.

Zhang, N., X. Zhou, S. Bertman, D. Tang, M. Alaghmand, P. B. Shepson, and M. A. Carroll (2012), Measurements of ambient HONO concentrations and vertical HONO flux above a northern Michigan forest canopy, *Atmos. Chem. Phys.*, *12*(17), 8285–8296.

Zhong, S., X. Li, X. Bian, W. E. Heilman, L. R. Leung, and W. I. Gustafson Jr. (2012), Evaluation of regional climate simulations over the Great Lakes region driven by three global data sets, *J. Great Lakes Res.*, *38*(2), 212–225.